

**SIMULATION OF PARTIALLY SATURATED - SATURATED  
FLOW IN THE CASPAR CREEK E-ROAD  
GROUNDWATER SYSTEM**

by

Jason C. Fisher

A Thesis

Presented to

The Faculty of Humboldt State University

In Partial Fulfillment

of the Requirements for the Degree

Master of Science

In Environmental Systems: Environmental Resources Engineering

May 2000

**SIMULATION OF PARTIALLY SATURATED - SATURATED  
FLOW IN THE CASPAR CREEK E-ROAD  
GROUNDWATER SYSTEM**

by

Jason C. Fisher

Approved by the Master's Thesis Committee:

---

Dr. Margaret Lang, Committee Member Date

---

Dr. Brad Finney, Committee Member Date

---

Jack Lewis Committee Member Date

---

Ronald A. Fritzsche, Date  
Dean of Research and Graduate Studies

## **ABSTRACT**

Over the past decade, the U.S. Forest Service has monitored the subsurface hillslope flow of the E-road swale. The swale is located in the Caspar Creek watershed near Fort Bragg, California. In hydrologic year 1990 a logging road was built across the middle section of the hillslope followed by a total clearcut of the area during the following year. Development of the logging road has resulted in a large build up of subsurface waters upslope of the road. The increase in pore pressures behind the road is of major concern for slope stability and road failure. A conceptual model is developed to describe the movement of water within the E-road groundwater system. The two-dimensional SUTRA model is used to describe both saturated and partially saturated flow within the system. SUTRA utilizes a finite element and integrated finite difference method to approximate the governing equation for flow. The model appears to reproduce the uniquely different frequency responses within the E-Road groundwater system. A comparison of simulated and historical piezometric responses demonstrates the model's inability to reproduce historical drainage rates. The low rates of simulated drainage are attributed to the absence of pipeflow within the model. Finally, road consolidation is associated with increased pore water pressures beneath the road bed.

## **ACKNOWLEDGMENTS**

I would like to express my thanks to the U.S. Forest Service Redwood Sciences Laboratory for their encouragement and support of my work. A special thanks goes to Liz Keppeler and her crew for maintaining the field equipment during the life of this study. I am grateful to Randi Field, co-worker and friend, for the many discussions we shared on the topic of E-Road. I would also like to thank Dr. Robert Willis, a compass in a sea of partial differential equations.

## TABLE OF CONTENTS

<b>LIST OF TABLES</b>	vii
<b>LIST OF FIGURES</b>	viii
<b>NOMENCLATURE</b>	xi
<b>INTRODUCTION</b>	1
<b>HISTORY OF HILLSLOPE GROUNDWATER MODELS</b>	2
<b>DESCRIPTION OF FIELD SITE AND INSTRUMENTATION</b>	7
Piping	14
Pore Pressure	14
Rainfall	19
<b>MODEL FORMULATION AND DEVELOPMENT</b>	22
<b>DESCRIPTION OF MODEL SCENARIOS</b>	28
Scenario 1: Homogeneous and Isotropic	28
Scenario 2: Nonhomogeneous with Active Boundary	28
Scenario 3: Road Consolidation	31
<b>MODEL RESULTS</b>	32
Scenario 1: Sensitivity Analysis and Drainage Simulation	32
Scenario 2: Pre-Road Building	41
Scenario 3: Post-Road Building and Historical Comparisons	43
<b>CONCLUSIONS</b>	52
<b>REFERENCES</b>	53
<b>APPENDIX A: Physical-Mathematical Basis of Numerical Model</b>	57
Fluid Physical Properties	57

<b>Properties of Fluid Within the Solid Matrix</b>	58
<b>Fluid Flow and Flow Properties</b>	62
<b>Partially Saturated Conditions</b>	66
<b>Fluid Mass Balance</b>	78
<b>APPENDIX B: Numerical Methods</b>	82
<b>Basis Functions</b>	82
<b>Coordinate Transformations</b>	88
<b>Gaussian Integration</b>	90
<b>Numerical Approximation of Fluid Mass Balance</b>	94
<b><u>Spatial Integration</u></b>	95
<b><u>Temporal Discretization</u></b>	102
<b>APPENDIX C: Scenario 1 Sensitivity</b>	104
<b>APPENDIX D: Sample SUTRA.d55 Input File</b>	106

## LIST OF TABLES

Table 1: Annual maximum pore pressure within the E-Road piezometers . . . . .	19
Table 2: Scenario 1 parameters for base case simulation . . . . .	33
Table 3: Partially saturated parameters for seven soil types . . . . .	35
Table 4: Scenario 2 parameters . . . . .	42

## LIST OF FIGURES

Figure 1: Location map of E-Road study site . . . . .	7
Figure 2: 3-d rendering of E-Road swale, pre road building . . . . .	9
Figure 3: 3-d rendering of E-Road swale, post road building . . . . .	10
Figure 4: Topography of E-Road swale, post road building . . . . .	11
Figure 5: E-Road during the summer of 1999 . . . . .	12
Figure 6: Distribution of precipitation input within E-Road . . . . .	13
Figure 7: Hypothetical hillslope cross-section . . . . .	13
Figure 8: Method for the collection of piping data . . . . .	15
Figure 9: PVC standpipe container collects pipeflow discharge . . . . .	16
Figure 10: Method for the collection of piezometric data . . . . .	17
Figure 11: Historical water pressures for lower piezometers . . . . .	20
Figure 12: Historical water pressures for upper piezometers . . . . .	21
Figure 13: 3-d rendering of E-Road swale, post road building with profile . . . . .	23
Figure 14: Hypothetical vertical profile of E-Road system . . . . .	24
Figure 15: Discretization and boundary conditions . . . . .	26
Figure 16: Scenario 1, permeability and porosity zones . . . . .	29
Figure 17: Scenario 2, permeability zones with active ground surface boundary	30
Figure 18: Scenario 3, permeability zones with road consolidation . . . . .	31
Figure 19: Scenario 1, pressure RMSE vs. intrinsic permeability . . . . .	34
Figure 20: Scenario 1, pressure RMSE vs. porosity . . . . .	34
Figure 21: Scenario 1, pressure RMSE vs. soil type . . . . .	35
Figure 22: Scenario 1, pressure RMSE vs. temporal step size . . . . .	36

Figure 23: Scenario 1, computational time vs. temporal step size	37
Figure 24: Scenario 1, pressure RMSE vs. number of elements	38
Figure 25: Scenario 1, compuational time vs. total number of elements	38
Figure 26: Scenario 1, parameter sensitivity	39
Figure 27: Scenario 1, pressure contours, drainage of system over 27.8 hr	40
Figure 28: Scenario 1, velocity vectors after 13.9 hr of simulation	41
Figure 29: Scenario 2, pressure contours after 61 days of simulation	43
Figure 30: Scenario 2, velocity vectors after 61 days of simulation	43
Figure 31: Scenario 3, pressure contours after 61 days of simulation	44
Figure 32: Scenario 3, velocity vectors after 61 days of simulation	44
Figure 33: Historical and simulated (scenario 3) heads for piez. R1P2	47
Figure 34: Historical and simulated (scenario 3) heads for piez. R2P2	47
Figure 35: Historical and simulated (scenario 3) heads for piez. R3P2	48
Figure 36: Historical and simulated (scenario 3) heads for piez. R4P2	48
Figure 37: Historical and simulated (scenario 3) heads for piez. R5P2	49
Figure 38: Historical and simulated (scenario 3) heads for piez. R5P2	49
Figure 39: A comparison between scenario 2 and 3 for piez. R4P2	50
Figure A.1: Seepage through an inclined sand filter	63
Figure A.2: Variations in $\Delta x$ within a conceptual soil structure	68
Figure A.3: Unknown pore configuration	69
Figure A.4: Computed $\bar{D}$ based on 45 soils as a function of the power n	73
Figure A.5: Water saturation versus pressure	77
Figure A.6: Relative permeability versus pressure	77

Figure A.7: Mass conservation for a control volume	79
Figure B.1: A quadrilateral element	83
Figure B.2: Basis function defined for quadrilateral elements	86
Figure B.3: Perspectives of basis function $\Omega_j(\xi, \eta)$ at node j	87
Figure B.4: Finite element in local coordinate system with Gauss points	91
Figure B.5: Geometry of example cell $i$	92
Figure B.6: Cells, elements, and nodes	96
Figure B.7: Temporal definitions	102

## NOMENCLATURE

$\alpha$	-Porous matrix compressibility
$\beta$	-Coefficient of compressibility of water
$\epsilon$	-Porosity
$\eta$	-Horizontal distance in a local coordinate system
$\nabla$	-The total spatial volume of the groundwater system
$\nabla_e$	-Elemental volume
$\nabla_{\text{total}}$	-Total volume of the porous medium composed of solid grains and void space
$\nabla_{\text{void}}$	-Volume of void space in total volume
$\nabla_{\text{water}}$	-Volume of water in total volume
$\gamma$	-Specific weight of water
$\Gamma$	-The surface of the region to be simulated
$\mu$	-Dynamic viscosity of fluid
$\nabla$	-Divergence operator
$\nu_p$	-The average medium conductance
$\Omega$	-Basis function within the local coordinate system
$\phi$	-Basis function within the global coordinate system
$\Psi$	-Number between -1 and 1
$\rho$	-Fluid density
$\sigma'$	-Intergranular stress
$\xi$	-Vertical distance in a local coordinate system

$a$	-Scaling factor
$A$	-Cross-sectional area
$A_e$	-Effective area
$A_{\text{sat}}$	-Pore area at saturation
$B$	-Thickness of the mesh within the $y$ -coordinate direction
$c$	-Shape factor
$C$	-Proportionality constant
$d$	-Mean grain diameter
$D$	-The mean square deviation between $k_{rm}$ and $k_r$
$\underline{g}$	-Magnitude of the gravitational acceleration vector
$gp$	-Gauss point number
$h$	-hydraulic head
$h_{\text{piez}}$	-piezometric head
$H_{gp}$	-Weighting coefficients
$\hat{\mathbf{i}}$	-Unit vectors in the $x$ coordinate directions
$\mathbf{I}$	-Mass inflow rate
$I_x$	-Mass inflow in the $x$ direction
$\hat{\mathbf{j}}$	-Unit vectors in the $y$ coordinate directions
$J$	-Jacobian Matrix
$k$	-Intrinsic permeability
$\hat{\mathbf{k}}$	-Unit vectors in the $z$ coordinate directions
$k_r$	-Relative permeability

$k_{rm}$	-Relative permeability found through experiment
$K$	-Hydraulic conductivity
$l$	-Unitless
$L$	-Length
$L_{\text{surf}}$	-Length of the ground surface boundary
$m$	-A factor used to account for the tortuosity of pores
$M$	-Constant which incorporates properties of the fluid and solid matrix
$M$	-Mass unit
$M_f$	-Total mass of fluid contained in a total volume.
$n$	-Accounts for effects of tortuosity and correlation factors
$\mathbf{n}$	-Normal unit vector
$N_{\text{surf}}$	-Total number of nodes on the ground surface boundary
$NN$	-The total number of nodes within the finite element mesh
$np$	-The total number of Gauss points
$\mathbf{O}$	-Mass outflow rate
$O_p$	-Governing equation representing the fluid mass balance
$O_x$	-Mass outflow in the $x$ direction
$p$	-Fluid pressure
$p_{\text{ATM}}$	-Atmospheric pressure
$p_c$	-Capillary pressure
$p_{\text{cent}}$	-Entry pressure

$p_i^*$	-Base case pressure head at node $i$
$p_i$	-Pressure head specified at node $i$
$p_{BC_i}$	-Pressure value specified within the ground surface boundary node
$p_{piez}$	-Pressure within the base of the piezometer
$p^{proj}$	-An estimate of fluid pressure at the end of the present time step
$P$	-A point located at the centroid of a control volume
$q$	-Mean seepage velocity of the fluid
$\mathbf{q}$	-Specific discharge
$Q$	-Rate of fluid flow
$Q_p$	-Fluid mass source term
$Q_{tip}$	-Instantaneous tipping bucket records
$r$	-Pore radius
$r_e$	-Effective radius
$R_p$	-A spatially varying residual value
RMSE	-Root Mean Squared Error
$s$	-Spatial Distance
$S_e$	-Effective saturation
$S_{op}$	-Specific pressure storativity
$S_w$	-Water saturation
$S_{wres}$	-A residual saturation below which saturation is not expected to fall
$t$	-Time
$T$	-Time unit

$u$	-Connectivity of pore structure
$\underline{v}$	-Average fluid velocity
$W_i$	-Weighting function in global coordinates
$x$	-Horizontal spatial distance within the global coordinate system
$y$	-Spatial depth within the global coordinate system
$z$	-Vertical spatial distance within the global coordinate system
$z_{\text{elev}}$	-Elevation of the piezometers base

## **INTRODUCTION**

Over the past decade, the U.S. Forest Service has monitored the subsurface hillslope flow of the E-road swale. The swale is located in the Caspar Creek watershed near Fort Bragg, California. Monitoring has consisted of piezometric measurements recorded every 15 to 30 minutes from well sites located throughout the swale and pipeflow measurements at 10 min intervals. In hydrologic year 1990 a logging road was built across the middle section of the hillslope followed by a total clearcut of the area during the following year.

Development of the logging road has resulted in a large build up of subsurface waters behind the road. The road behaves much like a dam, and road and slope stability are of major concern. Landslides commonly occur during rainstorms when soil saturation reduces soil shear strength. Pore water pressure is the only slope stability variable that changes over a short time scale, and theory predicts that a slope can become unstable as saturated thickness increases due to rainfall infiltration. Previous studies of subsurface hillslope flow indicate that very little is understood about the subject. Further studies in this area will only help to improve existing techniques in the design and maintenance of mountain roads.

This investigation employs a conceptual model to better understand the hydrologic mechanisms which govern the behavior of subsurface waters within a swale road system. A comparison is made between model simulations and historical E-Road pore pressures.

## **HISTORY OF HILLSLOPE GROUNDWATER MODELS**

Field investigations of subsurface hillslope flow have shown that piezometric response is sensitive to rainfall, soil porosity, topography, and vegetation. Swanston (1967) showed that there is a close relationship between rainfall and pore-water pressure development. As rainfall increases, pore-water pressure increases, rapidly at first, but at a decreasing rate as rainfall continues, reaching an upper limit determined by the thickness of the soil profile. Additional studies of shallow-soiled hillslopes during the wet seasons showed that there was little lag time between rainfall and piezometric response (Swanston, 1967; Hanberg and Gokce, 1992). Furthermore, Hanberg and Gokce (1992) showed that the rate of piezometric rise was dependent on porosity and rainfall rate. Keppeler et al. (1994) observed increases in pore-water pressure and soil moisture following logging.

Based on field evidence, Whipkey (1965), Hewlett and Nutter (1970), and Weyman (1970) suggested that the presence of inhomogeneities in the soil may be a crucial factor in the generation of subsurface stormflow. These inhomogeneities may either be permeability breaks associated with soil horizons that allow shallow saturated conditions to build up or as Harr (1977), Mosley (1979), and Beven (1980) suggest, inhomogeneities may be structural and biotic macropores in the soil that allow for very fast flow rates. With a significant portion of the total subsurface flow taking place in the macropores, a higher hydraulic conductivity will be perceived for the entire soil profile. In addition field studies of subsurface stormflow have shown that the direct application of Darcian flow to subsurface water in forested watersheds may not be realistic (Whipkey, 1965; Mosley, 1979).

Both analytical and numerical models of saturated hillslope subsurface flow have been developed using the nonlinear Boussinesq equation, also called the Dupuit Forchheimer equation. The second approximation of the Boussinesq (1904) equation, was modified by Bear (1972) to incorporate a non-horizontal bottom.

Bear (1972), Sloan and Moore (1984), and Buchanan et al. (1990) have all developed analytical solutions to predict piezometric response for subsurface saturated flow in a one-dimensional uniform slope. While these models describe oversimplified groundwater systems quite well, the analytical solutions are unable to describe anything complex in nature (e.g. a system found in the environment). However, attempts have been made to further develop an analytical model to handle complex transient recharge in a sloping aquifer of finite width (Singh et al., 1991).

A numerical model developed by Hanberg and Gokce (1992), modeled the full, one dimensional Dupuit-Forchheimer equation for a hillside with changing slope angle and transient rainfall. The predicted response rose with the historical observed response but receded more quickly. They hypothesized that seepage out of the bedrock lengthened the observed recession.

Reddi et al. (1990) numerically modeled saturated subsurface flow in the arial two-dimensional space with pressures averaged over the vertical depth of the aquifer. In the overall downslope direction the Dupuit-Forchheimer approach was used. Flow in the transverse direction was assumed horizontal and was not topographically driven. Their predictions differed significantly from field observations in timing and magnitude. The first physically-based numerical model to describe both partially saturated and saturated flow within a hillslope system was presented by Freeze

(1972a). Freeze developed a hillslope model to study baseflow generation in upland watersheds, and storm runoff processes (Freeze, 1972b). Earlier, Freeze (1971) had developed a single governing equation that encompasses both partially saturated and saturated flow. The successive over-relaxation technique, an iterative technique that employs implicit finite difference formulations, is used to solve the nonlinear parabolic partial differential governing equation. Later work by Freeze (1974) and Beven (1989) indicated the practical and theoretical limitations associated with modeling complex natural flow systems with simulation models. These include: parameter averaging, data uncertainty, spatial variability of important parameters, computer limitations, and discretization.

Dietrich et al. (1986) simulated two-dimensional steady-state flow in a hypothetical homogeneous hillslope using TRUST (Narasimhan et al., 1978). The model is a partially saturated - saturated hillslope model that utilizes an integral finite difference method, incorporating both infiltration partitioning and overland flow. They found that the pore pressure distribution was strongly dependent on both boundary conditions and slope geometry. Application of the TRUST model is additionally seen in the work of Wilson (1988) and Brown (1995). Wilson (1988) and Brown (1995) represented hillslope systems in both two and three dimensions. The two-dimensional systems represented the vertical cross-section from an upper to lower portion of the hillslope. The three-dimensional systems combined a number of vertical cross-sections to define the entire hillslope system.

Wilson (1988) found the hydraulic response was controlled by groundwater circulation patterns within the bedrock resulting from large-scale topographic controls

and small-scale heterogeneities in bedrock permeability. Brown discovered that a mixed explicit-implicit solver worked best for his study since it produced acceptable mass balance results and did not show significant oscillations for a range of materials. Model simulations using available field data were compared to field observations of rainfall pore-pressure responses and were found to be in reasonable agreement.

The finite difference approximation of subsurface hillslope flow is again seen in the work of Blain (1989) and Jackson (1992a). The hillslope subsurface system was characterized in the aerial two-dimensional space. Blain utilizes an upstream-weighted difference approximation of the spatial partial derivatives and a Crank-Nicholson approximation for the temporal pattern of soil moisture. Jackson simplifies the system by assuming streamlines parallel to the slope and the domination of saturated, subsurface flow. Additionally, the model has the capability to deal with convergent (or divergent) topography. They found that peak piezometric response was largely dependent on rainfall rate and the storage coefficient while the recession curve was influenced mainly by the hydraulic conductivity. The model was tested against piezometric response measured in a hillslope hollow and showed promising results.

The application of a finite element model to hillslope subsurface flow was first seen in the work of Calver (1988, 1989). Calver utilized a rainfall-runoff model, the Institute of Hydrology Distributed Model version 4 [IHDM4], developed by Beven et al. (1987). The Galerkin method of weighted residuals is used by the model for the two spatial dimensions while an implicit finite difference scheme is applied to the time dimension. Calver conducted both two and three-dimensional simulations

for hillslope catchments. The two-dimensional system consisted of vertical sections while the three-dimensional system required combining the vertical slices. Calver found that generally smaller elements were favored with a ratio of horizontal to vertical element dimension equal to 10. A temporal discretization of 0.5 hours was found to be the longest possible time step.

Flow and transport modeling within the hillslope subsurface environment was investigated by McCord et al. (1991) and Jackson (1992b). Both groups of modelers applied VAM2D (Huyakorn et al., 1989), a finite element model which simulates flow and transport in two spatial dimensions. Simulation results were then compared to field site tracer studies. McCord's results indicated that both soil type and anisotropy strongly affect unsaturated flow.

Brandes et al. (1998) conducted numerical modeling experiments to solve the steady state Richards' equation over a two-dimensional cross-sectional hillslope domain using the finite element model FEMWATER (Yeh, 1987). The system was characterized by (1) no-flow (Neumann) boundary conditions along the sides and base of the hillslope, (2) a variable infiltration-seepage boundary along the ground surface, and (3) a single constant head (Dirichlet) node at the foot of the slope representing a first-order stream. Brandes et al. looked at the model's behavior under steady-state precipitation with low initial antecedent soil conditions. Results from FEMWATER indicate that a decreasing unsaturated zone will provide stability within the numerics of the solution as the saturated zone increases. Furthermore, the hillslope system at or near complete saturation will exhibit instability.

## **DESCRIPTION OF FIELD SITE AND INSTRUMENTATION**

The E-Road swale, a moderately steep zero-order basin, is located within the headwaters of the North Fork Caspar Creek Experimental Watershed, in the Jackson Demonstration State Forest near Fort Bragg, California, USA (Figure 1) (UTM zone 10 E:438426 N:4356896). The north-facing swale has a youthful topography consisting of uplifted marine terraces that date to the late Tertiary and Quaternary periods (Kilbourne, 1986). The swale occupies an area of 0.40 hectares.

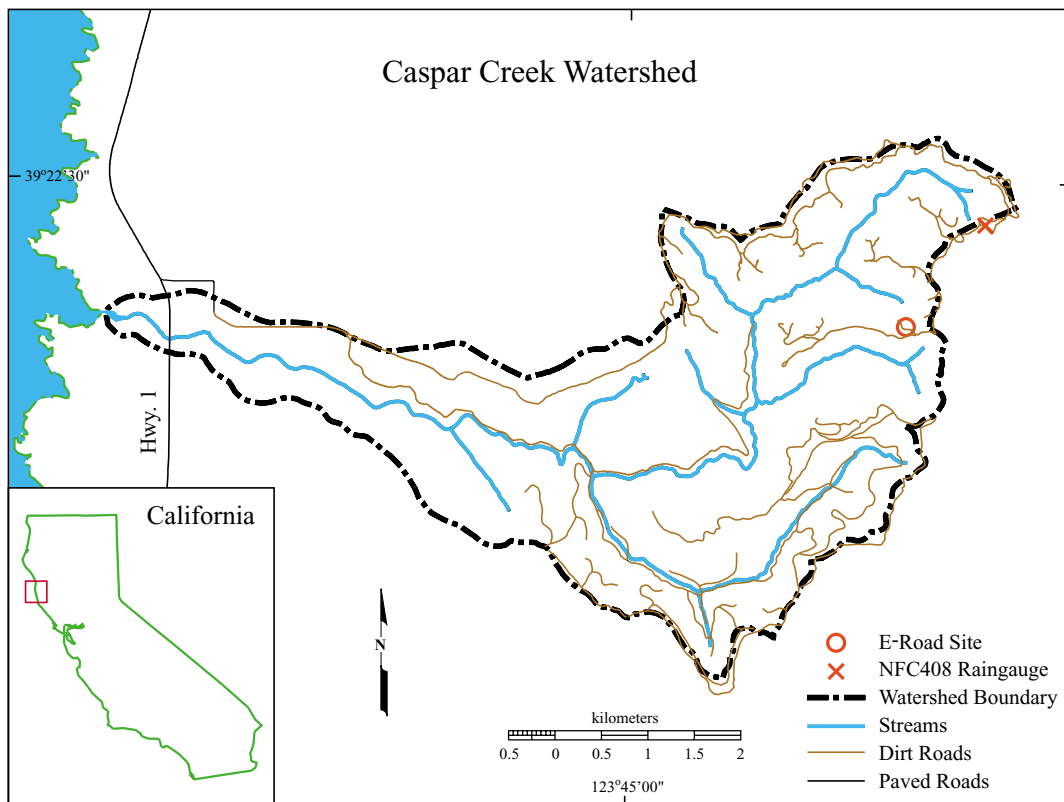


**Figure 1:** California, U.S.A., and location map of E-Road study site in the Caspar Creek Watershed.

Precipitation within the study area is characterized by low-intensity rainfall, prolonged cloudy periods in winter, and relatively dry summers with cool coastal

fog. Between October and April 90% of the 1190 mm mean annual occurs. Average monthly air temperatures between 1990 and 1995 in December were 6.7°C, with an average minimum of 4.7°C. Average July temperatures was 15.6°C, with an average maximum of 22.3°C (Ziemer, 1996).

The soil within the swale is the Vandamme series, a clayey, vermiculitic, isomesic typic tropudult, derived from sedimentary rocks, primarily Franciscan greywacke sandstone. Textures of the surface soil and subsoil are loam and clay loam respectively, with 35 to 45% clay in the subsoil (Keppeler, et al., 1994). The permeability within the soil is considered moderately slow (Huff et al., 1985).

Vegetation within the swale is dominated by Douglas-fir (*Pseudotsuga menziesii* [Mirb.] Franco), coast redwood (*Sequoia sempervirens* [D.Don] Endl.), grand fir (*Abies grandis* [Dougl. ex D.Don] Lindl.), western hemlock (*Tsuga heterophylla* [Raf.] Sarg.), tanoak (*Lithocarpus densiflorus* [Hook. and Arn.] Rohn) and Pacific madrone (*Arbutus menziesii* Pursh.).

The E-Road groundwater study began in hydrologic year 1990 and involved the monitoring of pipeflow and pore pressures within the swale. Instrumentation for piping and pore pressures was installed in the fall of 1989. During the winter of 1990, pre-disturbance monitoring took place until a seasonal road was constructed across the swale in the summer of 1990. Tree removal required for road construction was implemented using skyline cable yarding. In late-summer 1991, the timber in the remainder of the swale was harvested using tractor yarding above the road and long-lining below. In late November 1991, broadcast burning took place. Due to the north-facing aspect of the swale, fuel consumption was incomplete. Three-

dimensional surface renderings of the E-Road swale both before and after road-building are shown in Figures 2 and 3 respectively.

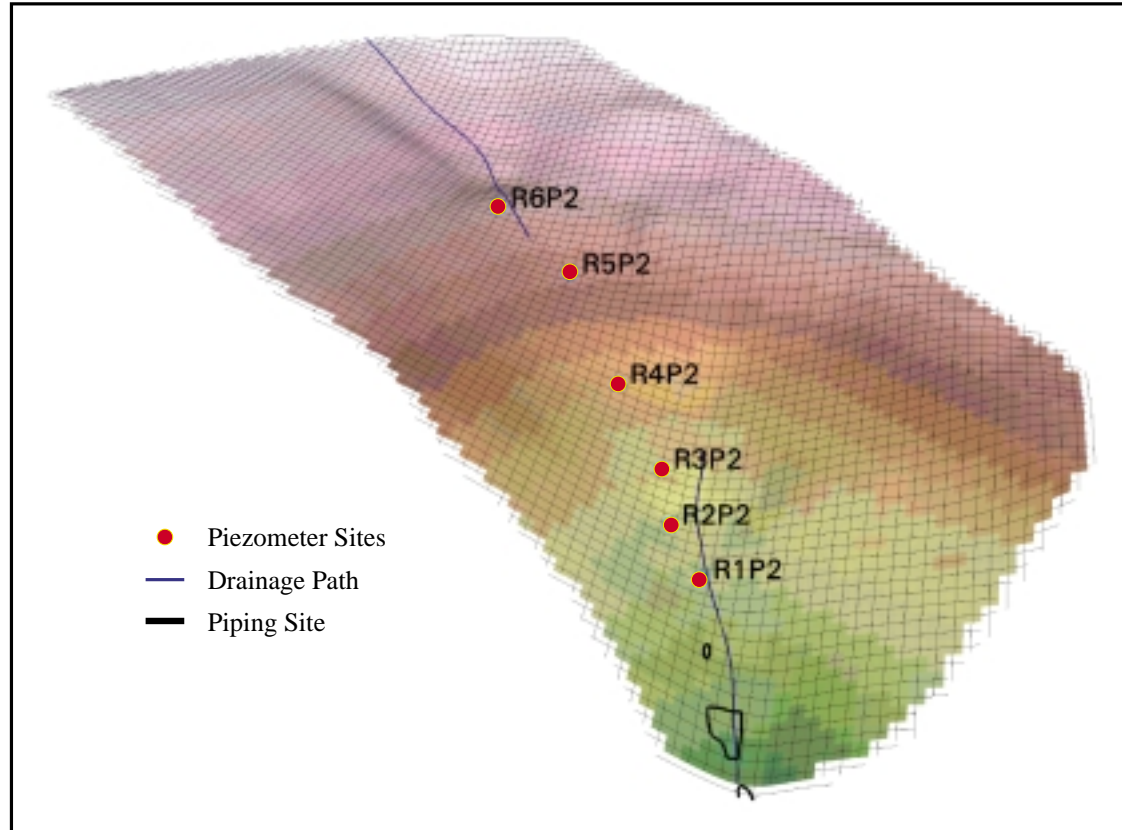


**Figure 2:** 3-dimensional rendering of E-Road swale, before road construction.

A topographic map of the swale, after road construction, is shown in Figure 4. The hillslope ranges from 3% to 35% with an average slope of 19% (Figure 5). Elevations within the study area range from 95 m to 128 m above sea level. Road fill depth is 3 m at its maximum, 2 m at the centerline, 1.6 m at R3P2, and less than 1 m at R2P2.

Inflow into the zero-order basin is limited to precipitation and fog drip. The routing of precipitation is given in Figure 6. The precipitation and fog drip that infil-

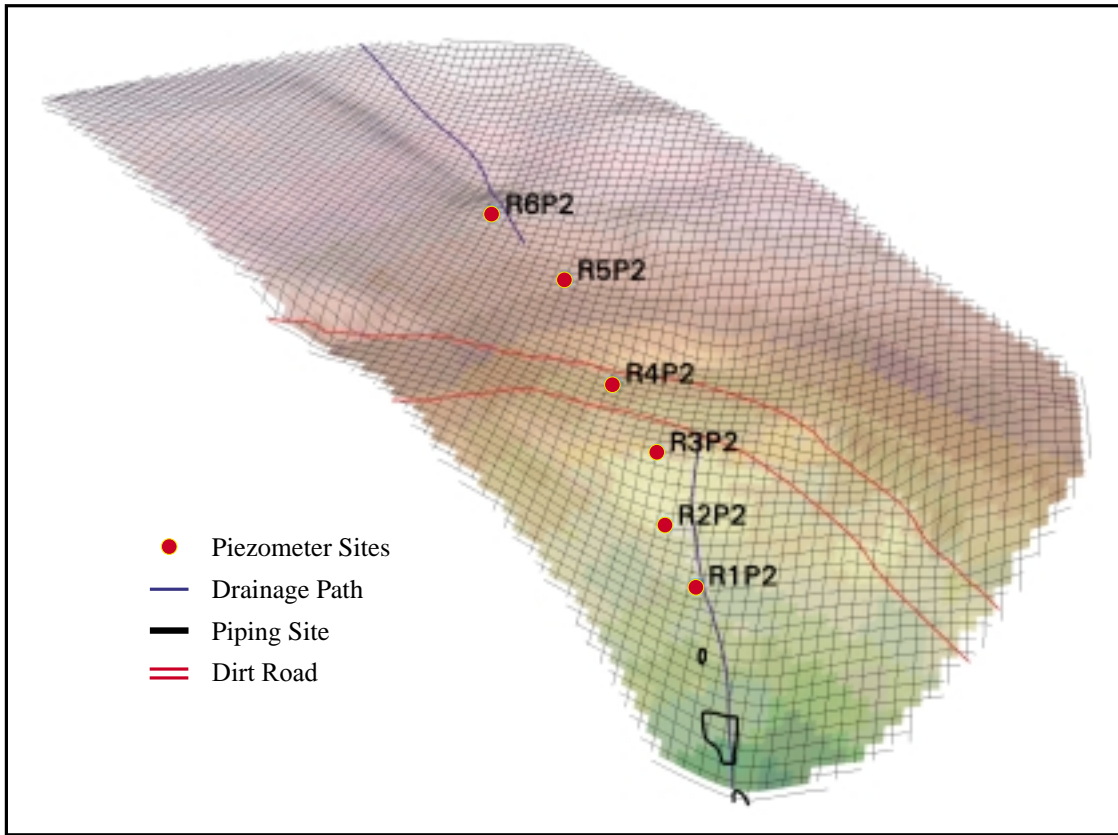


**Figure 3:** 3-dimensional rendering of E-Road swale, after road construction.

trates into the subsurface environment is transported both through micropores and macropores. Laminar micropore flow takes place within the soil matrix, a porous medium of mineral and organic particles. Macropore flow occurs in void diameters of 1 mm or larger. The geometry and type of macropore vary with depth below the land surface and arise from various biologic and soil forming processes (Keppeler and Brown, 1998) (Figure 7). Larger void diameters and connectivity among voids result in higher flow rates. The erosive behavior of the higher flow rates results in the generation of pathways. These pathways extend within the shallow subsurface horizons as continuous or interconnected conduits forming complex branching net-

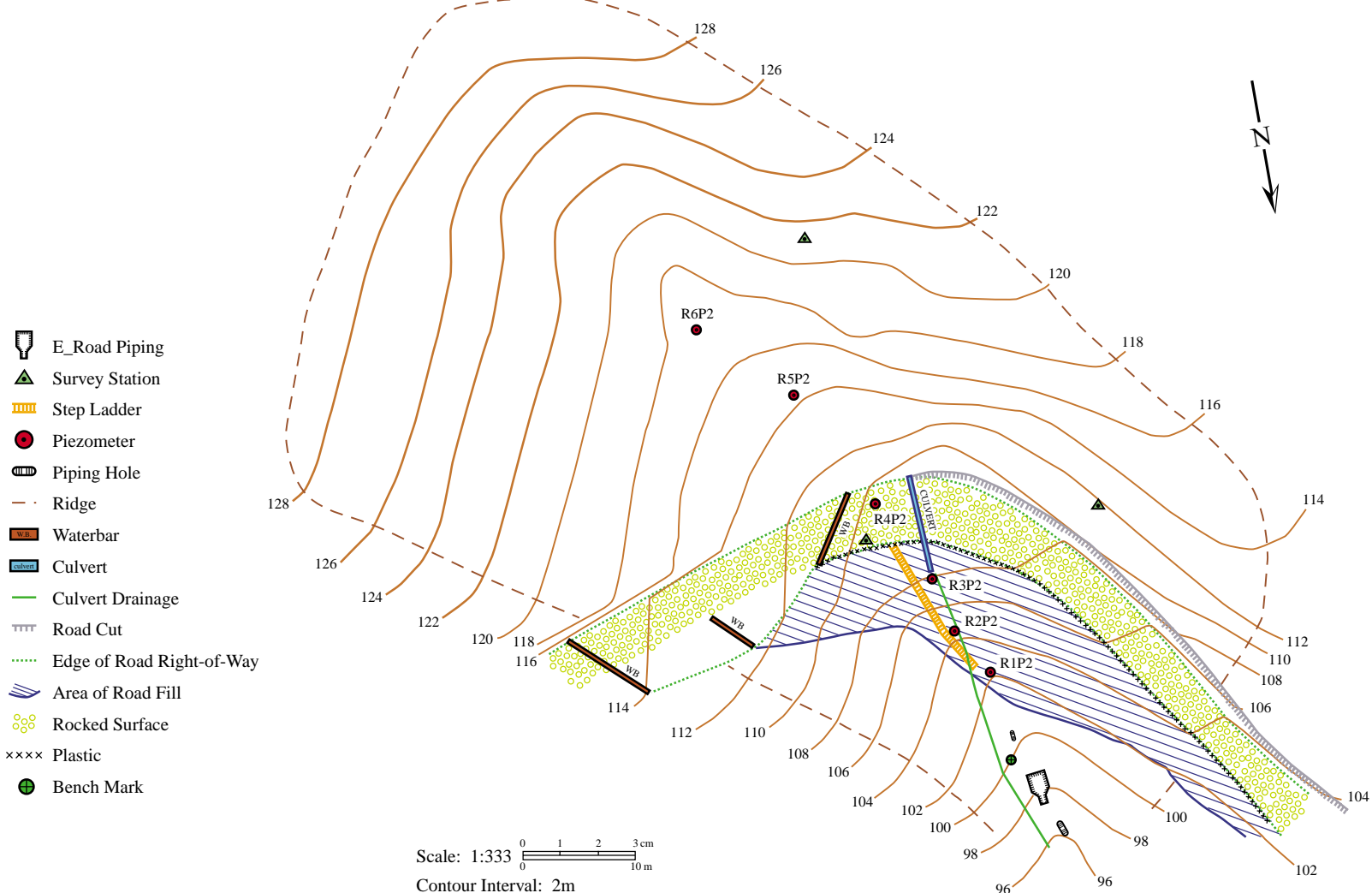


**Figure 4:** Topography of E-Road swale, post road building.

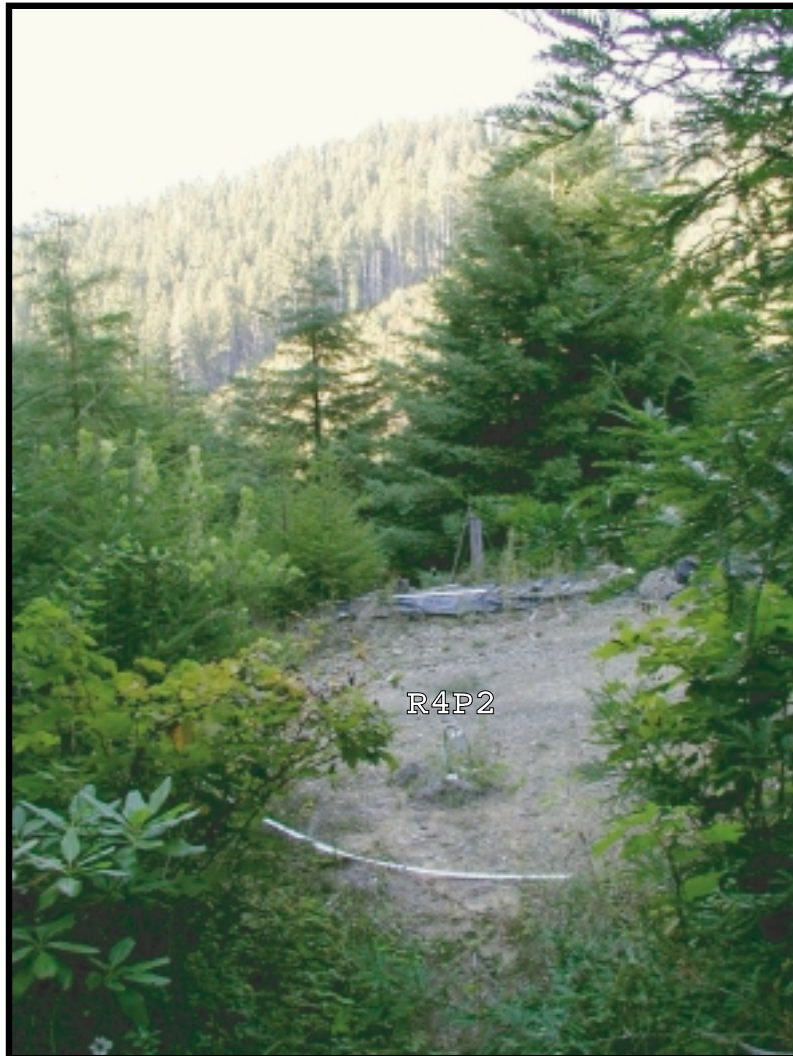


**Figure 5:** E-Road during the summer of 1999.

works (Albright, 1992). Pipeflow is that flow which takes place through conduits 2 cm or greater in diameter.

For the duration of the E-Road study, data collected have included pipeflow, pore pressure, and rainfall data. Collection methods and instrumentation for each type of data are discussed below.

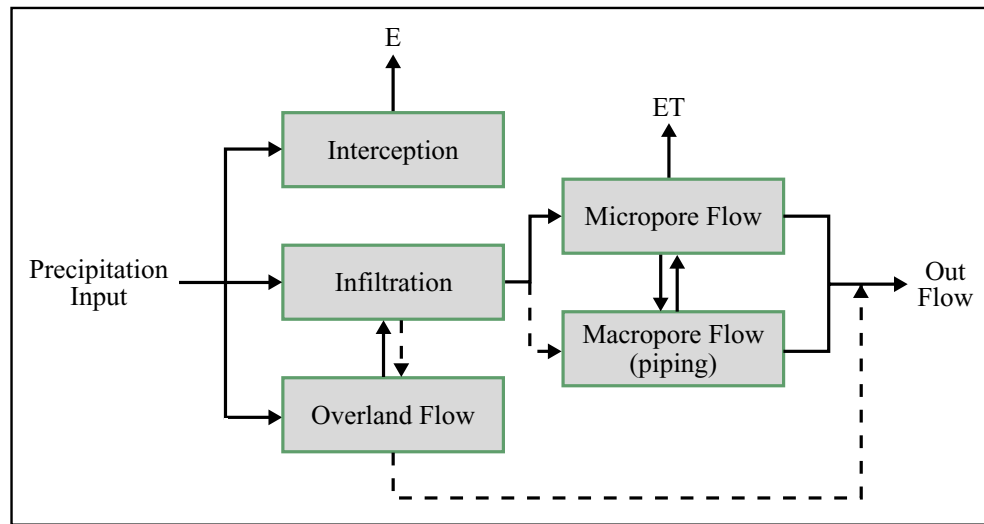


**Figure 6:** Distribution of precipitation input within the E-Road swale system where "E" is Evaporation and "ET" is Evapotranspiration. Dashed lines indicate transport mechanisms rarely observed within the E-Road swale.

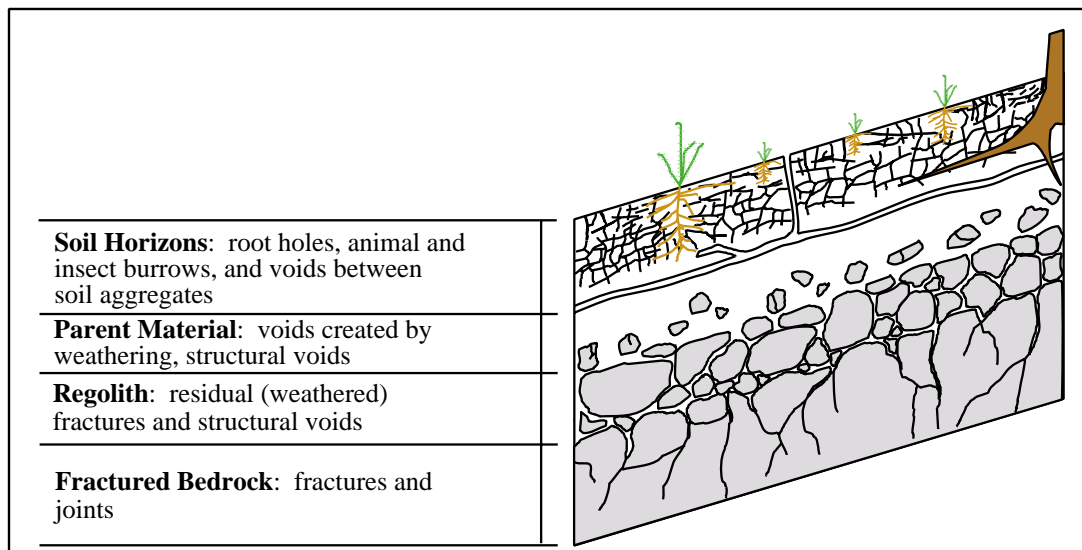


**Figure 7:** Hypothetical hillslope cross-section with characteristic voids and flow path variations (Brown, 1995).

## Piping

Excavation of a near-vertical soil face at the base of the E-Road swale allowed for the capture of pipeflow and soil matrix discharge (Figure 8). Two soil pipes were discovered upon excavation of the soil face. The larger of the two pipes, 9 inches in diameter, flows perennially while flow in the smaller pipe, 2 inches in diameter, is limited to the winter season. The captured flow from each pipe is routed through a plumbing network into a standpipe container and the standpipe stage is continuously monitored. Drainage holes, drilled in a pattern lengthwise along the side of the container, are shown in Figure 9. Each container was calibrated to establish a relationship between container stage (water depth) and pipe discharge (Ziemer, 1992). Manual discharge measurements were periodically collected in the field to verify the standpipe container calibrations. Stage measurements within the pipe are made with a pressure transducer placed at the bottom of the standpipe container. Transducer stage levels were recorded by a data logger (Omnidata Easy Logger) at 10 min intervals during the winter season and 30 min intervals during the low-flow season. Due to the instability of the pressure transducer under heavy flows, the piping data is not presented here in its entirety.

## Pore Pressure

Pore pressure response to rainfall was observed using six piezometers; R1P2, R2P2, R3P2, R4P2, R5P2, and R6P2 (Figure 10). Installation of the piezometers involved hand augering 10 cm diameter holes through the soil profile. A PVC pipe, the length of the augered hole, was slotted with a hacksaw within the lower 15 cm of

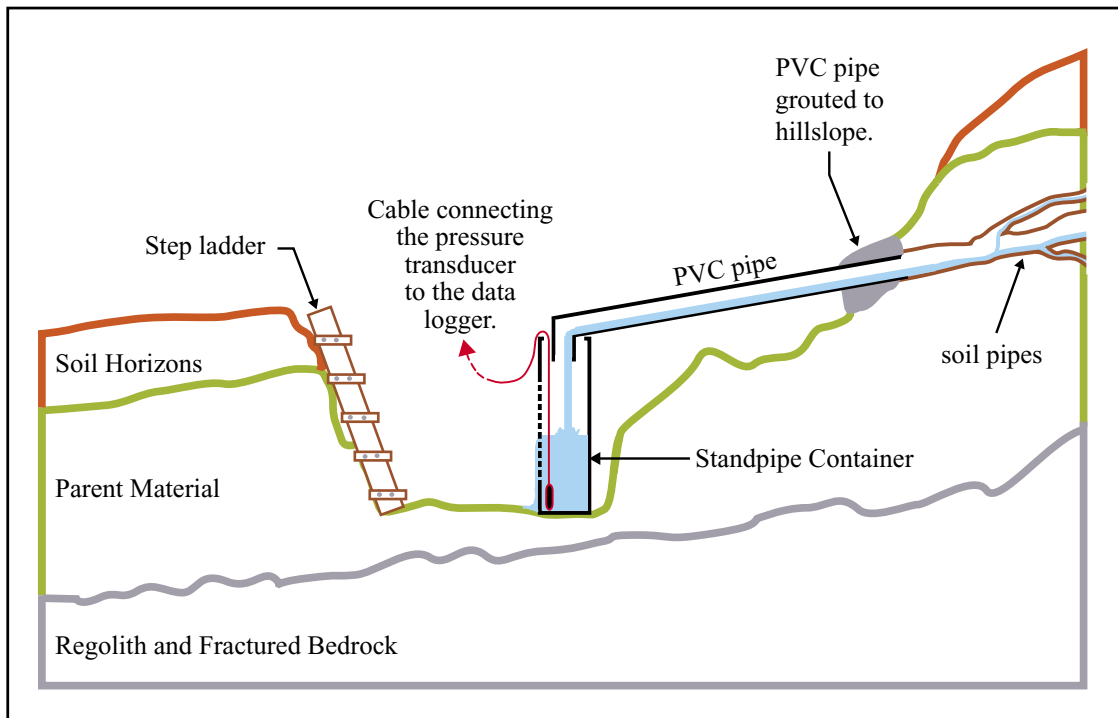


**Figure 8:** Method for the collection of piping data.

the pipe. After wrapping the slotted portion of the pipe with a plastic mesh screen, the entire pipe was lowered into the augered hole. The pipe was then backfilled with approximately 25 cm of pea gravel, 15-20 cm of bentonite, and excavated soil. Depth of the augered holes was limited by the physical limit of the hand augering device. At some sites, rock fragments in the lower saprolite prevented the auger from reaching bedrock (Keppeler and Brown, 1998). The water level within the pipe was measured with a pressure transducer and electronically recorded by data logger. Fluid pressures are recorded at 15 min intervals during the winter and 30 min intervals during the summer months. Manual stage measurements were periodically taken with a hand-held water level detector to validate pressure transducer data. Figures 11 and 12 show water levels for each of the piezometers over time. Maximum



**Figure 9:** PVC standpipe container collects soil pipeflow discharged from hillslope.

pore pressures are summarized in Table 1.

The first year (HY 1990) of the study experienced a moderate rainfall total with flashy pore pressure responses in the lower piezometers (R1P2, R2P2, R3P2) and little activity within the upper piezometers (R4P2, R5P2, R6P2). The single year of pre-treatment data left little information available for a pre-disturbance analysis. During the first winter after road building (HY 1991), pore pressure response continued its trend with spiky activity in the lower piezometers and upper piezometers remaining dry. A low rainfall total for hydrologic year 1991 may partially explain the inactivity of the upper piezometers.

After tractor logging was completed late in 1991, the piezometric response to

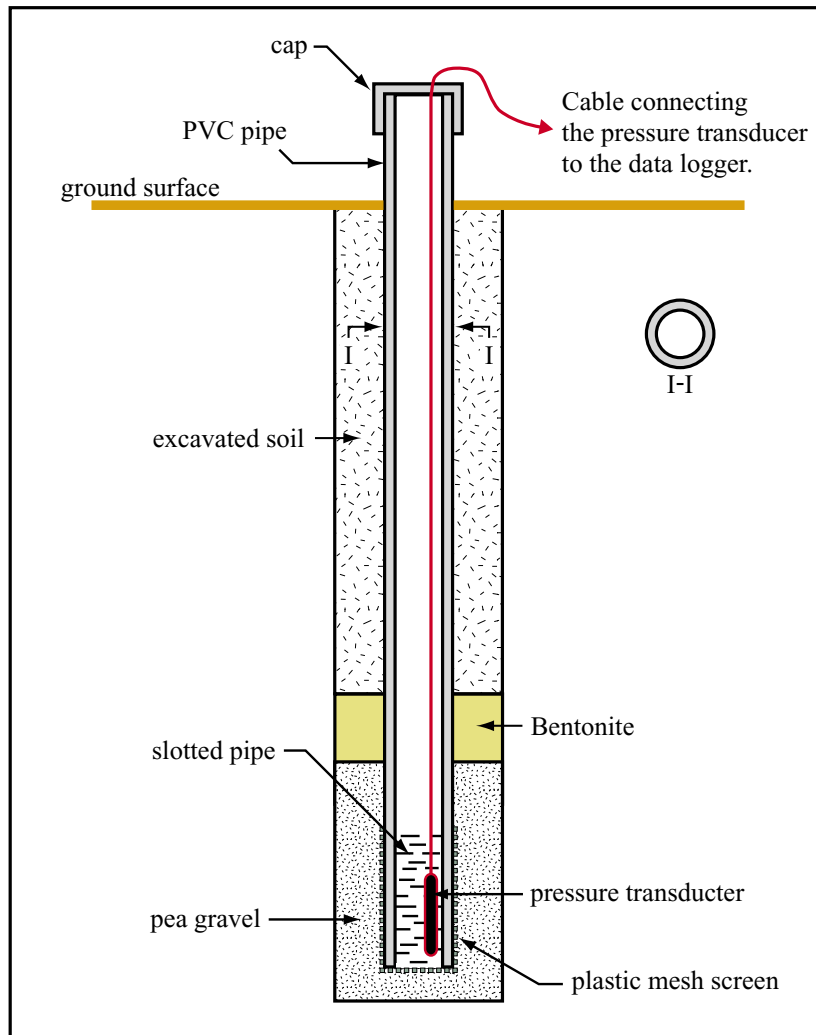


**Figure 10:** Method for the collection of piezometric data.

precipitation showed sharp increases in water levels in and above the road followed by a quick recession. Drainage within the upper piezometers saw water levels return to baseline conditions following a rainfall event. Drainage patterns below the road were unchanged. No piezometric response was detected within R4P2, R5P2, and R6P2 until after logging.

The spiky response of the upper piezometers in hydrologic year 1992 is attributed to ground disturbances experienced during the logging of the swale (i.e.

the collapse of soil pipes beneath the roadbed). Damage to the established piping network directly affects the swales ability to drain. Following the clearcut, rainfall events act to re-establish the damaged pipe network. Pore pressures, up-slope from a collapsed pipe, increase until pressures are sufficient enough to reshape the piping network. New soil pipes are formed within the patchwork of collapsed pipes allowing for an increase in drainage rates.

In hydrologic year 1993, a high rainfall year, the fluid pressure response to discrete rainfall events changed drastically within the upper piezometer holes. Their flashy response was now superimposed on an annual rise-fall cycle. The compounding of pore pressures throughout the winter months indicates a groundwater buildup behind the road which is assumed to result from the consolidation of road bed materials and a consequent decrease in drainage rates beneath the road surface. The magnitude of groundwater buildup is both a function of the annual precipitation total and the antecedent precipitation index (API) entering into the winter months.

Low rainfall for hydrologic year 1994 saw a decrease in groundwater buildup in and above the road; however, the compounding response was still evident throughout the year. From hydrologic year 1995 to 1998 the E-Road swale experienced much higher annual rainfall totals. The response of the system to increased precipitation was a clear buildup of groundwater behind the road during the winter months followed by the gradual drainage of the system throughout the summer months. In hydrologic year 1998 the swale received 88 inches; the highest annual rainfall total. The response of pore pressures beneath the road to elevated precipi-

tation levels resulted in a record water level of 6.42 m for piezometer R4P2 (Table 1). The increase in fluid pressure beneath the road, arguably the weakest portion of the hillslope (road-fill), raises the potential for hillslope failure. Water levels within R4P2 have never returned to pre-disturbance levels.

**Table 1:** Annual maximum pore pressures within the E-Road piezometers. NR indicates that no positive pressure head was observed during that year.

Hydro Year	Water level with respect to piezometer hole depth (m).						Rainfall Total (in)
	R1P2	R2P2	R3P2	R4P2	R5P2	R6P2	
1990	0.37	1.31	2.11	0.77	NR	NR	44.73
1991	0.57	1.71	3.39	0.63	NR	NR	28.75
1992	0.65	1.91	6.05	6.03	2.97	6.45	36.56
1993	0.61	2.09	4.24	4.61	4.77	4.18	62.77
1994	0.42	2.12	4.29	3.89	3.97	6.56	34.41
1995	0.52	1.92	4.50	5.25	4.72	7.49	63.55
1996	0.46	1.88	4.49	4.69	4.84	6.76	51.88
1997	0.45	1.80	5.59	4.07	4.93	6.04	51.42
1998	0.48	1.84	4.53	6.42	4.90	7.41	87.98
Max. Pore Pressure (m)	0.65	2.12	6.05	6.42	4.93	7.49	
Hole Depth (m)	1.37	2.59	6.35	7.66	5.69	7.83	
Base Elevation (m)	101.01	101.53	101.57	102.31	108.79	109.74	

## Rainfall

Rainfall is monitored with the NFC408 tipping bucket rain gauge (UTM zone 10 E:439243 N:4357978) located 1.335 km north-east of the E-Road swale. Data collection is instantaneous with each tip recording 0.01 inches of rainfall. An Onset data logger is used to electronically record tip times. Figures 11 and 12 show daily rainfall totals for hydrologic years 1990 through 1998 with annual rainfall totals summarized in Table 1.

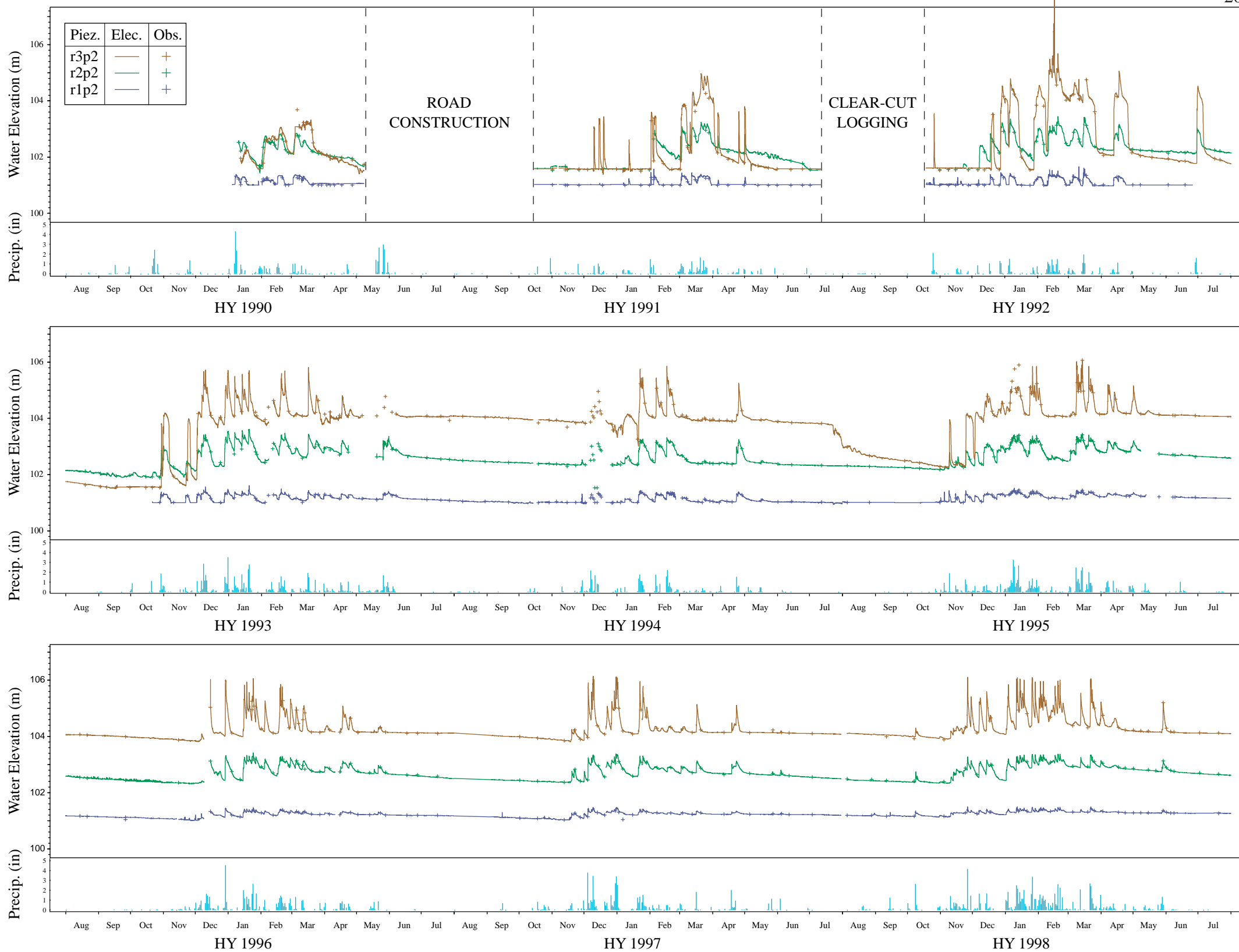


Figure 11: Historical piezometric responses for R1P2, R2P2, and R3P2.

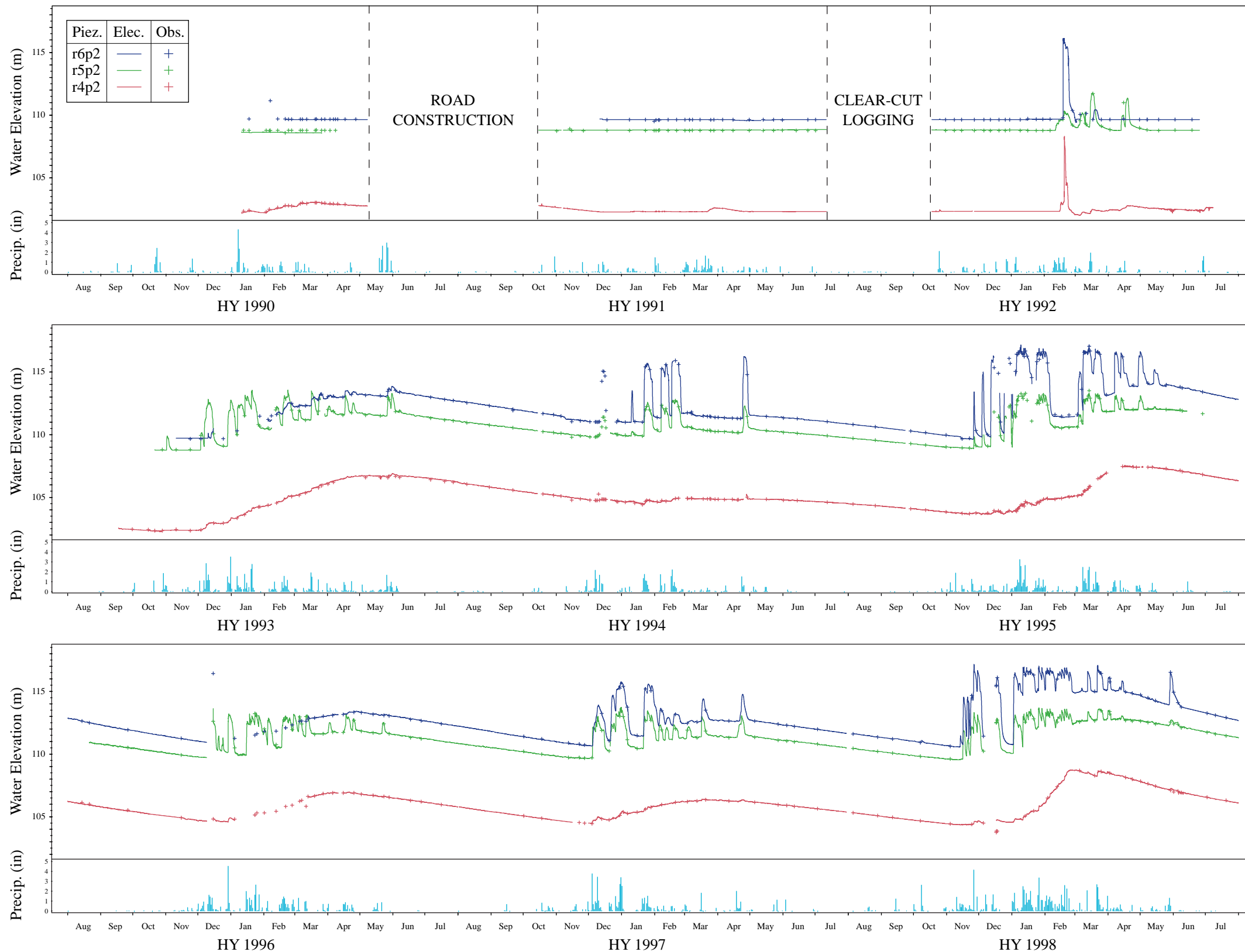


Figure 12: Historical piezometric responses for R4P2, R5P2, and R6P2.

## **MODEL FORMULATION AND DEVELOPMENT**

Development of a two-dimensional model required a simplification of the swale system. In Figure 13, a profile line was established through the center of the swale connecting each of the piezometer sites. Both upper and lower segments of the profile follow the swale's drainage path. A vertical cross-section established along the profile line allowed for a two dimensional (2-d) hypothetical profile view of the hillslope (Figure 14), where elevation is measured in the vertical coordinate direction. Representation of the swale system in two dimensions neglects the effects of convergent flow.

Fluid flow within the 2-d model is limited to the horizontal ( $x$ -axis) and vertical ( $z$ -axis) directions with pore pressures averaged over the thickness ( $y$ -axis) of the system. The error associated with a 2-d representation of a 3-d system is not easily quantified in a complex environmental system such as the E-Road swale. However, future investigations may address the error associated with neglecting convergent flow by comparing 2-d and 3-d numerical representations of the E-Road system.

Evapotranspiration, interception, and pipeflow are additional hydrologic mechanisms unaccounted for by the model. A reduction in rainfall is assumed to partially account for evapotranspiration and interception. Pipeflow, however, is not as easily accounted for by the model. The governing equation, describing groundwater flow within the system, is built upon the assumption of laminar flow. Flow within soil pipes is turbulent and little is known about the spatial distribution of soil pipes within the E-Road swale. Impacts associated with neglecting pipeflow are not clearly understood. The importance of pipeflow is, however, a major hydrologic

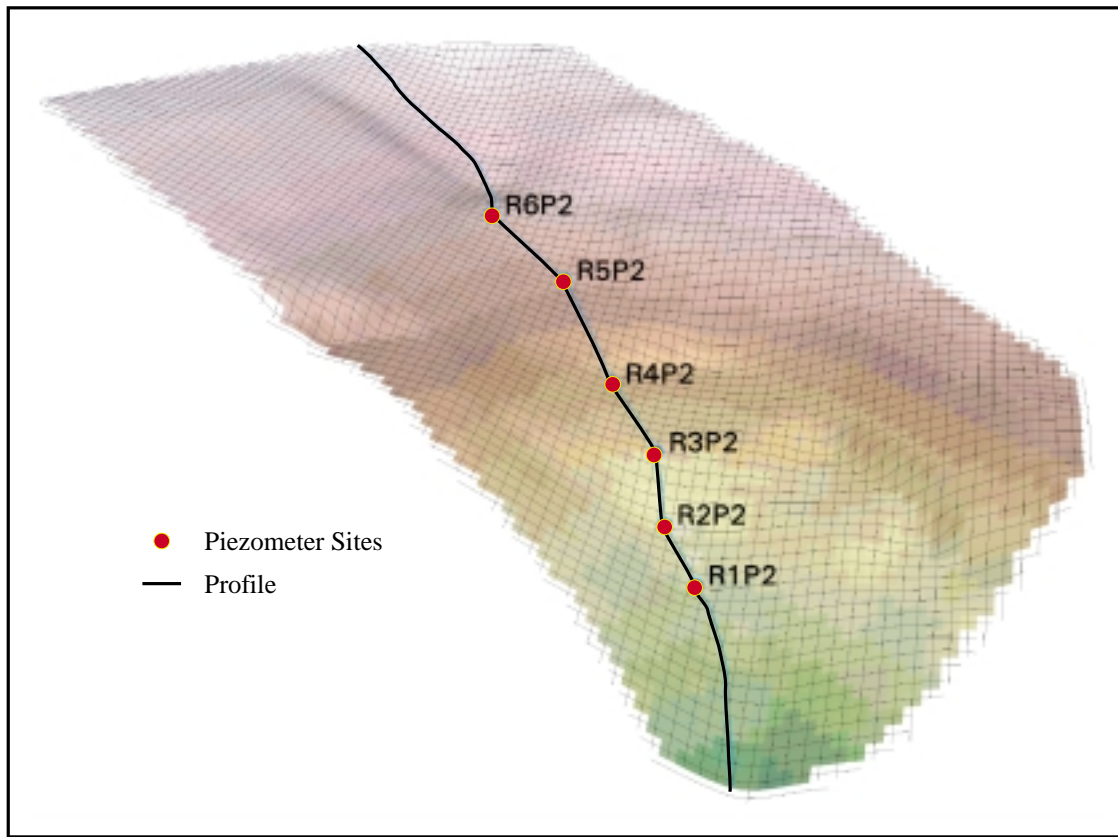


**Figure 13:** 3-dimensional rendering of E-Road swale, after road-building, with profile connecting piezometer sites.

mechanism within the swale system. Studies conducted for similar swale systems within the Caspar Creek watershed attribute 99% of the total swale discharge to pipeflow (Ziemer, 1992). The inability of infiltrating waters to enter a piping system is expected to translate into slower drainage rates within the swale. The purpose of applying the numerical model is not to exactly represent the E-Road historical behavior, but rather to aid in understanding the mechanisms which govern subsurface flow within a swale-road system.

A shortage of information within the subsurface environment required making certain assumptions about the geometry and depth of subsurface material layers.

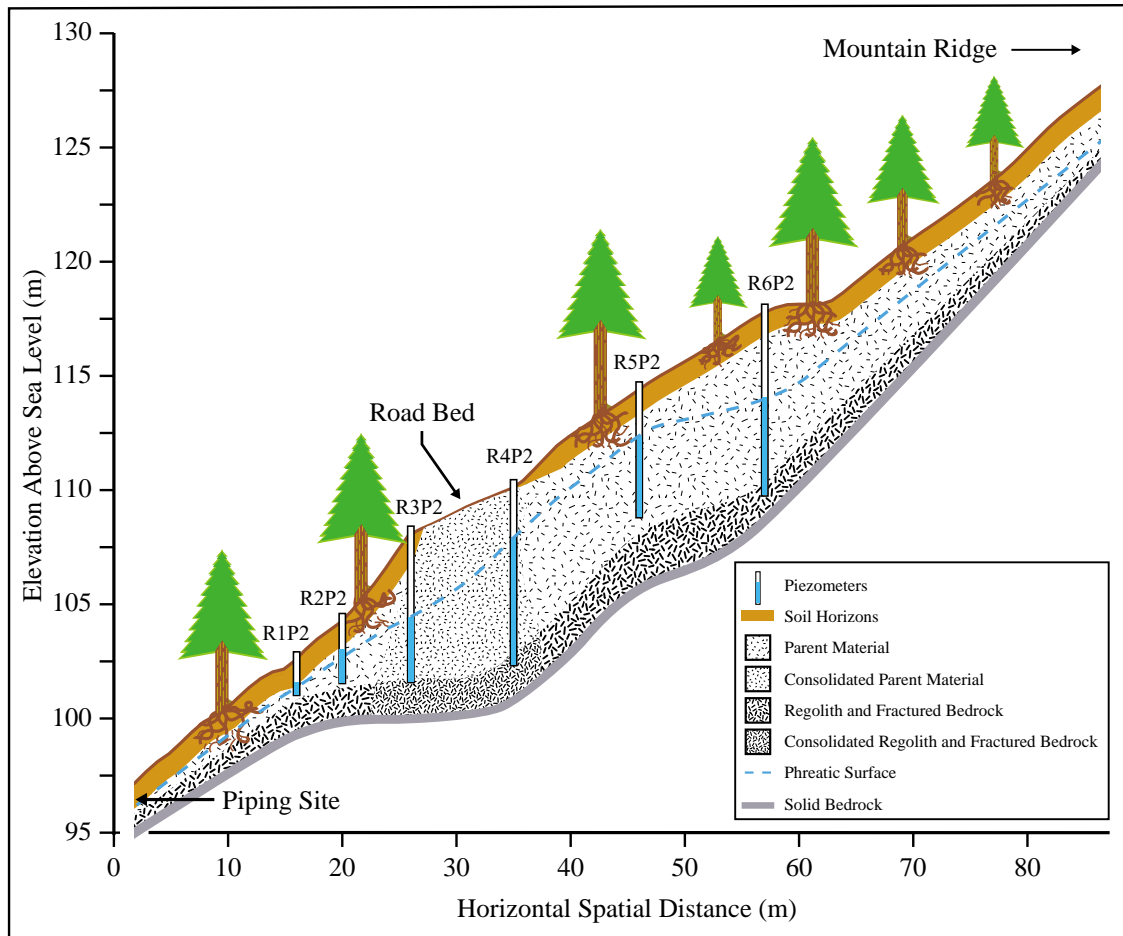


**Figure 14:** Hypothetical vertical profile of E-Road system.

Placement of the regolith layer was aided with depth measurements for each of the piezometers. It was assumed that the physical limitations associated with the hand augering device put piezometer hole depths at the interface between parent and regolith materials. Segmentation of the subsurface into zones of differing material type (i.e. soil horizons, parent material, and regolith-fractured bedrock) allowed for the allocation of subsurface parameters (e.g. permeability and porosity). In addition, materials are assumed to be consolidated beneath the road surface, because of logging operations, vehicle traffic, and road fill mass.

The numerical model selected to characterize the groundwater system is SUTRA (Voss, 1984). SUTRA is a FORTRAN program that simulates density-dependent, variably saturated or unsaturated, groundwater flow. The model employs a hybrid finite-element and integrated finite-difference method to approximate the governing equations for subsurface flow. The model was selected because of its ability to simulate a partially saturated environment. Derivation of the governing equations may be found in Appendix A and B of this report.

The boundary conditions for the cross-sectional model are shown schematically in Figure 15. Both the upper vertical boundary, located near the mountain ridge, and bedrock boundary are specified as no-flux Neumann boundary conditions. The ground surface is additionally a Neumann boundary condition, however, an input flux is specified for precipitation, with fluid pressure represented as a function of rainfall. At the base of the swale, located within the piping soil face, lies a vertical Dirichlet boundary condition with hydrostatic pressures set constant over time.

Each of the systems boundaries is an approximation of the real world conditions. The error introduced with the approximation results from a simplified representation of a complex boundary condition. For example, setting hydrostatic pressures along the pipeflow boundary neglects the functional relationship between the boundary pressures and the moisture content within the system.

Specification of the boundary conditions, finite-element mesh, and model parameters was aided with Argus ONE (ArgusONE, 2000) and its plug-in extension, SUTRA-GUI (USGS, 2000). Argus ONE is a commercially available, general purpose graphical Pre- and Post-Processor for the numerical modeler. The power of

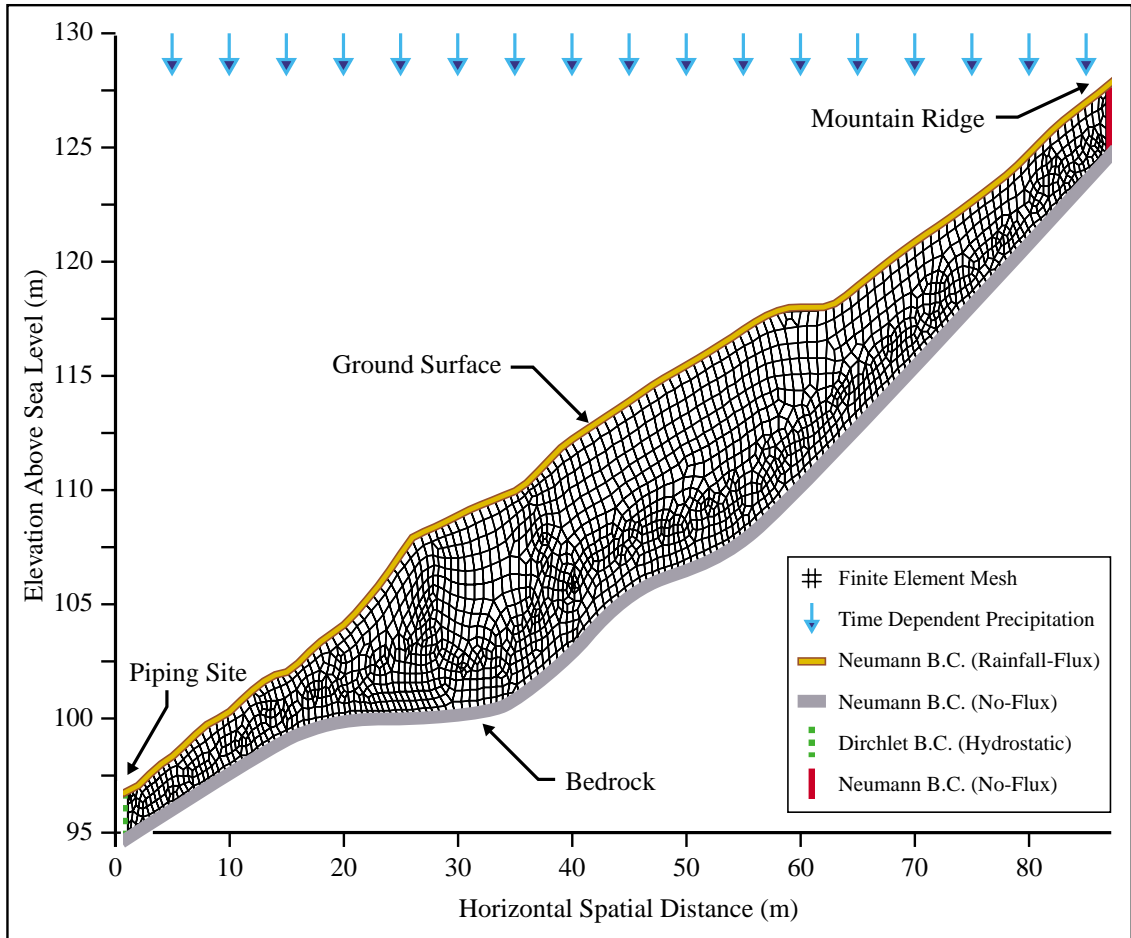


**Figure 15:** Discretization and boundary conditions.

Argus ONE is in its ability to generate robust finite-element meshes within complex topographic boundaries. SUTRA-GUI, a public domain Graphical User Interface (GUI) developed by the USGS for SUTRA, uses Argus ONE to automatically prepare SUTRA input files and to provide immediate visualization of simulation results.

A note is made of the computational tools utilized for the E-Road modeling investigation. Simulations as well as pre- and post-processing were performed on a PC, running Windows NT version 4.0 (service pack 6), with the following specs: one

ABIT BP6 Dual Socket 370 Celeron 440BX AGP 3xDIMMs ATX motherboard, two Boxed Intel 366MHz Celeron PPGA Processors with 128KB L2 cache (each processor was over clocked to 500MHz), and one 16Mx64 3.3V SDRAM 168-pin DIMM PC100 (128 MByte). Model simulations were run using the Microsoft Developer Studio 97 (Visual Fortran Professional Edition 5.0A.)

## **DESCRIPTION OF MODEL SCENARIOS**

A working model to describe the E-Road system was developed in three, increasingly complex scenarios. Each phase, represented as a simulation scenario, builds upon the complexity of the previous phase.

### **Scenario 1: Homogeneous and Isotropic**

The first scenario, shown in Figure 16, consists of a homogeneous and isotropic E-Road groundwater system. The ground surface boundary is specified as a no-flux Neumann boundary condition. Furthermore, without a rainfall flux, Scenario 1 is restricted to drainage simulations. Initial pressures within the system at  $t = 0$  reflect a totally saturated system. This scenario is used to investigate the model's sensitivity to changes in parameters.

### **Scenario 2: Nonhomogeneous with Active Ground Surface Boundary**

The second scenario, shown in Figure 17, is a nonhomogeneous system that builds upon Scenario 1 with three additional components. First, intrinsic permeability zones are established for the soil horizons, parent material, and regolith and fractured bedrock. Secondly, a rainfall flux,  $Q_p$ , is added across the ground surface boundary. Converting instantaneous tipping bucket records,  $Q_{\text{tip}}$ , from inches to meters per second required

$$Q_p = \frac{(Q_{\text{tip}})(0.0254 \frac{\text{m}}{\text{in}})(L_{\text{surf}})(dy)}{(\Delta t)(N_{\text{surf}})} \quad (1)$$

where  $L_{\text{surf}}$  is the length of the ground surface boundary [m],  $dy$  is the width of the system within the  $y$ -coordinate direction (set constant at 1 m),  $\Delta t$  is the

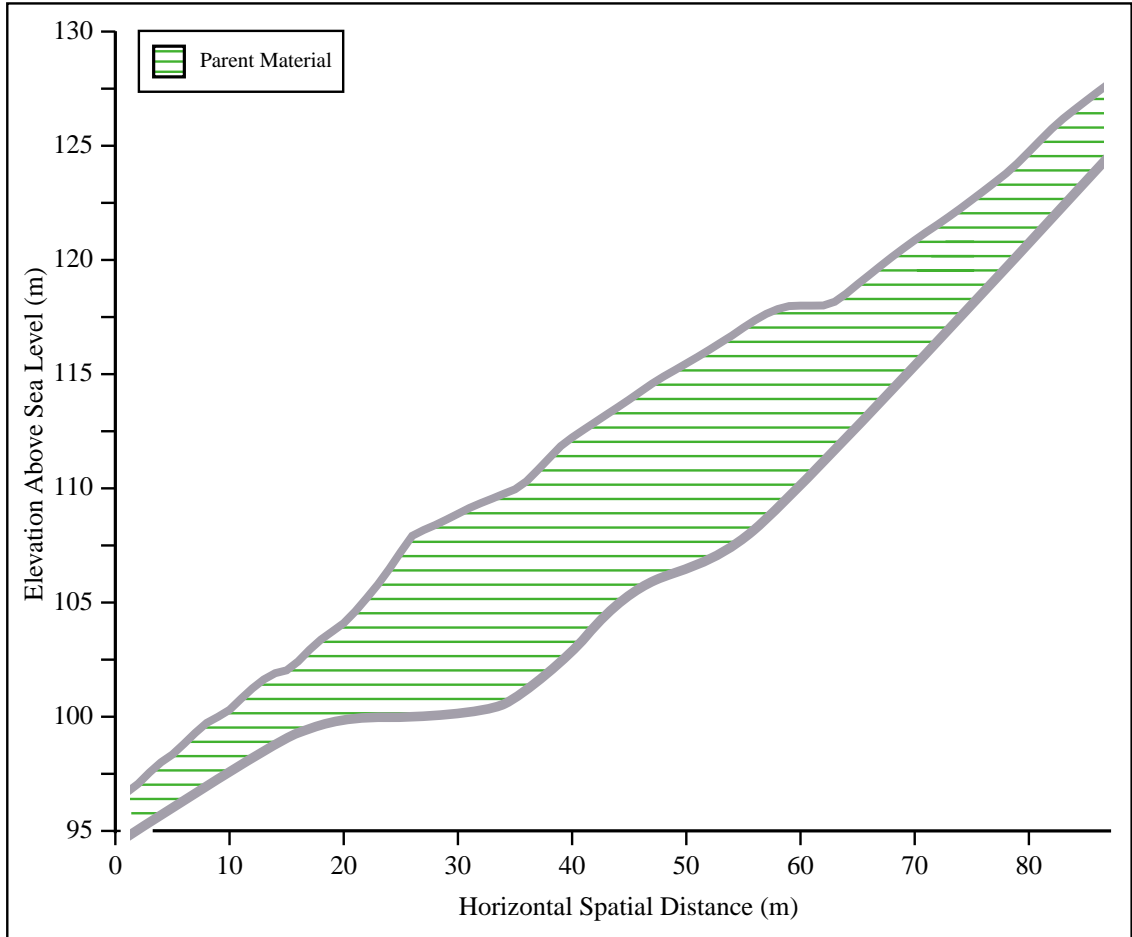


**Figure 16:** Scenario 1, permeability zone with ground surface boundary.

uniform time step [s], and  $N_{\text{surf}}$  is the total number of nodes on the ground surface boundary [ $l$ ]. The third additional component of Scenario 2 is a time-dependent switch, established for pressure values specified within the ground surface boundary nodes. The conditional statement for pressure at a given time step,  $n$ , within the boundary is

$$p_{\text{BC}_i}^n = \begin{cases} 0 \text{ Pa}, & \text{Rainfall} \\ -5000 \text{ Pa}, & \text{No Rainfall} \end{cases} \quad (2)$$

where pressure is set to  $-5000$  Pa (equivalent to a residual saturation of 7% [Figure

A.5]) for time periods of no rainfall, and atmospheric (gauge) pressure for periods of rain. At atmospheric pressure, a spatial node is considered totally saturated,  $S_w = 100\%$ . Initial pressures within the system at  $t = 0$  reflect a partially drained system.

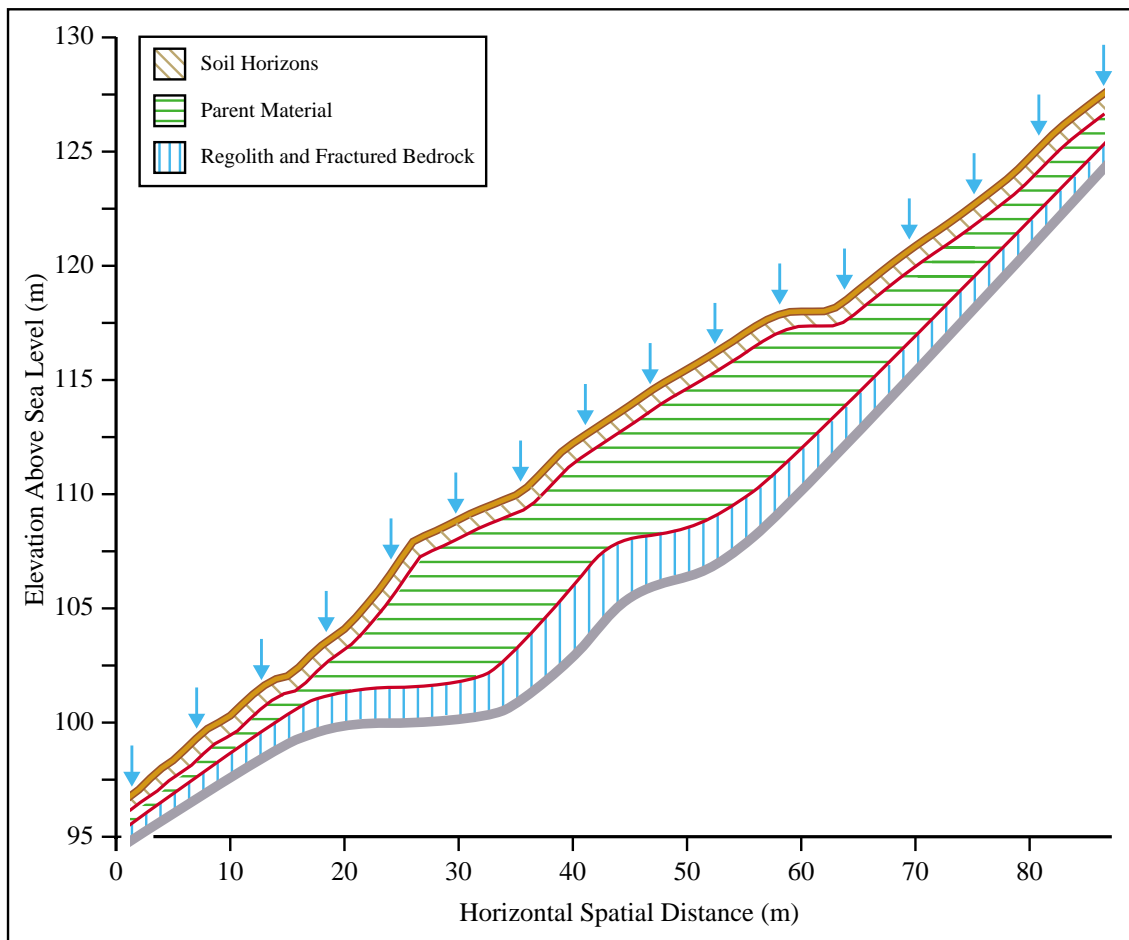


**Figure 17:** Scenario 2, permeability zones with active ground surface boundary.

### Scenario 3: Road Consolidation

The third scenario, shown in Figure 18, builds upon scenario 2 with the establishment of low intrinsic permeability zones beneath the road surface and the removal of the soil horizon at the road surface.

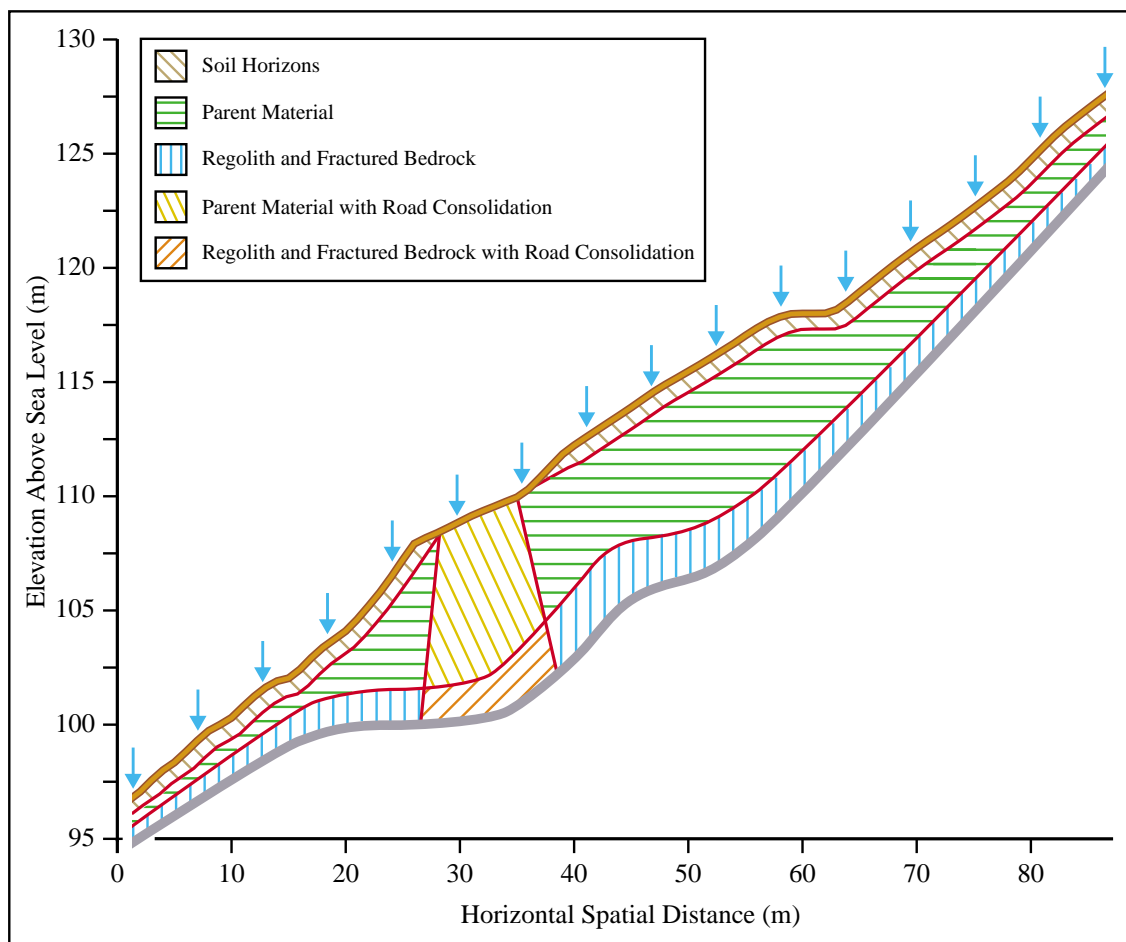


**Figure 18:** Scenario 3, permeability zones with road consolidation.

## **MODEL RESULTS**

Simulation results are presented for each of the groundwater scenarios.

### **Scenario 1: Sensitivity Analysis and Drainage Simulation**

The differences between the simulation results from scenario 1 were quantified using a root mean squared error (RMSE) criteria. The equation for the pressure RMSE is

$$\text{RMSE} = \sqrt{\frac{\sum_{i=1}^{\text{NN}} [(p_i^* - p_i)^2]}{\text{NN}}} \quad (3)$$

where  $p_i^*$  is the base case pressure head at a specific spatial node  $i$ ,  $p_i$  is the pressure head for a given run of the model, and NN is the total number of spatial nodes. The RMSE quantifies the difference in pressure head conditions between two simulation results for a given time period. Each of the two simulations share identical finite element meshes, however, system parameters and boundaries differ between the simulations.

The first simulation is run with a set of parameters known as the ‘base case.’ Base case parameter values for scenario 1 are listed in Table 2. The second simulation utilizes parameter values identical to the base case with the exception of a single parameter change. Incrementing a single parameter value over a range of magnitudes generates a number of simulation results. These simulation results are compared to the base case results using the RMSE.

A RMSE analysis is performed for the parameters: (1) intrinsic permeability, (2) porosity, (3) soil type, (4) temporal step size, and (5) the total number of elements within the system. A detailed description of the RMSE results is given in

Appendix C of this report. In Figures 19-22 and 24, the base case appears as the point for which RMSE = 0.

**Table 2:** Scenario 1 parameters for base case simulation.

PARAMETER	NOTATION	VALUE	UNITS
Fractional upstream weight	UP	0	Unitless
Pressure boundary-condition	GNUP	0.01	Unitless
Duration of time step	DELT, $\Delta t$	10	sec
Maximum allowed simulation time	TMAX	100000	sec
Fluid compressibility	COMPFL, $\beta$	2.718E-6	(m sec <sup>2</sup> ) / kg
Density of fluid	RHOW0, $\rho$	1000	kg / m <sup>3</sup>
Fluid Viscosity	VISCO0, $\mu$	0.001	kg / (m sec)
Solid matrix compressibility	COMPMA, $\alpha$	1.27E-6	(m sec <sup>2</sup> ) / kg
Density of solid grain	RHOS	1025	kg / m <sup>3</sup>
Component of gravity vector in the +X direction	GRAVX	0	m / sec <sup>2</sup>
Component of gravity vector in the +Z direction	GRAVY	-9.81	m / sec <sup>2</sup>
Intrinsic Permeability	PMAX/MIN, $k$	1.0E-11	m <sup>2</sup>
Volumetric Porosity	POR, $\epsilon$	0.1	Unitless
Number of elements in systems	NE	2696	Unitless
Sandy clay loam: Scaling Factor	a	0.58	m <sup>-1</sup>
Shape Parameter	n	1.59	Unitless
Water saturation at saturation	Ssat	0.54	Unitless
Residual saturation	Swres	0.09	Unitless

The sensitivity of the model to intrinsic permeability, a measure of the ease of fluid movement through saturated interconnected void spaces, is shown in Figure 19. The range in intrinsic permeabilities is  $k = 10^{-13} \text{ m}^2$  to  $k = 10^{-10} \text{ m}^2$ . Changes to intrinsic permeabilities in the range ( $10^{-13} \text{ m}^2 < k < 10^{-11} \text{ m}^2$ ) significantly impact the models solution while changes in the range ( $10^{-11} \text{ m}^2 < k < 10^{-10} \text{ m}^2$ ) have little to no impact.

The sensitivity of the model to porosity is shown in Figure 20. Recall, the porosity is the volume of voids in the soil matrix per total volume. The range in porosity is  $\epsilon = 1\%$  to  $\epsilon = 30\%$ . RMSE increases approximately linearly with departures of porosity from the base case value.

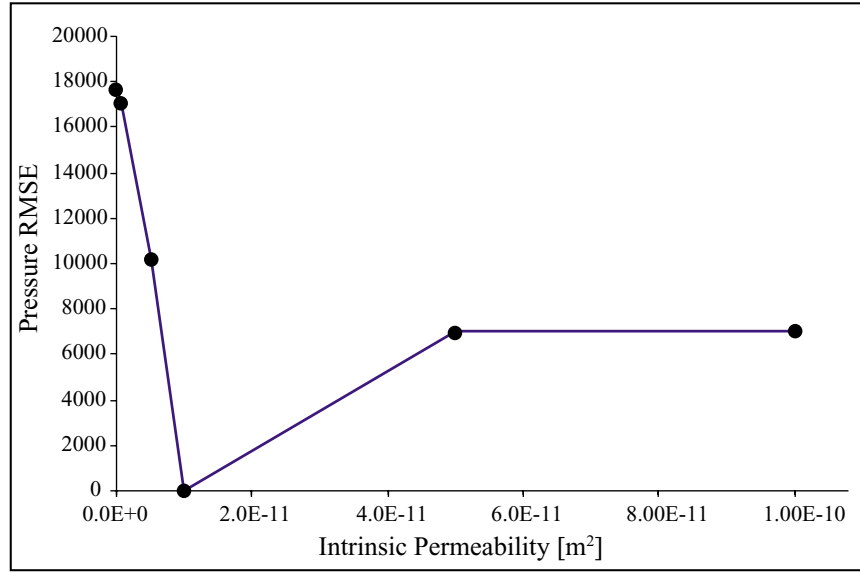


**Figure 19:** Scenario 1, pressure root mean squared error versus the intrinsic permeability.

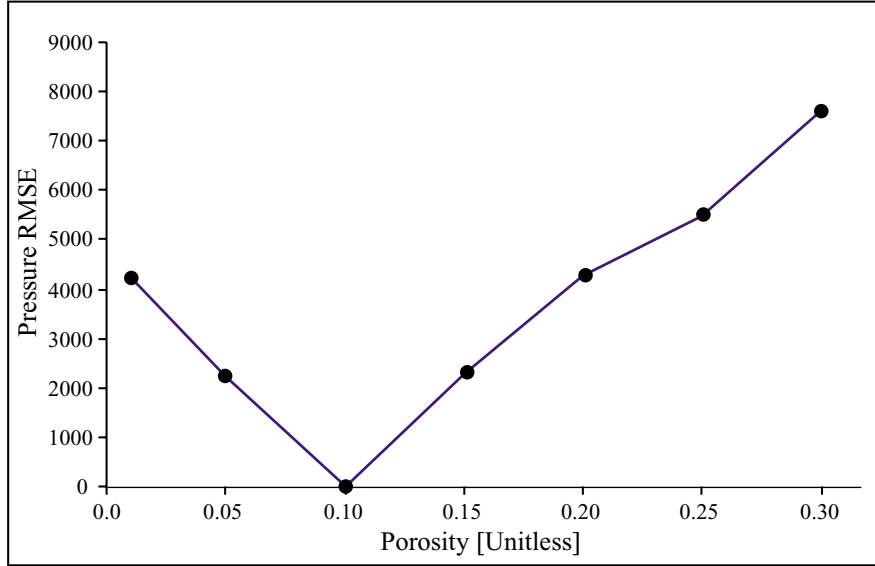


**Figure 20:** Scenario 1, pressure root mean squared error versus porosity.

Several parameters describing partially saturated conditions within the subsurface ( $a$ ,  $n$ ,  $S_{\text{sat}}$ ,  $S_{\text{wres}}$ ) are dependent on soil type. Field and laboratory experiments are typically used to identify the partially saturated parameters within a study site. Soil tests within the E-Road swale were not made. However, a soil survey con-

ducted for the watershed identified the soil type as ‘clay loam.’ Table 3 gives the range of different soil types utilized for the sensitivity analysis of partially saturated parameters. A soil type of ‘sandy clay loam’ is used in the base case simulation of scenario 1.

**Table 3:** Partially saturated parameters for seven soil types.

SOIL TYPES	a	n	S <sub>sat</sub>	S <sub>wres</sub>
Sandy loam	2.77	2.89	0.44	0.00
Silt Loam	10.92	1.18	0.50	0.00
Loam	17.81	1.16	0.50	0.00
Sandy clay loam	0.58	1.59	0.54	0.09
Silty clay loam	1.36	1.24	0.56	0.00
Clay loam	1.25	2.38	0.56	0.07
Beit Netofa Clay	0.152	1.17	0.446	0.00

RMSE values calculated for each of the seven soil types are shown in Figure 21. Similar simulation results are observed for silt loam, loam, and sandy clay loam.

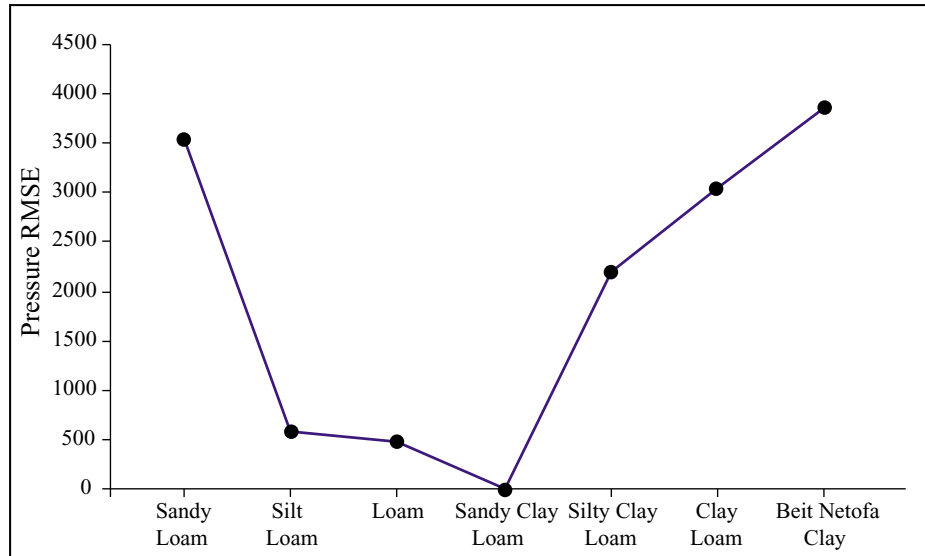


**Figure 21:** Scenario 1, pressure root mean squared error versus soil type.

Figure 22 shows RMSE values calculated for a range of temporal step sizes,  $\Delta t$ . Theory suggests that a decrease in  $\Delta t$  increases the numerical stability of the model.

The tradeoff associated with a smaller step size is an increase in computational time (Figure 23). For temporal step sizes less than 40 sec, the model is very sensitive to small changes in  $\Delta t$ . Decreasing the temporal step size results in a reduction in the moisture levels within the systems partially saturated conditions. For larger  $\Delta t$  values an upper limit is established at 200 sec. Simulations made with  $\Delta t > 200$  sec produced irregular drainage patterns within the swale. The irregular drainage patterns, evident in the model's inappropriate storage of water within the upper portion of the swale, is attributed to a breakdown in the numerics.

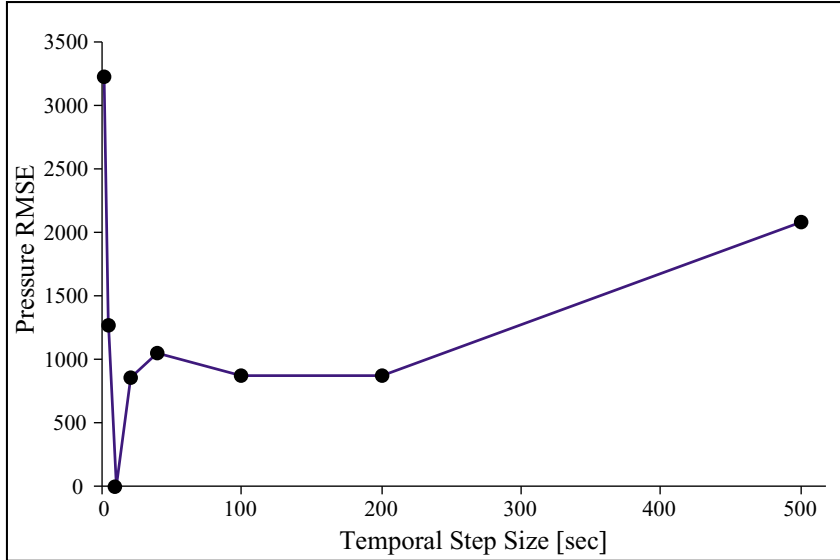


**Figure 22:** Scenario 1, pressure root mean squared error versus temporal step size.

The sensitivity of the model to spatial discretization is established in Figure 24. Figure 24 shows the pressure RMSE as a function of the total number of elements within the system. Previous modeling investigations of a partially saturated system indicate the susceptibility of the model to numerical breakdown given an insufficient number of elements (Fisher, 1999). The numerical instability was characterized by a

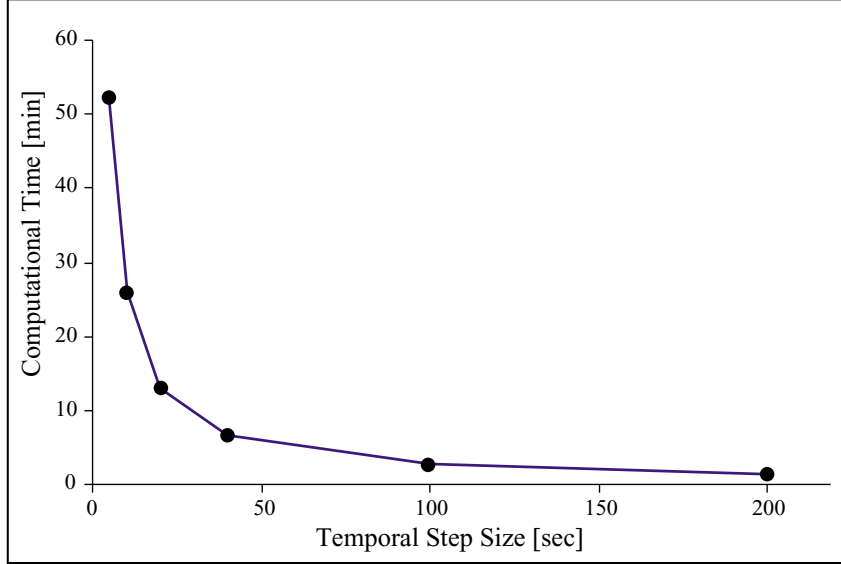


**Figure 23:** Scenario 1, computational time versus temporal step size.

nonuniform capillary fringe along the phreatic surface. For scenario 1, the numerical breakdown occurred for systems containing less than 1404 elements.

Greater numerical stability is achieved with an increase in the number of finite elements within the system. In addition, a finer mesh density requires additional computational time. Figure 25 gives the computational time as a function of the total number of elements.

A maximum pressure RMSE is identified for each of the parameters previously examined within the RMSE analysis. The magnitude of the maximum RMSE is sensitive to the choice of base case and the range over which the parameter was tested. A comparison of the maximum RMSE values is shown in Figure 26. Sensitivity of the model is greatest for changes in intrinsic permeability. A moderate sensitivity is observed for both the porosity and total number of elements. The lowest sensitivity is associated with the soil type and temporal step size.

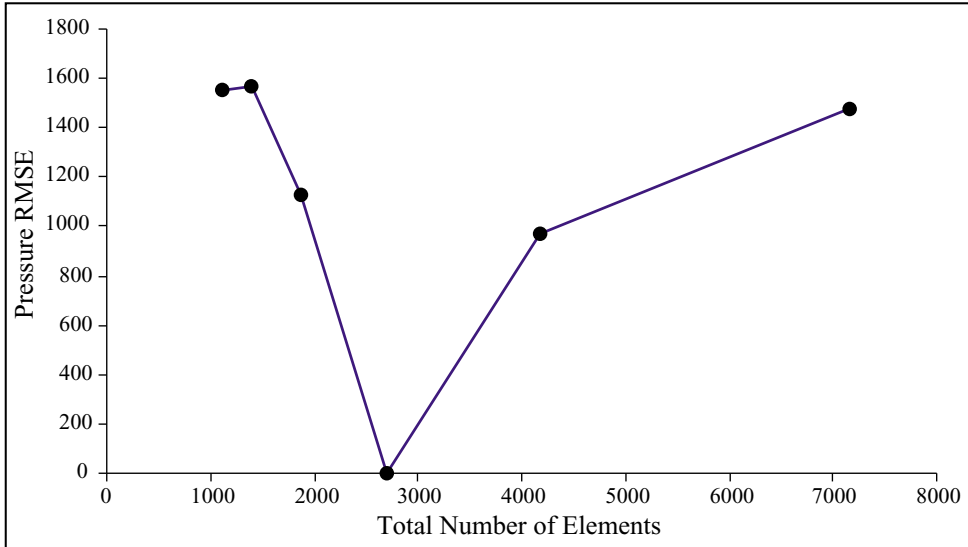


**Figure 24:** Scenario 1, pressure root mean squared error versus the number of elements.

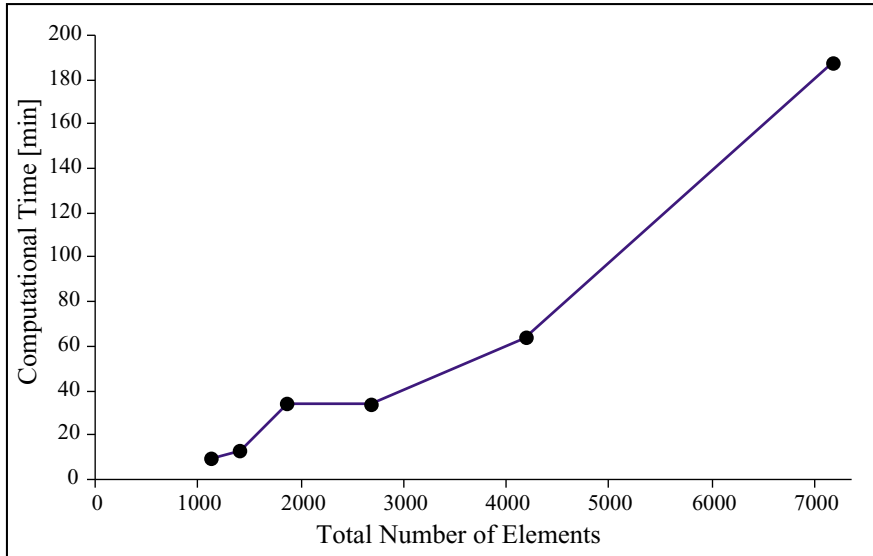


**Figure 25:** Scenario 1, computational time versus the total number of elements.

Pressure conditions are given after 2.8, 13.9, and 27.8 hr of simulation time (Figure 27), to demonstrate the model's ability to drain over time. As expected, the phreatic surface (0 pa pressure contour) progressively lowers in elevation for each time period. The horizontal phreatic surface, observed after 13.9 hr of simulation

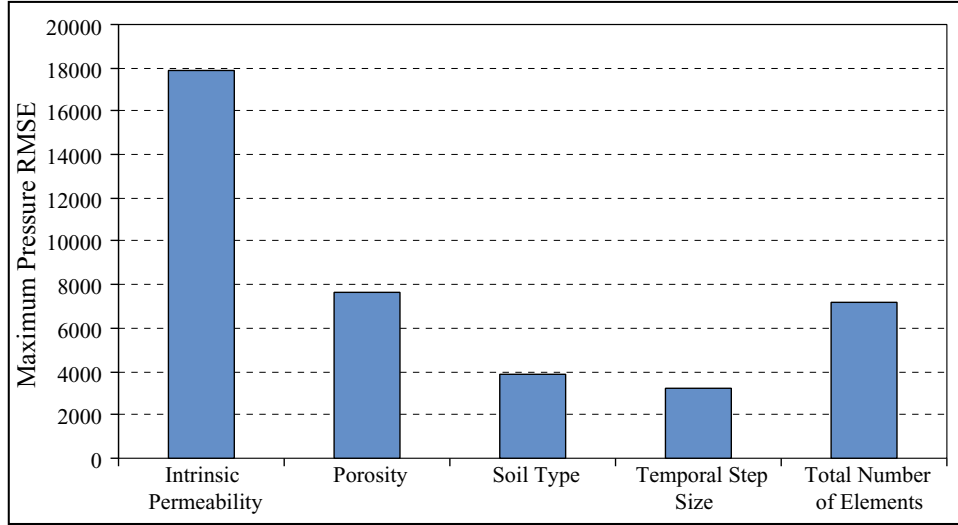


**Figure 26:** Scenario 1, parameter sensitivity.

time, illustrates the effect of an impermeable ground surface boundary pressure set constant at 0 pa. The ground surface boundary, sharing a common pressure with the phreatic surface, has the undesirable effect of flooding the lower portion of the swale.

Located within the upper portion of the swale are the partially saturated pressure contours ( $p < 0$  pa). The irregular contours, describing the partially saturated conditions, are believed to be a product of numeric instability. The equations for partially saturated flow are extremely nonlinear and susceptible to breakdown in systems of low saturation.

Velocity vectors for each element in scenario 1 are given after 13.9 hr of base case simulation (Figure 28). For saturated conditions, velocity vectors directionally align with the lower hydrostatic boundary and are indistinguishable within the partially saturated conditions. The velocity vectors do not take shape until  $p > 0$  pa. A constriction of flow within the base of the swale, where bedrock and ground

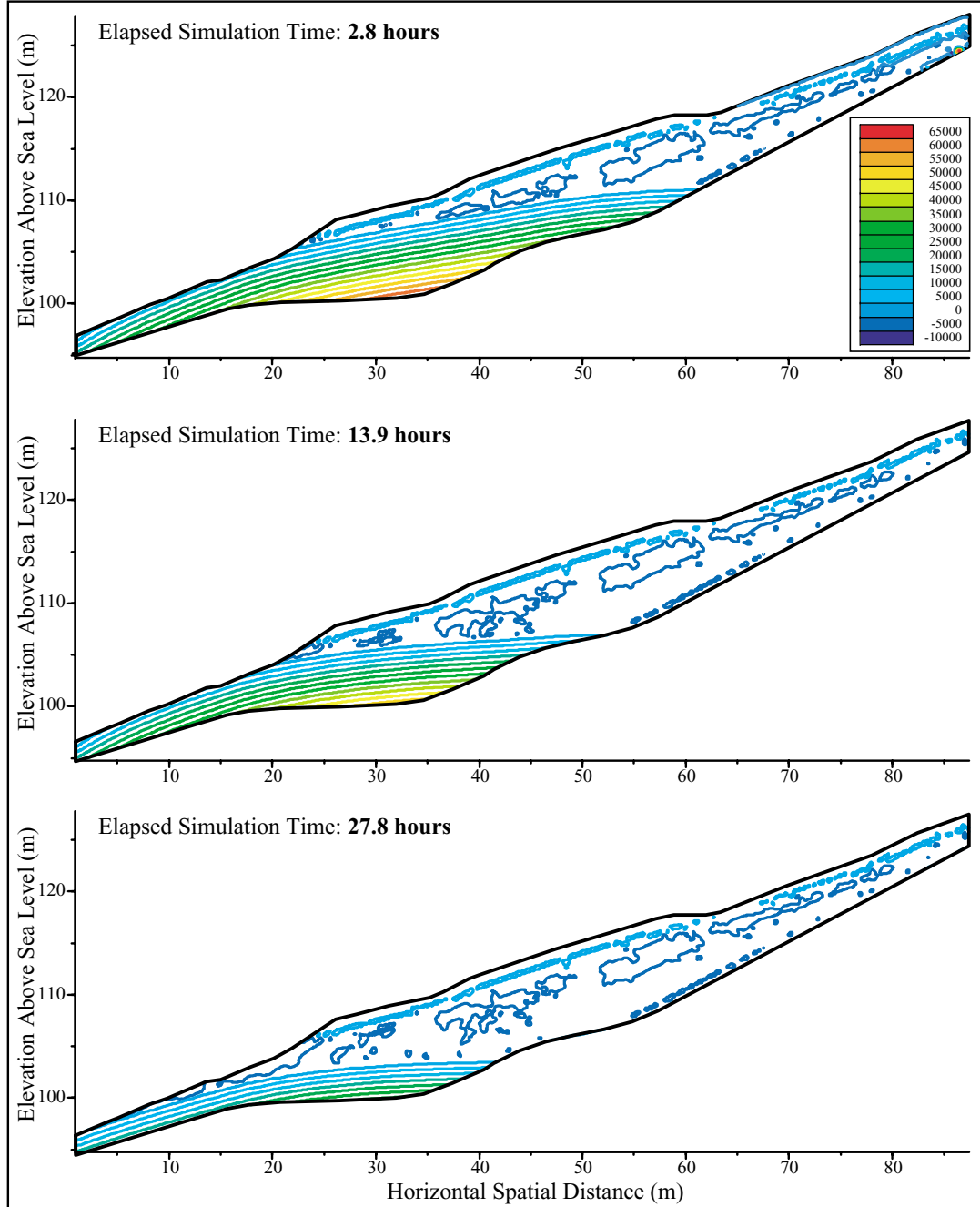


**Figure 27:** Scenario 1 pressure contours (pa), drainage of system over a time period of 2.8, 13.9, and 27.8 hours.

surface boundaries merge, produces increased velocity magnitudes. Velocity vectors exit the system through the lower hydrostatic boundary. The total mass flux across

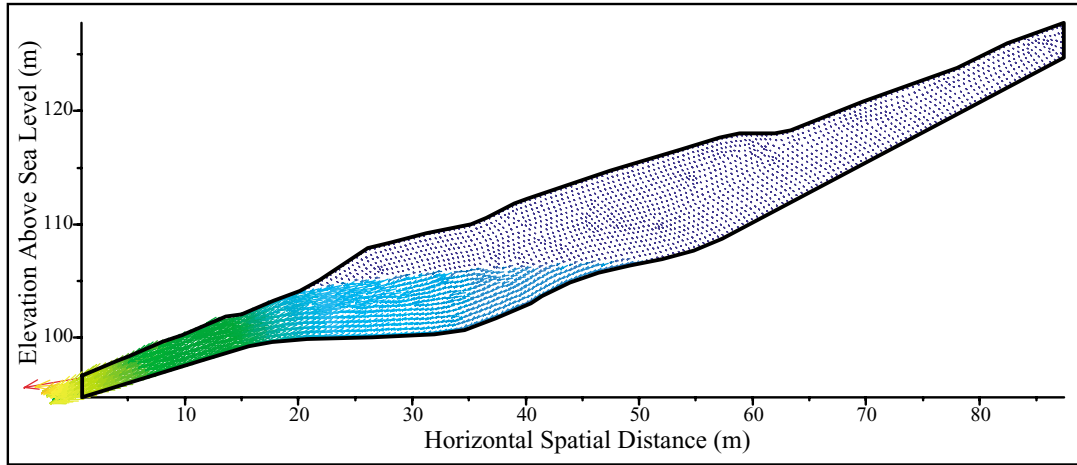


**Figure 28:** Scenario 1, velocity vectors after 13.9 hours of simulation.

the lower hydrostatic boundary is 0.062 kg/m.

### Scenario 2: Pre-Road Building

Scenario 2 parameters are summarized in Table 4. An increase in  $\Delta t$  was required to complete a simulation run in a reasonable amount of time. At  $\Delta t = 200$  sec, the 61-day simulation took approximately 14 hours to complete. Intrinsic permeabilities within the system are given for each material type. A high intrinsic permeability is specified in the soil horizons, a moderate intrinsic permeability in the parent material, and a low intrinsic permeability within the regolith and fractured bedrock. The time dependent rainfall flux, specified across the ground surface boundary, is a function of historical rainfall records (November 10<sup>th</sup> 1996 to January 10<sup>th</sup> 1997).

Figure 29 depicts the pressure contours after 61 days of simulation. The shape of the phreatic surface reveals the impact of intrinsic permeability layering within the system. The placement of a higher intrinsic permeability zone over a lower

**Table 4:** Scenario 2 parameters (see Table 2 for undefined parameters).

PARAMETER	NOTATION	VALUE	UNITS
Duration of time step	DELT, $\Delta t$	200	sec
Maximum allowed simulation time	TMAX	5270400	sec
Permeability: Soil Horizons	k	1.0E-11	m <sup>2</sup>
Parent Material		6.0E-13	m <sup>2</sup>
Regolith and Fractured Bedrock		7.0E-14	m <sup>2</sup>
Number of elements in systems	NE	3949	Unitless
Clay loam: Scaling Factor	a	1.25	m <sup>-1</sup>
Shape Parameter	n	2.38	Unitless
Water saturation at saturation	Ssat	0.56	Unitless
Residual saturation	Swres	0.446	Unitless

intrinsic permeability zone produces a lag in the groundwater movement within the regolith and fractured bedrock. The lag is most evident within the upper portion of the swale where drainage rates are highest. The difference in drainage rates between the two material types is shown in Figure 30. Velocities within the parent material are much greater than velocities within the regolith and fractured bedrock.

Flow within the soil horizons is dominated by gravity, with capillary forces masked by the material's high intrinsic permeability. The only observable horizontal flow within the soil horizons is found within the base of the swale. A constriction of flow within the base forces the water table upward into the soil horizons. Unable to enter back into the parent material, water is quickly transported out of the system through the soil horizons. Velocity vectors, pointing outward across the ground surface boundary, are responsible for ground seepage.

Simulations were made with reduced historic rainfall to test the sensitivity of the model to changes in rainfall magnitude. Unexpectedly, there was no change in the model solution for a 99% reduction in historical rainfall. The magnitude of the mass flux across the ground surface boundary is negligible within the modeled

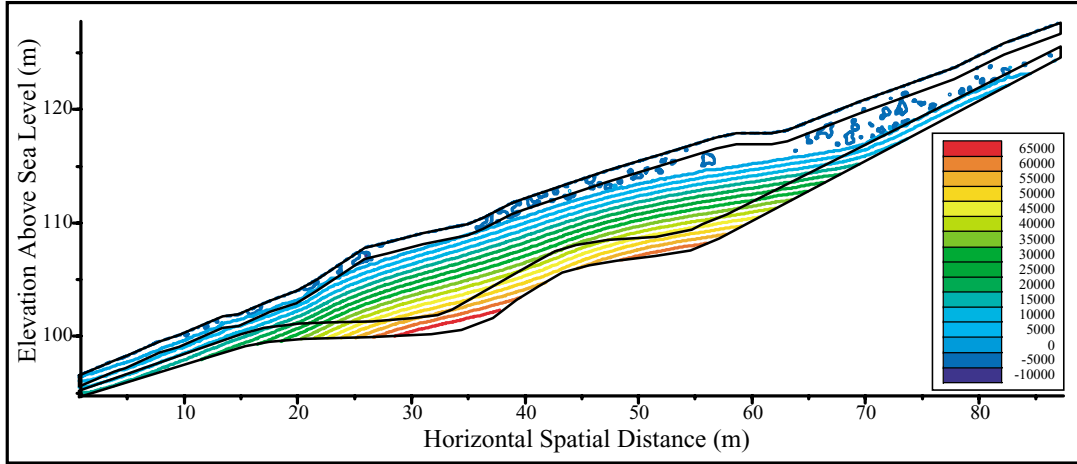


**Figure 29:** Scenario 2, pressure contours (pa) after 61 days of simulation.

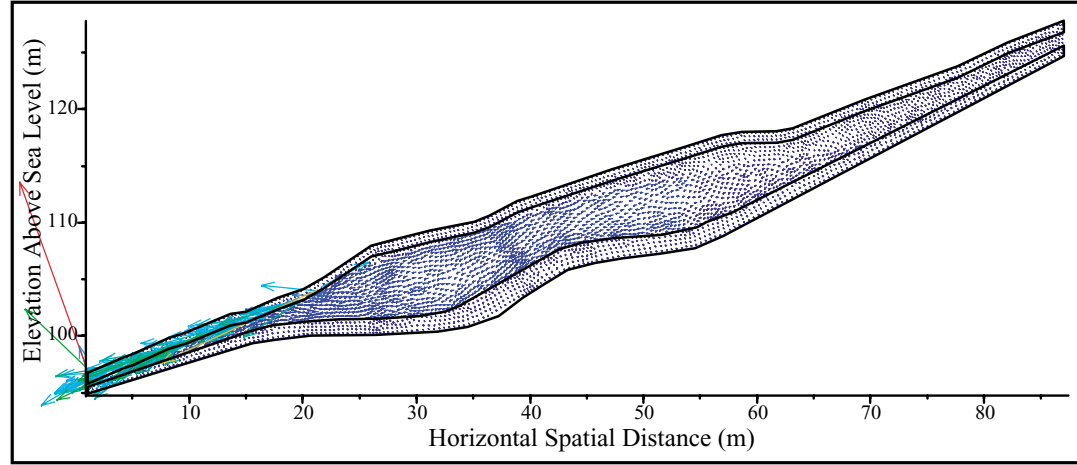


**Figure 30:** Scenario 2, velocity vectors after 61 days of simulation.

system. The pressure response to precipitation events is instead governed by the model's pressure switch within the ground surface boundary.

### Scenario 3: Post-Road Building and Historical Comparisons

Scenario 3 parameters are identical to scenario 2 parameters with the addition of two low intrinsic permeability zones beneath the road surface. The intrinsic permeabilities of the two additional zones are  $k = 3 \cdot 10^{-12} \text{ m}^2$  within the consolidated

parent material and  $k = 6 \cdot 10^{-14} \text{ m}^2$  within the consolidated regolith and fractured bedrock. Pressure contours and velocity vectors after a 61 day simulation period are shown in Figures 31 and 32, respectively. The effect of road consolidation is an increase in pore pressure beneath the road bed. Groundwater, impeded by the low intrinsic permeability zone, mounds behind the consolidated material, reaching an upper limit at the ground surface boundary.

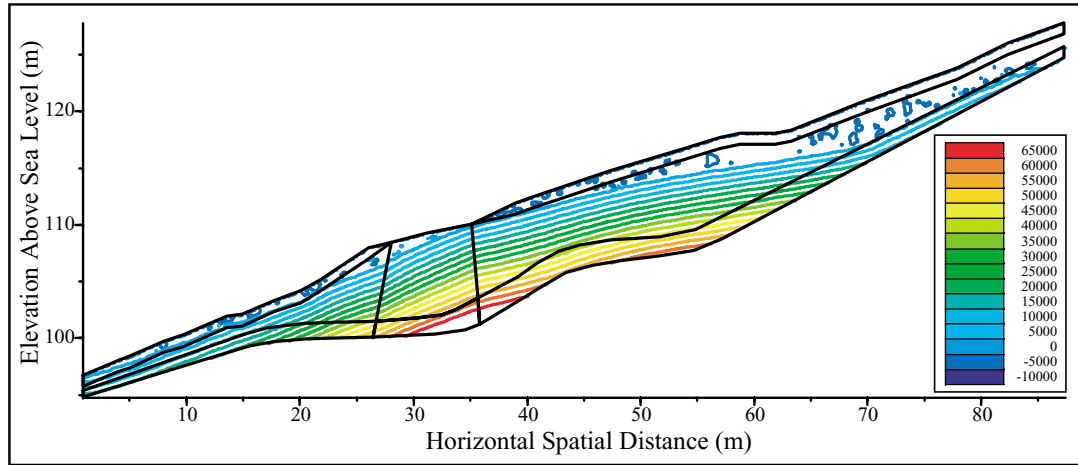


**Figure 31:** Scenario 3, pressure contours (pa) after 61 days of simulation.

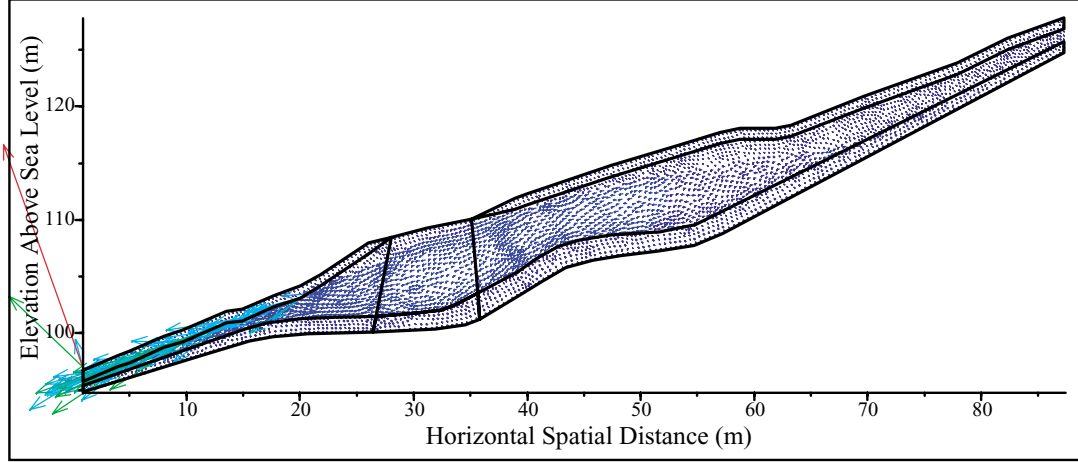


**Figure 32:** Scenario 3, velocity vectors after 61 days of simulation.

For each of the swale's piezometers, a comparison is made between the water year 1997 historical and simulated hydraulic heads (Figures 33-38). The conversion from capillary pressure,  $p$ , to hydraulic head,  $h$ , is

$$h_{\text{piez}} = \frac{p_{\text{piez}}}{\gamma} + z_{\text{elev}} \quad (4)$$

where  $h_{\text{piez}}$  is the piezometric head,  $p_{\text{piez}}$  is the pore water pressure within the base of the piezometer,  $\gamma$  is the specific weight of water, and  $z_{\text{elev}}$  is the elevation of the piezometer's base. For the month of November 1996, the simulated pressure response of the upper piezometers is strongly affected by the model's initial pressure conditions. By December 1996 the influence of the initial conditions is less apparent.

As seen in Figures 37 and 38, historical drainage rates are much greater than simulated drainage rates. The difference in drainage rates is attributed to the model's inability to simulate pipeflow within the system. To compensate for pipeflow, intrinsic permeabilities were increased throughout the swale. The system's response to higher intrinsic permeabilities is an increase in drainage within the upper piezometers and a decrease in drainage within the lower piezometers. The decrease in drainage emphasizes the control of the hydrostatic boundary on drainage rates within the lower portion of the swale. Hydrostatic pressures, which are assumed constant over time, place a limit on drainage across the swale's lower vertical boundary. Groundwater, unable to exit the system at drainage rates associated with increased intrinsic permeability, builds behind the hydrostatic boundary, flooding the lower portion of the swale. The flooding is compounded by the excessive drainage rates within the upper portion of the swale.

The model's overprediction of hydraulic heads within piezometer R4P2 (Figure 36) is not easily understood. Any number of hydrologic flow mechanisms, either misrepresented or neglected within the system, may attribute to the approximately 4 m difference between historical and simulated water pressures. Possible problem areas include: (1) neglecting convergent flow within the 2-d system, (2) the incorrect placement of the bedrock boundary, (3) the inability of the model to simulate pipeflow, and (4) an oversimplification of ground consolidation with depth. These issues should be addressed in future groundwater studies.

The frequency response for a piezometer is characterized by the number of cycles or oscillations of pressure per unit time. Where waves of multiple frequencies are superimposed the characterization can be quite complex. R5P2 and R6P2 (Figure 11) clearly have a high frequency pattern superimposed on a low frequency annual cycle. For each of the piezometers, historical and simulated responses appear to operate at a common frequency. A casual comparison of the frequency response for each of the piezometers indicates three dominant frequencies within the system: piezometers R1P2 and R2P2 share a high frequency response, piezometers R3P2, R5P2, and R6P2 a moderate frequency response, and piezometer R4P2 a low frequency response. The model appears to reproduce some of the different frequency responses within the E-Road groundwater system. No attempt was made to rigorously analyze the frequency spectra nor to validate the dual frequency responses seen in R5P2 and R6P2 after logging.

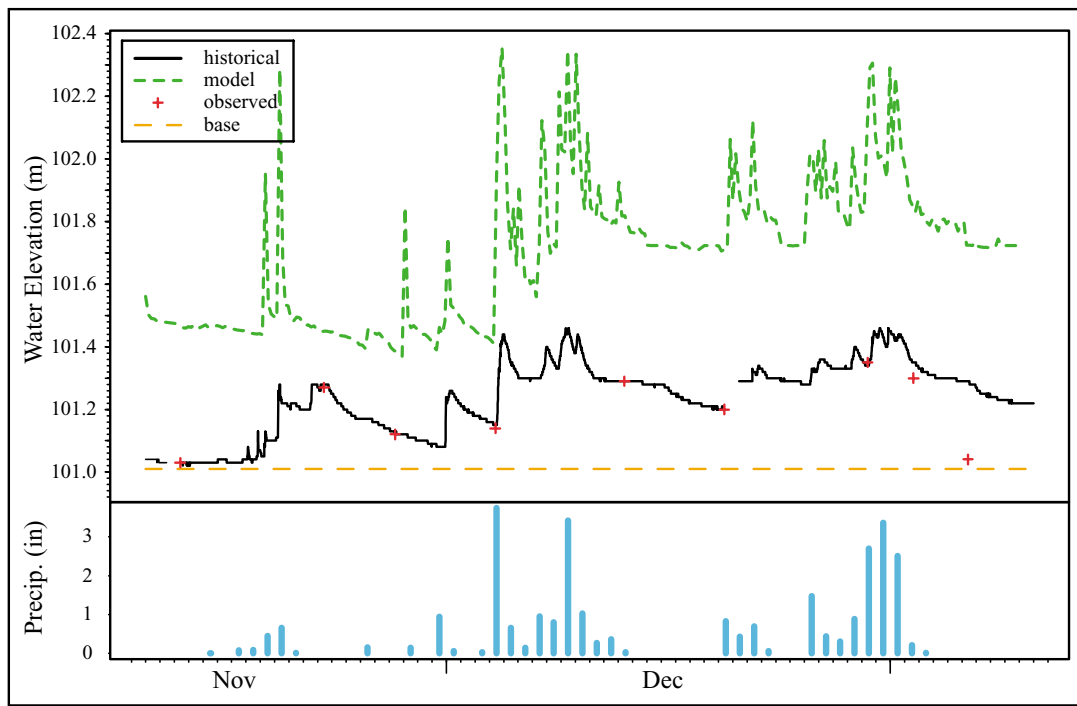


**Figure 33:** Historical and simulated (scenario 3) hydraulic head values for piezometer R1P2.

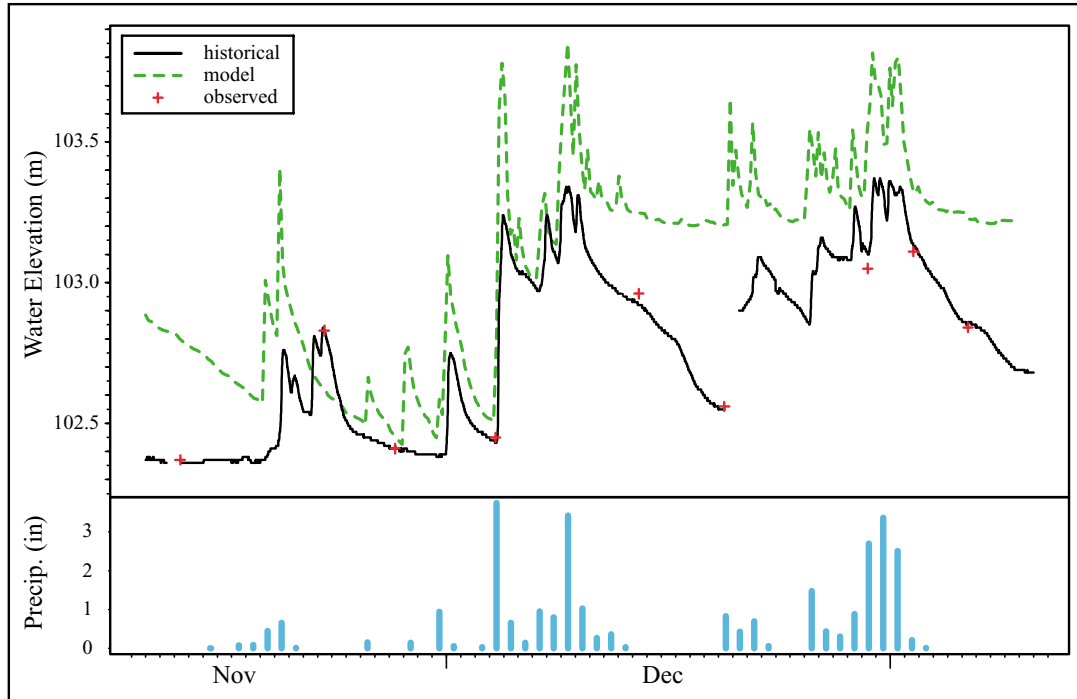


**Figure 34:** Historical and simulated (scenario 3) hydraulic head values for piezometer R2P2.

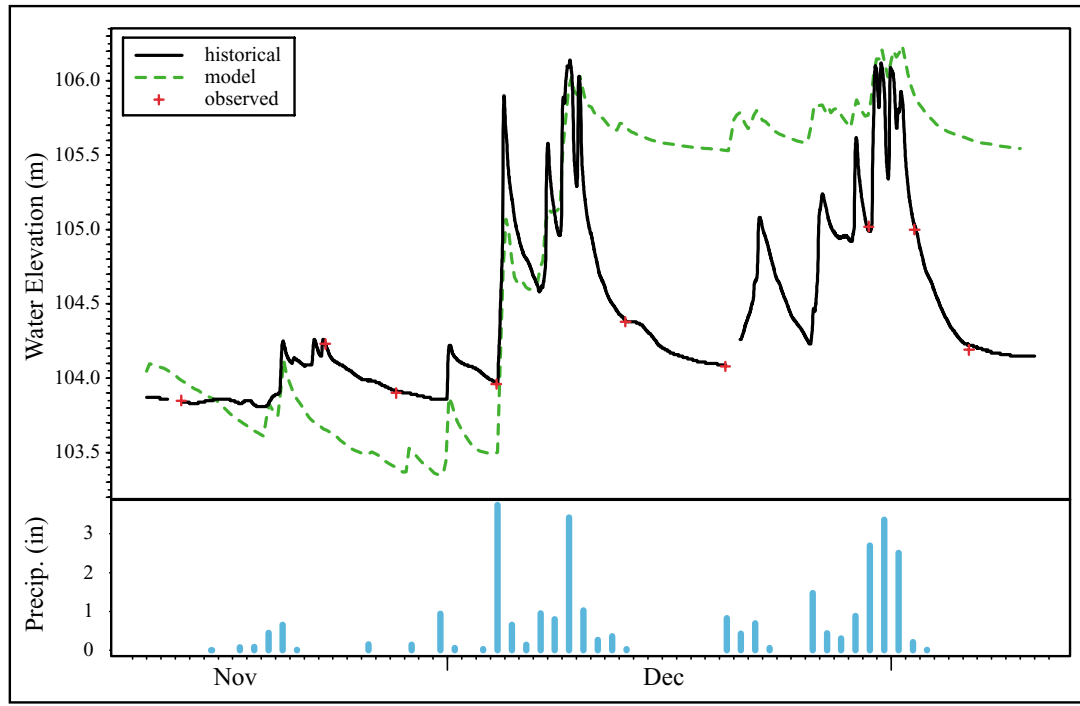


**Figure 35:** Historical and simulated (scenario 3) hydraulic head values for piezometer R3P2.

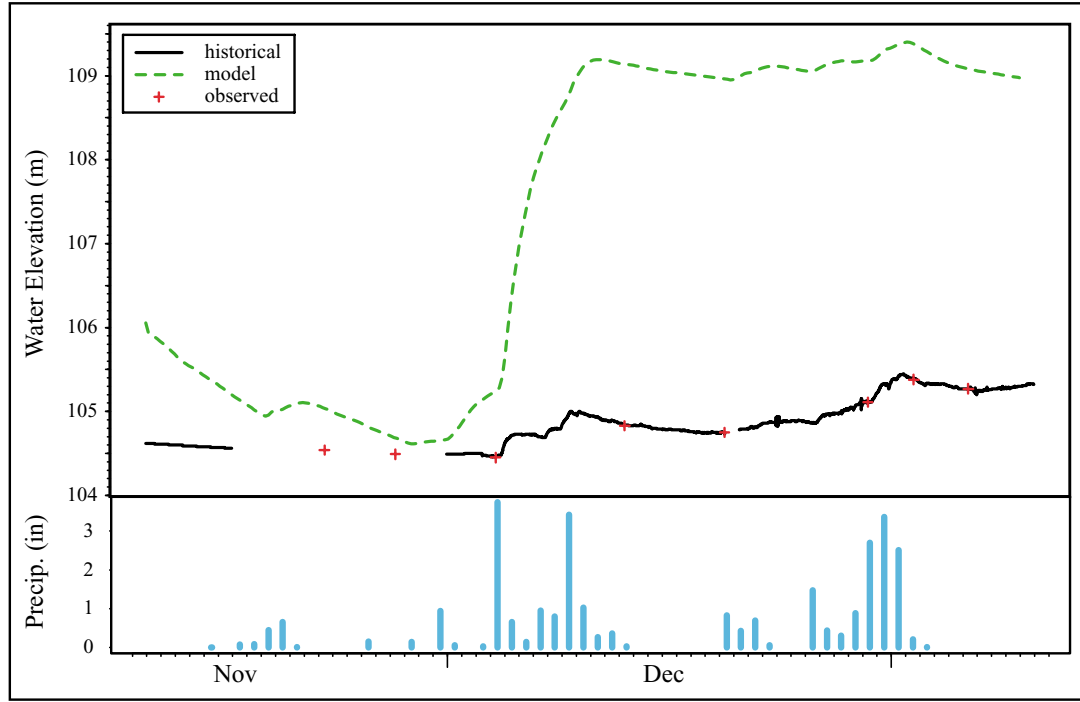


**Figure 36:** Historical and simulated (scenario 3) hydraulic head values for piezometer R4P2.

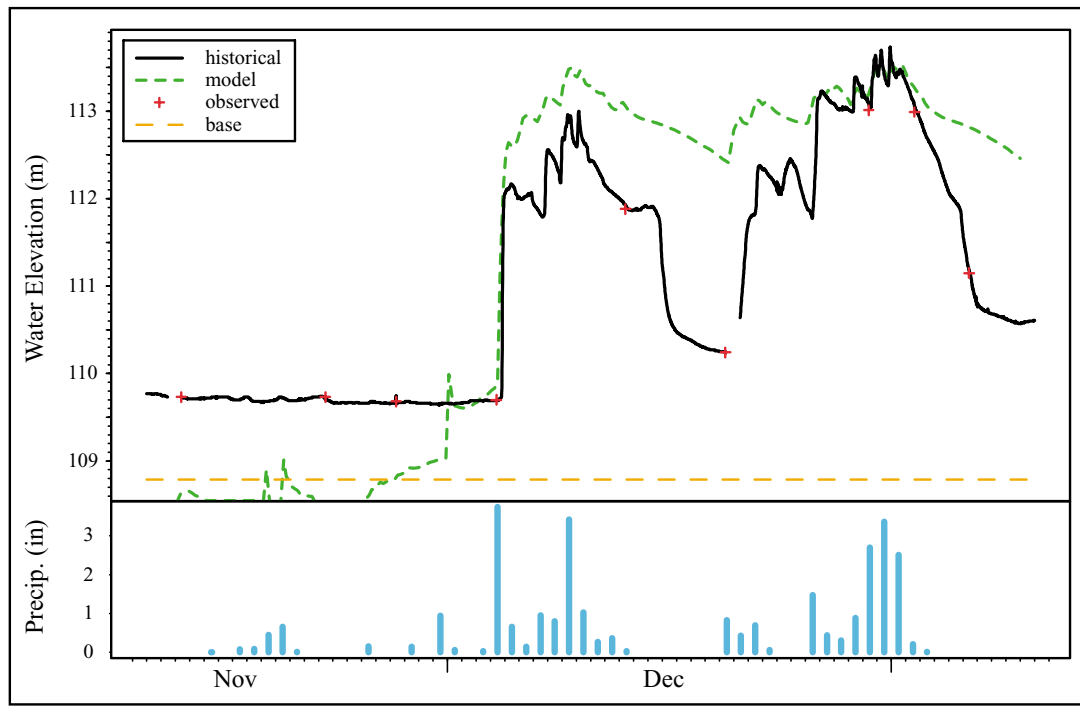


**Figure 37:** Historical and simulated (scenario 3) hydraulic head values for piezometer R5P2.

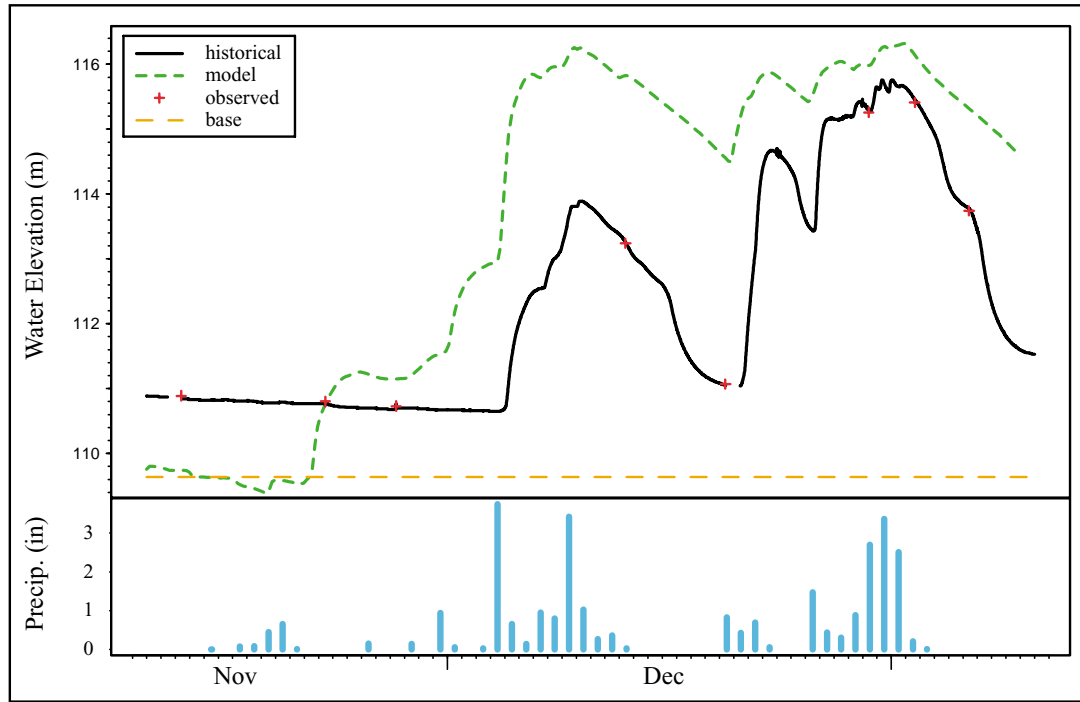


**Figure 38:** Historical and simulated (scenario 3) hydraulic head values for piezometer R6P2.

A comparison of the simulations made with (scenario 3) and without (scenario 2) the road consolidation is shown in Figure 39. For each of the scenarios, R4P2 piezometric heads are given over time (December 7<sup>th</sup> 1996 to January 11<sup>th</sup> 1997). As can be seen from Figure 39, drainage rates without the road (scenario 2) are greater than drainage rates with the road (scenario 3). Furthermore, peak hydraulic head responses to precipitation are greater for the scenario 3 system.

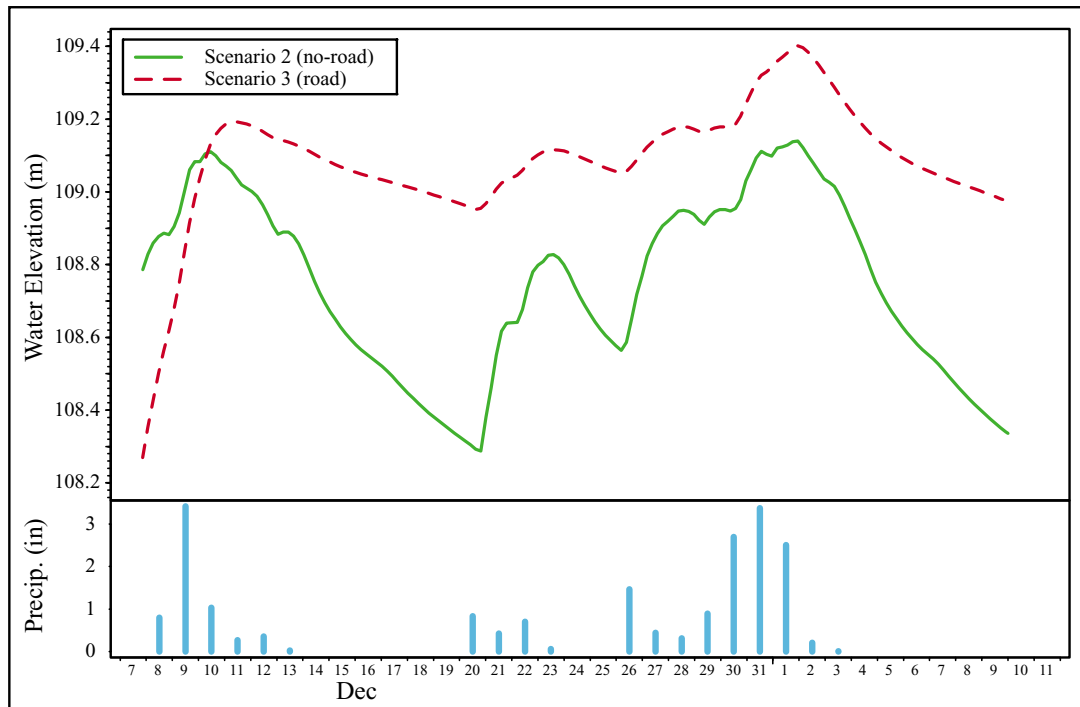


Figure 39: A comparison between scenario 2 and 3 for piezometer R4P2.

Comparing the effects of road consolidation on the system's peak pore pressure response illustrates the model's usefulness as an engineering design tool. As previously stated, the pressure response beneath and above the road may be used as an indicator for landslide susceptibility within the swale. An increased likelihood of slope failure is attributed to higher pore water pressures within the subsurface envi-

ronment. The model's ability to identify the hydrologic controls which govern pore pressures within the swale is useful in selecting road designs and road restoration techniques which minimize the peak pressure responses beneath the road surface.

## **CONCLUSIONS**

The results of this thesis have demonstrated:

1. Road consolidation is associated with increased pore water pressures beneath the road bed.
2. The inability of the model to account for pipeflow produces simulated drainage rates much slower than historical drainage rates.
3. Analysis of the simplified model Scenario 1 indicated model sensitivity was greatest for changes in intrinsic permeability.
4. Mass flux across the ground surface boundary is negligible within the modeled system.
5. The model appears to reproduce the uniquely different frequency responses within the E-Road groundwater system.
6. A decrease in the temporal step size,  $\Delta t$ , increases both the numerical stability of the model and the computational time required for a simulation. A  $\Delta t = 200$  sec is recommended to ensure numerical stability while holding computational time within practical limits.
7. A finer discretization within the finite element mesh produces an increase in numerical stability and an increase in the computational time required for a simulation. A 4000 element mesh is recommended to maintain numerical stability within the partially saturated conditions while holding computational time within practical limits.

## REFERENCES

- Albright, J. S., *Storm Runoff Comparisons of Subsurface Pipe and Stream Channel Discharge in a Small, Forested Watershed in Northern California*, Master of Science Thesis, Humboldt State University, Arcata, CA, 118 p., 1992.
- ArgusONE, <http://www.argusint.com/index.html>, 2000.
- Bear, J., *Dynamics of Fluids in Porous Media*, Dover Publications, Inc., New York, 361-437, 1972.
- Bear, J., *Hydraulics of Groundwater*, McGraw-Hill, New York, 567 p., 1979.
- Beven, K. J., *The Grendon Underwood Field Drainage Experiment*, Institute of Hydrology, Wallingford, U. K., Rep. No. 65, 1980.
- Beven, K. J., Changing ideas in hydrology - The case of physically-based models, *Journal of Hydrology*, 105, 157-172, 1989.
- Beven, K. J., A. Calver, and E. M. Morris, *The Institute of Hydrology Distributed Model*, Institute of Hydrology, Wallingford, U. K., Rep. No. 98, 1987.
- Blain, C. A., *Development of a Physically Based Numerical Soil Moisture Flow Model which has Applications to the Soil Matrix and Macropore Domains*, Master of Science Thesis, Princeton University, 1989.
- Boussinesq, J., Recherches theorétiques sur l'écoulement des nappes d'eau infiltrées dans le sol et sur le débit des sources, *Jour. Math. Pres Appl.*, 5, 5-78, 1904.
- Brandes, D., C. J. Duffy, and J. P. Cusumano, Stability and damping in a dynamical model of hillslope hydrology, *Water Resources Research*, 34(12), 3303-3313, 1998.
- Brown, D. L., *An Analysis of Transient Flow in Upland Watersheds: Interactions between Structure and Process*, Ph.D. dissertation, University of California, Berkeley, 225 p., 1995.
- Buchanan, P., K. W. Savigny, and J. De Vries, A method for modeling water tables at debris avalanche headscarsps, *Journal of Hydrology*, 113, 61-88, 1990.
- Calver, A., Calibration, sensitivity and validation of a physically-based rainfall-runoff model, *Journal of Hydrology*, 103, 103-115, 1988.

- Calver, A., and W. L. Wood, On the discretization and cost-effectiveness of a finite element solution for hillslope subsurface flow, *Journal of Hydrology*, 110, 165-179, 1989.
- Darcy, H., *Les Fontaines Publiques de la Ville de Dijon*, Dalmont, Paris, 1856.
- Dietrich, W. E., C. J. Wilson, and S. L. Reneau, Hollows, colluvium, and landslides in soil-mantled landscapes, *Hillslope Processes*, A. D. Abrahams, ed., Allen and Unwin Ltd., 361-388, 1986.
- Fisher, J. C., *Numerical sensitivity of a finite element solution for unconfined groundwater flow*, final report for Advanced Numerical Methods, Humboldt State University, Arcata, CA, 26 p., 1999.
- Freeze, R. A., Three-dimensional, transient, saturated-unsaturated flow in a ground-water basin, *Water Resources Research*, 7(2), 347-366, 1971.
- Freeze, R. A., Role of subsurface flow in generating surface runoff 1. Base flow contributions to channel flow, *Water Resources Research*, 8, 609-623, 1972a.
- Freeze, R. A., Role of subsurface flow in generating surface runoff 2. Upstream source areas, *Water Resources Research*, 8, 1272-1283, 1972b.
- Freeze, R. A., Streamflow Generation, *Reviews of Geophysics and Space Physics*, 12, 627-647, 1974.
- Hanberg, W. C., and A. O. Gokce, *Rapid water level fluctuations in a thin colluvium landslide west of Cincinnati, Ohio*, U. S. Geol. Surv. Bull. 2059-C, 16 p., 1992.
- Harr, R. D., Water flux in soil and subsoil on a steep forested slope, *Journal Hydrology*, 33, 37-58, 1977.
- Hewlett, J. D., and W. L. Nutter, *The varying source area of streamflow from upland basins*, paper presented at the Symposium on Interdisciplinary Aspects of Watershed Management, Montana State University, Bozeman, 1970.
- Huff, T. L., D. W. Smith, and W. R. Powell, Tables for the soil-vegetation map, Jackson State Forest, Mendocino County, Soil-Vegetation Survey, California Department of Forestry, The Resources Agency, Sacramento, CA, 1985.
- Huyakorn, P. S., J. Kool, and H. White, *VAM2D: A variably saturated analysis model with hysteresis and anisotropy in two-dimensions*, Nucl. Regul. Comm., Rockville, Md., Rep. NUREG/CR-5352, GGL/89-01, 1989.

- Jackson, C. R., A model of transient, topographically driven, saturated subsurface flow, *Water Resources Research*, 28(5), 1417-1427, 1992a.
- Jackson, C. R., Hillslope infiltration and lateral downslope unsaturated flow, *Water Resources Research*, 28(9), 2533-2539, 1992b.
- Keppeler, E. T., R. R. Ziemer, and P. H. Cafferata. *Changes in soil moisture and pore pressure after harvesting a forested hillslope in northern California*, In: Marston, Richard A., and Victor R. Hasfurther (eds). Proceedings, Annual Summer Symposium of the American Water Resources Association: Effects of Human-Induced Changes on Hydrologic Systems, Jackson Hole, Wyoming. American Water Resources Association, Bethesda, Maryland, June 26-29, 205-214, 1994.
- Keppeler, E. T., and D. L. Brown, *Subsurface drainage processes and management impacts*. In: Ziemer, Robert R., technical coordinator. Proceedings of the conference on coastal watersheds: the Caspar Creek story, 1998 May 6; Ukiah, CA. General Tech. Rep. PSW GTR-168. Albany, CA: Pacific Southwest Research Station, Forest Service, U.S. Department of Agriculture, 25-34, 1998.
- Killbourne, R. T., Geology and slope stability of the Fort Bragg area, *California Geology*, 39(3), 58-68, 1986.
- McCord, J. T., D. B. Stephens, and J. L. Wilson, Hysteresis and state-dependent anisotropy in modeling unsaturated hillslope hydrologic processes, *Water Resources Research*, 27(7), 1501-1518, 1991.
- Mosely, M. P., Streamflow generation in a forested watershed, New Zealand, *Water Resources Research*, 15(4), 795-806, 1979.
- Mualem, Y., A new model for predicting the hydraulic conductivity of unsaturated porous media, *Water Resources Research*, 12(3), 513-522, 1976.
- Narasimhan, T. N., P. A. Witherspoon, and A. L. Edwards, Numerical model for saturated-unsaturated flow in deformable porous media: 2. The algorithm, *Water Resources Research*, 14(2), 255-261, 1978.
- Reddi, L. N., I. M. Lee, and T. H. Wu, A comparison of models predicting groundwater levels of hillside slopes, *Water Resources Bulletin*, 26(4), 657-667, 1990.
- Shao, M., and R. Horton. Integral method for estimating soil hydraulic properties, *Soil Sci. Soc. Am. J.*, 62, 585-592, 1998.

- Singh, R. N., S. N. Rai, and D. V. Ramana, Water table fluctuation in a sloping aquifer with transient recharge, *Journal of Hydrology*, 126, 315-326, 1991.
- Sloan, P. G., and I. D. Morre, Modeling subsurface stormflow on steeply sloping forested watersheds, *Water Resources Research*, 20(12), 1815-1822, 1984.
- Swanson, D. N., *Soilwater piezometry in a southeast Alaska landslide area*, Forest Service, U. S. Department of Agriculture, Portland, Oreg., Res. Note PNW-68, 17 p., 1967.
- USGS, <http://water.usgs.gov/software/sutra-gui.html>, 2000.
- van Genuchten, M. Th. A closed-form equation for predicting the hydraulic conductivity of unsaturated soils, *Soil Sci. Soc. Am. J.*, 44, 892-898, 1980.
- Voss, C. I., *A finite-element simulation model for saturated-unsaturated, fluid density dependent ground-water flow with energy transport or chemically-reactive single species solute transport*, U. S. Geological Survey Water-Resources Investigations Report 84-4369, 409 p., 1984.
- Weyman, D. R., Throughflow on hillslopes and its relation to the stream hydrograph, *Bull. Int. Assoc. Sci. Hydrol.*, 15(2), 25-33, 1970.
- Whipkey, R. Z., Subsurface stormflow on forested slopes, *Bull. Int. Assoc. Sci. Hydrol.*, 10(2), 74-85, 1965.
- Willis, R., and W. W-G Yeh, *Groundwater Systems Planning and Management*, Prentice-Hall, Inc., Englewood Cliffs, New Jersey, 32-35, 1987.
- Wilson, C. J., *Runoff and Pore Pressure Development in Hollows*, Ph.D. dissertation, University of California, Berkeley, 1988.
- Yeh, G. T., *FEMWATER: A finite element model of water flow through saturated - unsaturated porous media-first revision*, Oak Ridge National Laboratory, Oak Ridge, Tenn., Rep. ORNL-5567/R1, 1987.
- Ziemer, R. R., *Effect of logging on subsurface pipeflow and erosion: coastal northern California, USA*, In: Erosion, Debris Flows and Environment in Mountain Regions, Proceedings of the Chendu Symposium, July 1992, Chendu, China, International Association of Hydrological Sciences Publication No. 209, 187-197, 1992.

## **APPENDIX A: Physical-Mathematical Basis of Numerical Model**

The decision to use SUTRA (Voss, 1984) as the physically based mathematical model, describing the groundwater flow within the E-Road system, is based primarily on the model's ability to simulate unsaturated conditions. SUTRA's capability of simulating the unsaturated conditions is, however, limited by the use of an empirical relationship for pressure-saturation. Derivation of the predictive equations describing groundwater flow requires an understanding of the fluid physical properties, properties of the fluid within the solid matrix, fluid flow and flow properties, unsaturated conditions, and the fluid mass balance. The dimensions associated with the groundwater parameters are: Length  $\doteq [L] \equiv$  meters, mass  $\doteq [M] \equiv$  kilograms, time  $\doteq [T] \equiv$  seconds, and unitless  $\doteq [l]$ .

### **1.1 Fluid Physical Properties:**

The primary variable for fluid flow within the groundwater system is fluid pressure. Fluid pressure is the exertion of force upon a surface by a fluid in contact with that surface:

$$p(x, z, t) \doteq \left[ \frac{M}{(L \cdot T^2)} \right] \quad (1.1.1)$$

where pressure,  $p$ , is a function of both space ( $x, z$ ) and time ( $t$ ). The density and dynamic viscosity of the fluid are given as,

$$\rho \doteq \left[ \frac{M}{L^3} \right] \quad (1.1.2)$$

$$\mu \doteq \left[ \frac{M}{L \cdot T} \right] \quad (1.1.3)$$

where  $\rho$  is approximated with a first order Taylor expansion about a base density and  $\mu$  is taken to be constant. Dynamic viscosity directly expresses ease of fluid flow; a less viscous fluid flows more readily under a driving force.

### 1.2 Properties of Fluid Within the Solid Matrix:

The total volume,  $\mathbb{V}_{\text{total}}$ , of the porous medium is composed of a matrix of solid grains and void space. The void space,  $\mathbb{V}_{\text{void}}$ , includes that portion of the total volume which the solid matrix does not fill. The volume of the void space may be fully or partly filled with air or water. Porosity,  $\epsilon$ , is defined as a volume of voids in the soil matrix per total volume.

$$\epsilon(x, z, t) \equiv \frac{\mathbb{V}_{\text{void}}}{\mathbb{V}_{\text{total}}} \doteq [l] \quad (1.2.1)$$

The product of porosity and water saturation,  $\epsilon S_w$ , gives the fraction of total volume filled by the fluid. Water saturation,  $S_w$ , is defined as the volume of water per volume of voids.

$$S_w(x, z, t) \equiv \frac{\mathbb{V}_{\text{water}}}{\mathbb{V}_{\text{void}}} \doteq [l] \quad (1.2.2)$$

When  $S_w = 1$ , the void space is completely filled with water and is said to be saturated. For  $S_w < 1$ , the void space is only partly filled with water and is referred to as being unsaturated.

When  $S_w < 1$ , water adheres to the surface of solid grains by surface tension effects, and the fluid pressure is less than atmospheric. Fluid pressure,  $p$ , is measured with respect to atmospheric pressure, ( $p_{\text{ATM}} = 0$  Pa). The negative pressure is defined as capillary pressure, which exists only for  $p < 0$ .

$$p_c(x, z, t) \doteq \begin{cases} \frac{M}{(L \cdot T^2)} & p < 0, \quad p_c = -p \\ 0 & p \geq 0, \quad p_c = 0 \end{cases} \quad (1.2.3)$$

In a saturated porous medium, as fluid pressure drops below zero, air may not directly enter the void space, but may suddenly penetrate when a critical capillary pressure is reached. This pressure,  $p_{\text{cent}}$ , is the entry pressure.

$$p_{\text{cent}} \doteq \left[ \frac{M}{(L \cdot T^2)} \right] \quad (1.2.4)$$

The relationship between fluid saturation and capillary pressure,  $S_w(p_c)$ , for a given medium is typically determined by laboratory experiment. Due to the variety of possible functions, no particular function is established by SUTRA; the desired function is user specified within the UNSAT subroutine of SUTRA. The functional relationship between saturation and capillary pressure within the E-Road system is defined with a general function. The  $S_w(p_c)$  relationship is given within the Unsaturated Conditions section of this report.

The total mass of fluid contained in a total volume is

$$M_f = (\epsilon S_w \rho) V_{\text{total}} \equiv \left( \frac{V_{\text{void}}}{V_{\text{total}}} \frac{V_{\text{water}}}{V_{\text{void}}} \frac{M}{V_{\text{water}}} \right) V_{\text{total}} \doteq [M] \quad (1.2.5)$$

The actual amount of total fluid mass,  $M_f$ , depends solely on fluid pressure,  $p$ . A change in total fluid mass in a volume, assuming  $V_{\text{total}}$  is constant, is expressed as:

$$d(M_f) = \frac{\partial(M_f)}{\partial p} dp \quad (1.2.6)$$

$$d(\epsilon S_w \rho) \cdot V_{\text{total}} = \left[ \frac{\partial(\epsilon S_w \rho)}{\partial p} dp \right] \cdot V_{\text{total}} \quad (1.2.7)$$

Saturation,  $S_w$ , is entirely dependent on fluid pressure,  $p$ .

$$d(\epsilon S_w \rho) = \left[ S_w \frac{\partial(\epsilon \rho)}{\partial p} + \epsilon \rho \frac{\partial(S_w)}{\partial p} \right] dp \quad (1.2.8)$$

The factor,  $\frac{\partial S_w}{\partial p}$ , is obtained by differentiation of the chosen saturation-capillary pressure relationship.

By definition, the aquifer storativity under fully saturated conditions is related to the factor,  $\frac{\partial(\epsilon\rho)}{\partial p}$  (Bear, 1979),

$$\frac{\partial(\epsilon\rho)}{\partial p} = \rho S_{op} \quad (1.2.9)$$

where the specific pressure storativity,  $S_{op}$ , is the volume of water released from saturated pore storage due to a unit drop in fluid pressure per total solid matrix plus pore volume.

$$S_{op}(x, z) = \frac{1}{V_{\text{total}}} \left( \frac{\Delta V_{\text{water}}}{\Delta p} \right) \doteq \left[ \frac{(L \cdot T^2)}{M} \right] \quad (1.2.10)$$

SUTRA employs an expanded form of the specific pressure storativity based on fluid and bulk porous matrix compressibility. The relationship is obtained as follows by expanding Equation (1.2.9).

$$\rho S_{op} = \frac{\partial(\epsilon\rho)}{\partial p} = \rho \frac{\partial \epsilon}{\partial p} + \epsilon \frac{\partial \rho}{\partial p} \quad (1.2.11)$$

The coefficient of compressibility of water is defined by

$$\beta \equiv \frac{1}{\rho} \frac{\partial \rho}{\partial p} \doteq \left[ \frac{(L \cdot T^2)}{M} \right] \quad (1.2.12)$$

and solving for  $\frac{\partial \rho}{\partial p}$  yields

$$\frac{\partial \rho}{\partial p} = \rho \beta \quad (1.2.13)$$

substituting for  $\frac{\partial \rho}{\partial p}$  in Equation (1.2.11) gives

$$\rho S_{op} = \rho \frac{\partial \epsilon}{\partial p} + \epsilon \rho \beta \quad (1.2.14)$$

Further development of Equation (1.2.14) requires the definition of a solid grain volume,  $\mathbb{V}_{\text{solid}}$ .

$$\mathbb{V}_{\text{solid}} = (1 - \epsilon) \cdot \mathbb{V}_{\text{total}} \quad (1.2.15)$$

The volume of the solid grains,  $\mathbb{V}_{\text{solid}}$ , is considered as constant because the compressibility of the individual grains is considerably less than that of their skeleton and is also less than the compressibility of water. The total derivative of this quantity is zero, or

$$d(\mathbb{V}_{\text{solid}}) = d[(1 - \epsilon) \cdot \mathbb{V}_{\text{total}}] = 0 \quad (1.2.16)$$

$$d[\mathbb{V}_{\text{total}} - \mathbb{V}_{\text{total}}\epsilon] = 0$$

$$d(\mathbb{V}_{\text{total}}) - [d(\mathbb{V}_{\text{total}})\epsilon + \mathbb{V}_{\text{total}}d(\epsilon)] = 0$$

$$\partial \mathbb{V}_{\text{total}} - \partial \mathbb{V}_{\text{total}}(\epsilon) = \partial \epsilon (\mathbb{V}_{\text{total}})$$

$$\partial \epsilon = \frac{\partial \mathbb{V}_{\text{total}}[1 - \epsilon]}{\mathbb{V}_{\text{total}}}$$

Dividing through by the change in fluid pressure,  $dp$ , yields

$$\frac{\partial \epsilon}{\partial p} = \frac{(1 - \epsilon)}{\mathbb{V}_{\text{total}}} \left( \frac{\partial \mathbb{V}_{\text{total}}}{\partial p} \right) \quad (1.2.17)$$

The stress at any point in the solid matrix-fluid system is the sum of intergranular stress,  $\sigma'$ , and fluid pore pressure,  $p$ .

$$\sigma' \doteq \left[ \frac{M}{(L \cdot T^2)} \right] \quad (1.2.18)$$

Within the E-Road system, total stress is assumed to remain nearly constant,  $d\sigma' = -dp$ , and any drop in fluid pressure increases the intergranular stress by a like

amount. This consideration allows Equation (1.2.17) to be expressed in terms of porous matrix compressibility, as

$$\frac{\partial \epsilon}{\partial p} = (1 - \epsilon)\alpha \quad (1.2.19)$$

where  $\alpha$  is the porous matrix compressibility,

$$\alpha = -\frac{1}{V_{\text{total}}} \frac{\partial V_{\text{total}}}{\partial \sigma'} = \frac{1}{V_{\text{total}}} \frac{\partial V_{\text{total}}}{\partial p} \doteq \left[ \frac{(L \cdot T^2)}{M} \right] \quad (1.2.20)$$

Equation (1.2.14) is rewritten as,

$$\rho S_{op} = \rho [(1 - \epsilon)\alpha] + \epsilon [\rho \beta]$$

$$S_{op} = (1 - \epsilon)\alpha + \epsilon \beta \quad (1.2.21)$$

### 1.3 Fluid Flow And Flow Properties:

Fluid movement in a porous medium is driven by differences in fluid potential. Pressure-driven flows are directed from regions of higher fluid pressure toward regions of lower fluid pressure. The mechanisms of pressure driving forces for flow are expressed for SUTRA simulations by a general form of Darcy's law. The development of the general form of Darcy's law is presented below.

In 1856, Henry Darcy investigated the flow of water in vertical homogeneous sand filters in connection with the fountains of the city of Dijon, France. Similar to Darcy's original experiment, Figure A.1, shows an experimental setup for seepage through an inclined surface. From his experiments, Darcy concluded that the rate of fluid flow  $Q$  is (a) proportional to the constant cross-sectional area,  $A$ , (b)

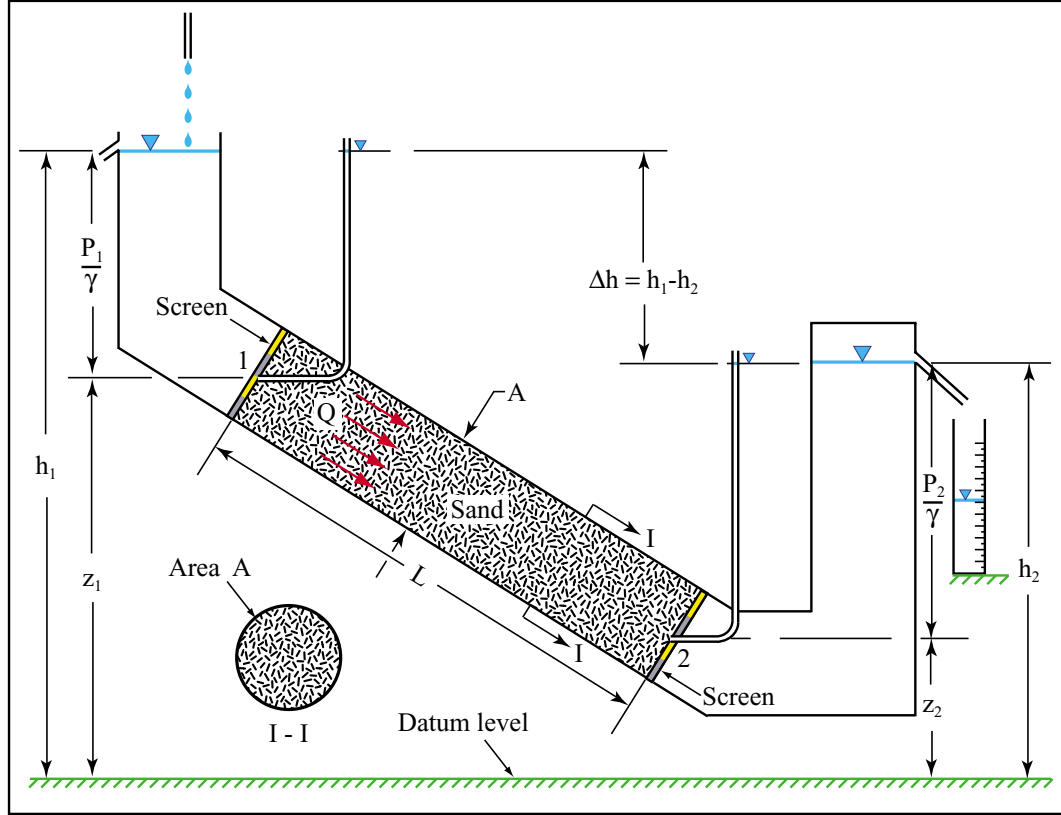


**Figure A.1:** Seepage through an inclined sand filter.

proportional to the difference in piezometric head across the filter,  $h_1 - h_2$ , and (c) inversely proportional to the length, L (Bear, 1972). The Darcy formula is given as

$$Q = KA \frac{(h_1 - h_2)}{L} \quad (1.3.1)$$

where **K** is a coefficient of proportionality or more commonly known as the hydraulic conductivity. The hydraulic gradient,  $\nabla h$ , is defined as,

$$\nabla h = \frac{\partial h}{\partial s} = \frac{h_2 - h_1}{s_2 - s_1} = \frac{-(h_2 - h_1)}{L} \quad (1.3.2)$$

where  $s$  is a spatial distance. Substituting the hydraulic gradient into equation (1.3.1) gives

$$Q = -KA\nabla h \quad (1.3.3)$$

The specific discharge,  $\mathbf{q}$ , is defined as the discharge per unit cross-sectional area normal to the direction of flow.

$$\mathbf{q} = \frac{Q}{A} \doteq \left[ \frac{L}{T} \right] \quad (1.3.4)$$

Substituting  $\mathbf{q}$  into Equation (1.3.3) gives

$$\mathbf{q} = -\mathbf{K} \nabla h \quad (1.3.5)$$

where

$$\nabla h = \frac{\partial \mathbf{h}}{\partial s} = \frac{dh}{dx} \hat{\mathbf{i}} + \frac{dh}{dy} \hat{\mathbf{j}} + \frac{dh}{dz} \hat{\mathbf{k}} \quad (1.3.6)$$

and  $\hat{\mathbf{i}}, \hat{\mathbf{j}}, \hat{\mathbf{k}}$  are unit vectors in the  $x, y, z$  coordinate directions, respectively.

The functional relationship between hydraulic head,  $h$ , and fluid pressure,  $p$ , is defined as

$$h = \int_{p_0}^p \frac{dp}{\gamma} + \frac{\bar{v}^2}{2g} + z \quad (1.3.7)$$

where  $\gamma$  is the specific weight of water,  $\bar{v}$ , is the average fluid velocity, and  $z$  is the vertical distance above an established datum. It is assumed that changes in piezometric head,  $h$ , are much larger than changes in the kinetic energy head along the flow path. Fluid velocities are assumed insignificant when compared with the pressure and elevation terms in Equation (1.3.8). Therefore, kinetic energy is neglected when considering the head loss along the flow path.

$$h = \int_{p_0}^p \frac{dp}{\gamma} + z \quad (1.3.8)$$

or

$$\nabla h = \frac{\nabla p}{\gamma} + \nabla z \quad (1.3.9)$$

For cases where density or viscosity are not constant, SUTRA utilizes a simplified version of the hydraulic conductivity,

$$\mathbf{K} = \frac{cd^2\gamma}{\mu} = \frac{\mathbf{k}k_r\gamma}{\mu} \quad (1.3.10)$$

where  $c$  is the shape factor and  $d$  is the mean grain diameter. Both  $c$  and  $d$  are based on the properties of the porous media. Fluid velocity, even for a given pressure and density distribution, may take on different values depending on how mobile the fluid is within the solid matrix. Fluid mobility depends on the combination of permeability,  $\mathbf{k}$ , relative permeability,  $k_r$ , and dynamic viscosity,  $\mu$ . Permeability is a measure of the ease of fluid movement through interconnected voids in the isotropic solid matrix when all voids are completely saturated. Relative permeability expresses the fraction of the total permeability remaining when the voids are only partly fluid-filled and only part of the total interconnected void space is connected by continuous fluid channels. SUTRA assumes  $k_r$  to be independent of direction in the isotropic porous media.

Returning to Equation (1.3.6), Darcy's law is further developed.

$$\mathbf{q} = -\mathbf{K}\nabla h = -\left[\frac{\mathbf{k}k_r\gamma}{\mu}\right]\left[\frac{\nabla p}{\gamma} + \nabla z\right] = \frac{-\mathbf{k}k_r\gamma}{\mu\gamma}(\nabla p + \gamma\nabla z) \quad (1.3.11)$$

The average fluid velocity,  $\bar{v}$ , is the velocity of fluid with respect to the stationary solid matrix. By definition, the specific discharge,  $\mathbf{q}$ , is

$$\mathbf{q} = \epsilon S_w \bar{v} \equiv \frac{\mathbb{V}_{\text{void}}}{\mathbb{V}_{\text{total}}} \frac{\mathbb{V}_{\text{water}}}{\mathbb{V}_{\text{void}}} \bar{v} \doteq \left[\frac{L}{T}\right] \quad (1.3.12)$$

Substituting for  $\mathbf{q}$  in Equation (1.3.12) gives

$$\epsilon S_w \bar{v} = \frac{-\mathbf{k}k_r}{\mu}(\nabla p + \gamma\nabla z)$$

$$\underline{v} = \frac{-\mathbf{k}k_r}{\epsilon S_w \mu} (\nabla p + \rho g \nabla z) \quad (1.3.13)$$

The gravity vector is defined in relation to the direction in which vertical elevation is measured

$$\underline{\mathbf{g}} = -|g| \nabla z \Rightarrow g = -\frac{\underline{\mathbf{g}}}{\nabla z} \quad (1.3.14)$$

where  $\underline{\mathbf{g}}$  is the magnitude of the gravitational acceleration vector. Substituting  $g$  into Equation (1.3.14) gives the average velocity as

$$\underline{v} = -\left(\frac{\mathbf{k}k_r}{\epsilon S_w \mu}\right) \cdot (\nabla p - \rho \underline{\mathbf{g}}) \quad (1.3.15)$$

A functional relationship between permeability and pressure is required by SUTRA within the UNSAT subroutine. A general function of  $k_r(p)$ , will be used and is given within the Unsaturated Conditions section of this report.

#### 1.4 Partially Saturated Conditions:

A predictive model is used to describe the movement of groundwater within partially saturated conditions (negative pressure fields). The model is specifically used to predict the relative permeability of unsaturated soils for a given water pressure. To derive the relative permeability in the unsaturated state, the model makes use of the measured pressure head versus water saturation curve,  $p(S_w)$ . The models development, as outlined by Mualem (1976), is presented below.

Consider a homogeneous porous medium having interconnected pores defined by their radius  $r$ . Pores within the medium, at complete saturation, go from a radius of  $r$  to  $r + dr$ . The change in radii,  $r \rightarrow r + dr$ , within the full pores contributes

to a change in water saturation. If  $f(r)$  is the pore water distribution function, the contribution to  $S_w$  is

$$f(r)dr = dS_w \quad (1.4.1)$$

Integration over the pore radii gives water saturation as a function of the pore radius

$$\int_{r_{\min}}^r f(r)dr = S_w(r) \quad (1.4.2)$$

and for saturated conditions,

$$\int_{r_{\min}}^{r_{\max}} f(r)dr = S_{\text{sat}} \quad (1.4.3)$$

The areal porosity,  $\frac{A_{\text{void}}}{A_{\text{total}}}$ , is equal to the volumetric porosity,  $\frac{V_{\text{void}}}{V_{\text{total}}}$ , so  $f(r)dr$  represents the ratio between the pore area of radii  $r \rightarrow r+dr$  and the total area (Mualem, 1976).

Consider a conceptual soil structure, Figure A.2, where a porous slab of thickness  $\Delta x$  hypothetically isolates a homogeneous soil column. The pore area distribution for the two slab sides is identical and equal to  $f(r)dr$ . For  $\Delta x$  much larger than the maximum radius,  $\Delta x \gg r_{\max}$ , complete randomness of the relative position of the voids at the two slab faces would exist. The independence of pore distributions at  $x$  and  $x + \Delta x$  implies that their probability for intersecting is

$$dA_e = [f(r_1)dr_1][f(r_2)dr_2] = f(r_1)f(r_2)dr_1dr_2 \quad (1.4.4)$$

where  $dA_e$  is both the change in pore area and the probability that a pore of radius  $r_1$  finds a pore of radius  $r_2$  when moving over a distance of  $\Delta x$ . For  $0 \leq \Delta x < r_{\max}$  there exists a correlation between  $r_1$  and  $r_2$  with perfect correlation at  $\Delta x = 0$ . To

account for the degree of correlation between the two sides, the change in pore area,  $dA_e$ , is rewritten with a dependency on water saturation,  $S_w$ ,

$$dA_e = S_w^{u-2} f(r_1) f(r_2) dr_1 dr_2 \quad (1.4.5)$$

where  $u$  describes the connectivity of the pore structure. The parameter  $u$  ranges from  $u = 1$  for full correlation to  $u = 2$  for no correlation. For a given water saturation, integration of Equation (1.4.5) over the range of radii of the water-filled pores is

$$A_e = \int_{r_{\min}}^{r_{\max}} dA_e = \int_{r_{\min}}^{r_{\max}} \int_{r_{\min}}^{r_{\max}} S_w^{u-2} f(r_1) f(r_2) dr_1 dr_2 \quad (1.4.6)$$

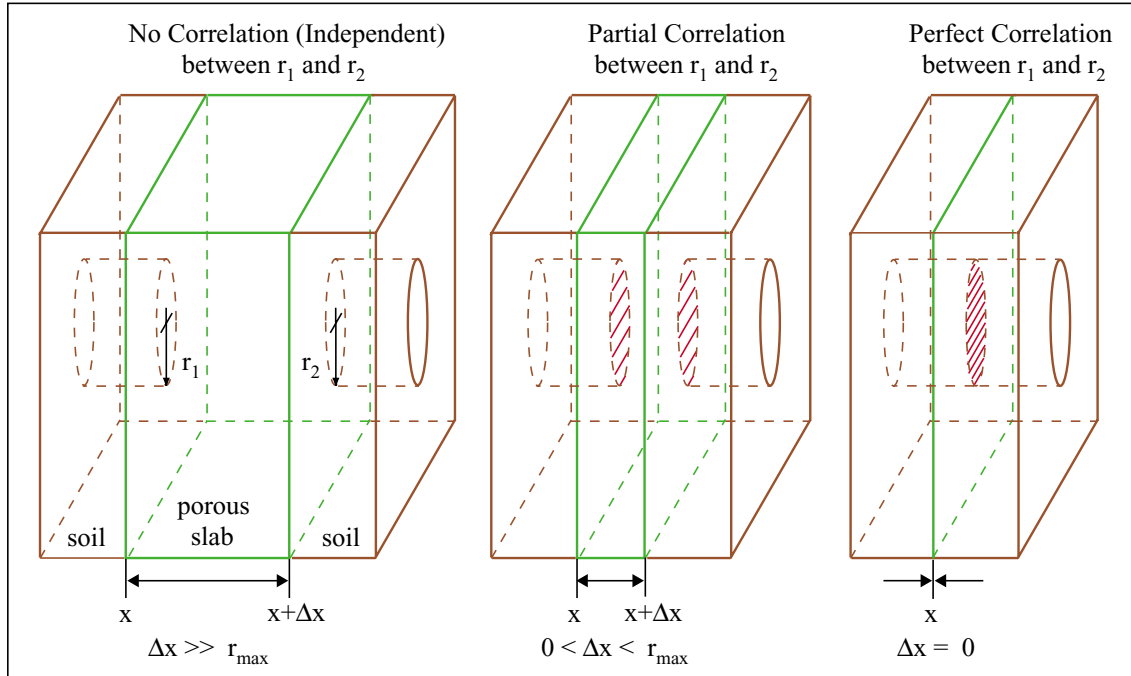


**Figure A.2:** Variations of  $\Delta x$  within a conceptual soil structure. Homogeneous soil with pore area distributions identical at the two slab sides, (1) & (2).

The contribution of the actual flow configuration in the slab to the hydraulic conductivity,  $K$ , requires two simplifying assumptions: (1) there is no bypass flow

between slab pores, and (2) the pore configuration may be replaced by a pair of capillary elements (Figure A.3a) whose lengths are proportional to their radii (Mualem, 1976).

$$\frac{L_1}{L_2} = \frac{r_1}{r_2} \quad (1.4.7)$$

Figure A.3 shows (A) a pair of capillary elements represented by (B) an equivalent single scaled capillary element; where  $r_e$  and  $A_e$  is the effective radius and area, respectively. Relying on Poiseuille's equation, the change in effective radius is given as

$$d(r_e^2) = r_1 r_2 \quad (1.4.8)$$

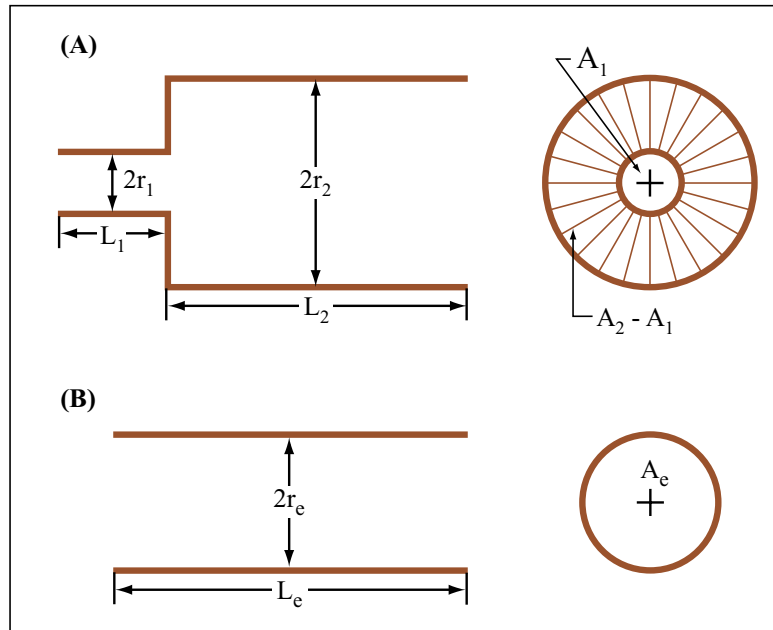


**Figure A.3:** Unknown pore configuration, represented as a pair of capillary elements (A), is replaced with an equivalent cylindrical pore (B).

Tortuosity of pores is accounted for by reducing the change in effective radius by a factor of  $S_w^m$ .

$$d(\hat{r}_e^2) = S_w^m r_1 r_2 \quad (1.4.9)$$

Darcy's Law (Equation 1.3.3) applied to the equivalent tube (Figure A.3b) yields

$$Q = -KA\nabla h = -\left(\frac{cd^2\gamma}{\mu}\right)(A_e \cdot A_{\text{sat}})\nabla h \quad (1.4.10)$$

where the effective area is given as

$$A_e = \frac{A}{A_{\text{sat}}} \Rightarrow A = A_e \cdot A_{\text{sat}} \quad (1.4.11)$$

where  $A_{\text{sat}}$  is the pore area at saturation. Darcy's Law in terms of the specific discharge,  $q$ , is given as

$$\begin{aligned} q &= -\left(\frac{cd^2\gamma}{\mu}\right)A_e\nabla h = -\left(\frac{c\gamma}{\mu}\right)d^2A_e\nabla h \dots \\ \dots &= -Md^2A_e\nabla h = -(M\hat{r}_e^2A_e)\nabla h \end{aligned} \quad (1.4.12)$$

where  $M = \frac{c\gamma}{\mu}$  is a constant which incorporates properties of the fluid and solid matrix. The effective radius,  $\hat{r}_e$ , is assumed equal to mean grain diameter,  $d$ . The changes in flux resulting from the contribution of full pores going from  $r$  to  $r + dr$  is

$$dq = d[-M\hat{r}_e^2A_e\nabla h] = -Md\hat{r}_e^2dA_e\nabla h \quad (1.4.13)$$

Integrating the specific discharge over the water filled pores gives

$$q = \int dq = -\left[M' \int_{\text{water filled pores}} d\hat{r}_e^2 dA_e\right] \nabla h \quad (1.4.14)$$

which allows  $K$  to be isolated from the modified form of Darcy's Law (Equation 1.4.14).

$$K = M' \int_{\text{water filled pores}} d\hat{r}_e^2 dA_e \quad (1.4.15)$$

The relative permeability,  $k_r$ , is expressed as

$$k_r = \frac{K(S_w)}{K_{\text{sat}}} = \frac{\frac{\text{M}' \int_{\text{water filled pores}} d\hat{r}_e^2 dA_e}{\text{M}' \int_{\text{water filled pores at saturation}} d\hat{r}_e^2 dA_e}}{\frac{\int_{\text{filled pores}} d\hat{r}_e^2 dA_e}{\int_{\text{all pores}} d\hat{r}_e^2 dA_e}} \quad (1.4.16)$$

Definitions for  $d\hat{r}_e^2$  (Equation 1.4.9) and  $dA_e$  (Equation 1.4.5) are then incorporated within Equation (1.4.16). Integration takes place over the radii of the pore domains.

$$\begin{aligned} k_r &= \frac{\int_{r_{\min}}^r \int_{r_{\min}}^r S_w^m r_1 r_2 S_w^{u-2} f(r_1) f(r_2) dr_1 dr_2}{\int_{r_{\min}}^{r_{\max}} \int_{r_{\min}}^{r_{\max}} S_{\text{sat}}^m r_1 r_2 S_{\text{sat}}^{u-2} f(r_1) f(r_2) dr_1 dr_2} \dots \\ \dots &= \frac{S_w^{m+u-2} \int_{r_{\min}}^r \int_{r_{\min}}^r r_1 r_2 f(r_1) f(r_2) dr_1 dr_2}{S_{\text{sat}}^{m+u-2} \int_{r_{\min}}^{r_{\max}} \int_{r_{\min}}^{r_{\max}} r_1 r_2 f(r_1) f(r_2) dr_1 dr_2} \end{aligned} \quad (1.4.17)$$

By definition, the effective saturation is expressed as

$$S_e = \frac{S_w}{S_{\text{sat}}} \quad (1.4.18)$$

which reduces the function for  $k_r$  (Equation 1.4.17) to

$$k_r = S_e^{m+u-2} \left[ \frac{\int_{r_{\min}}^r \int_{r_{\min}}^r r_1 r_2 f(r_1) f(r_2) dr_1 dr_2}{\int_{r_{\min}}^{r_{\max}} \int_{r_{\min}}^{r_{\max}} r_1 r_2 f(r_1) f(r_2) dr_1 dr_2} \right] \quad (1.4.19)$$

Note,  $r_e^2 = r_e r_e = r_1 r_2$ , which allows

$$\begin{aligned} k_r &= S_e^{m+u-2} \left[ \frac{\int_{r_{\min}}^r \int_{r_{\min}}^r r_e r_e f(r_e) f(r_e) dr_e dr_e}{\int_{r_{\min}}^{r_{\max}} \int_{r_{\min}}^{r_{\max}} r_e r_e f(r_e) f(r_e) dr_e dr_e} \right] \dots \\ \dots &= S_e^{m+u-2} \left[ \frac{\int_{r_{\min}}^r r_e f(r_e) dr_e \int_{r_{\min}}^r r_e f(r_e) dr_e}{\int_{r_{\min}}^{r_{\max}} r_e f(r_e) dr_e \int_{r_{\min}}^{r_{\max}} r_e f(r_e) dr_e} \right] \dots \\ \dots &= S_e^{m+u-2} \left[ \frac{\int_{r_{\min}}^r r_e f(r_e) dr_e}{\int_{r_{\min}}^{r_{\max}} r_e f(r_e) dr_e} \right]^2 \end{aligned} \quad (1.4.20)$$

The capillary law, expressing the inverse proportionality of the maximum radius of the water filled pores and the capillary pressure head is

$$r = \frac{C}{p_c} \quad (1.4.21)$$

where C is a proportionality constant. Expressing  $k_r$  in terms of  $p$  and substituting for  $f(r_e)dr = dS_e$  from Equation (1.4.1) yields

$$k_r = S_e^{m+u-2} \left[ \frac{\int_0^{S_e} \left( \frac{C}{p_c} \right) dS_e}{\int_0^{S_{sat}} \left( \frac{C}{p_c} \right) dS_w} \right]^2 = S_e^{m+u-2} \left[ \frac{\int_0^{S_w} \left( \frac{1}{p_c} \right) dS_e}{\int_0^{S_{sat}} \left( \frac{1}{p_c} \right) dS_e} \right]^2 \quad (1.4.22)$$

Since there exists no procedure for an independent determination of m, the effects of tortuosity, and u, the correlation factors, both m and u are lumped together into a single parameter n.

$$n = m + u - 2 \quad (1.4.23)$$

The parameter n is determined from a curve fitting technique between  $k_r(p_c)$  in Equation (1.4.22) and the empirical relation of  $k_{rm}(p_c)$  found through experiment. For each soil the mean square deviation, D, between  $k_{rm}$  and  $k_r$  is

$$D = \left[ \int_{S_e \text{ min}}^1 \frac{[\ln(k_r) - \ln(k_{rm})]^2}{(1 - S_e \text{ min})} dS_e \right]^{\frac{1}{2}} \quad (1.4.24)$$

Posing the problem as a parameter estimation optimization gives the objective as the minimization of the error between measured and computed permeability while treating n as the decision variable. The problem associated with this technique is the dependency of n on the specific soil type being used. A general n value which could be used for all soils was determined by Mualem (1976). In order to maintain consistency in the numerical computation of D for all soils, Mualem solved for a mean value of  $\bar{D}$  based on 45 common soils. Each of the 45 soils are cited within the literature and contain measured  $p$ - $S_e$  and  $K$ - $S_w$  data on drainage. Holding n constant, a  $\bar{D}$  value is calculated. The magnitude of  $\bar{D}$  represents the performance of n in characterizing the 45 soils. Mualem's results, Figure A.4, show an optimal solution of  $n = \frac{1}{2}$ .

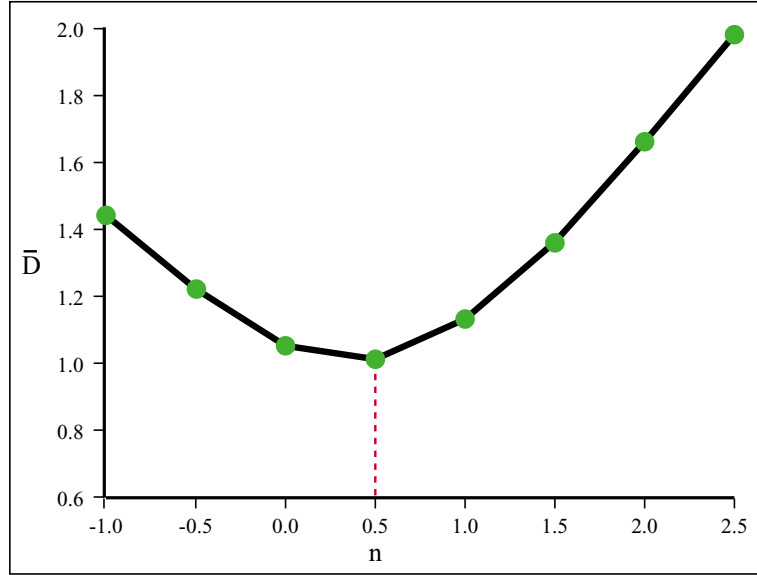


**Figure A.4:** Computed  $\bar{D}$  based on 45 soils as a function of the power  $n$  (Mualem, 1976).

To solve Equation (1.4.22), an expression relating the dimensionless saturation or effective saturation,  $S_e$ , to the capillary pressure,  $p_c$ , is needed. The functional relationship,  $S_e(p_c)$ , adopted for this study was established by van Genuchten (1980) and is given in its general form as

$$S_e = \left[ \frac{1}{1 + (ap_c)^n} \right]^m \quad (1.4.25)$$

where  $a$ ,  $n$ , and  $m$  are parameters dependent on the materials within the study site.

Solving for the capillary pressure,  $p_c$ , within Equation (1.4.25), yields

$$\begin{aligned} S_e^{\frac{1}{m}} &= \frac{1}{1 + (ap_c)^n} \Rightarrow (ap_c)^n = \frac{1}{S_e^{\frac{1}{m}}} - 1 \Rightarrow \dots \\ \dots \quad ap_c &= \left[ \frac{1}{S_e^{\frac{1}{m}}} \right]^{\frac{1}{n}} \Rightarrow p_c = \frac{1}{a} \left[ \frac{1 - S_e^{\frac{1}{m}}}{S_e^{\frac{1}{m}}} \right]^{\frac{1}{n}} \end{aligned} \quad (1.4.26)$$

Equation (1.4.22) is further developed with the capillary pressure definition given

in Equation (1.4.26). A substitution for  $n = \frac{1}{2}$  is made.

$$k_r(S_e) = S_e^{\frac{1}{2}} \left[ \frac{\int_0^{S_e} \frac{1}{p_c} dS_e}{\int_0^1 \frac{1}{p_c} dS_e} \right]^2 = S_e^{\frac{1}{2}} \left[ \frac{f(S_e)}{f(S_{e,\text{sat}})} \right]^2 \quad (1.4.27)$$

where

$$\begin{aligned} f(S_e) &= \int_0^{S_e} \frac{1}{p_c} dS_e = \int_0^{S_e} \frac{1}{\frac{1}{a} \left[ \frac{1-S_e^{\frac{1}{m}}}{S_e^{\frac{1}{m}}} \right]^{\frac{1}{n}}} dS_e \quad \dots \\ \dots &= a \int_0^{S_e} \left[ \frac{S_e^{\frac{1}{m}}}{1 - S_e^{\frac{1}{m}}} \right]^{\frac{1}{n}} dS_e \end{aligned} \quad (1.4.28)$$

The relative permeability,  $k_r$ , is assumed a power function of the effective saturation,  $S_e$ . Substitution of  $S_e = S^m$  into Equation (1.4.28) leads to

$$\begin{aligned} f(S) &= a \int_0^{S^{\frac{1}{m}}} \left[ \frac{(S^m)^{\frac{1}{m}}}{(1 - (S^m)^{\frac{1}{2}})} \right]^{\frac{1}{n}} d(S^m) \quad \dots \\ \dots &= a \int_0^{S^{\frac{1}{2}}} \frac{S^{\frac{1}{n}}}{(1 - S)^{\frac{1}{n}}} (mS^{m-1}) dS = am \int_0^{S^{\frac{1}{m}}} S^{m-1+\frac{1}{n}} (1 - S)^{-\frac{1}{n}} dS \quad \dots \\ \dots &= am \int_0^{S^{\frac{1}{m}}} S^k (1 - S)^{-\frac{1}{n}} dS \end{aligned} \quad (1.4.29)$$

where  $m$  is limited to  $(0 < m < 1)$ . In it's most general form, no closed-form expression can be derived for Equation (1.4.29). However, integration is possible for all integer values of  $k$ , where  $k = m - 1 + \frac{1}{n}$ . For the particular case when  $k = 0$  (i.e.  $m = \frac{n-1}{n}$  and  $\frac{1}{n} = 1 - m$ ), integration of Equation (1.4.29) gives

$$\begin{aligned} f(S) &= am \int_0^{S^{\frac{1}{m}}} S^{m-1+(1-m)} (1 - S)^{-(1-m)} dS \quad \dots \\ \dots &= am \int_0^{S^{\frac{1}{2}}} S^0 (1 - S)^{m-1} dS \quad \dots \end{aligned}$$

$$\dots = am \left[ \frac{(1-S)^m}{m} \right]_0^{S_e^{\frac{1}{2}}} = a \left[ (1 - S_e^{\frac{1}{m}})^m - 1 \right] \quad (1.4.30)$$

Equation (1.4.29) in terms of the effective saturation,  $S_e$ , and the effective saturation at saturation,  $S_{e,\text{sat}}$ , is

$$f(S_e) = a \left[ (1 - S_e^{\frac{1}{m}})^m - 1 \right] \quad (1.4.31)$$

$$f(S_{e,\text{sat}}) = a \left[ (1 - 1^{\frac{1}{m}})^m - 1 \right] = -a \quad (1.4.32)$$

which allows Equation (1.4.27) to be written as,

$$k_r(S_e) = S_e^{\frac{1}{2}} \left[ \frac{a(1 - S_e^{\frac{1}{m}})^m - 1}{-a} \right]^2 = S_e^{\frac{1}{2}} \left[ 1 - (1 - S_e^{\frac{1}{m}})^m \right]^2 \quad (1.4.33)$$

Substituting the effective saturation,  $S_e$ , found in Equation (1.4.25), into Equation (1.4.32) gives the relative permeability as a function of capillary pressure,  $k_r(p_c)$ .

$$\begin{aligned} k_r(p_c) &= \left[ \frac{1}{1 + (ap_c)^n} \right]^{\frac{m}{2}} \left\{ 1 - \left( 1 - \left[ \frac{1}{1 + (ap_c)^n} \right]^{\frac{m}{m}} \right)^m \right\}^2 \dots \\ \dots &= \left[ \frac{1}{\{1 + (ap_c)^n\}^{\frac{m}{2}}} \right] \left\{ 1 - \left( \frac{1 - (ap_c)^n - 1}{1 + (ap_c)^n} \right)^m \right\}^2 \dots \\ \dots &= \frac{\left[ 1 - (ap_c)^{nm} (1 + (ap_c)^n)^{-m} \right]^2}{(1 + (ap_c)^n)^{\frac{m}{2}}} \end{aligned} \quad (1.4.34)$$

where

$$m = 1 - \frac{1}{n} \quad (1.4.35)$$

when  $k = 0$ . The dimensionless saturation,  $S_e$  is defined as

$$S_e = \frac{S_w - S_{w\text{res}}}{S_{\text{sat}} - S_{w\text{res}}} \quad (1.4.36)$$

where  $S_{w\text{res}}$  is a residual saturation below which saturation is not expected to fall. Water becomes immobile for  $S_w < S_{w\text{res}}$ . Equation (1.4.25) in terms of the residual saturation is given as

$$S_w = S_{w\text{res}} + (S_{\text{sat}} - S_{w\text{res}}) \left[ \frac{1}{1 + (ap_c)^n} \right]^m \quad (1.4.37)$$

Substituting for  $m$  in Equation (1.4.37) gives the water saturation as a function of capillary pressure,  $p_c$ .

$$\begin{aligned} S_w(p_c) &= S_{w\text{res}} + (S_{\text{sat}} - S_{w\text{res}}) \left[ \frac{1}{1 + (ap_c)^n} \right]^{\frac{n-1}{n}} \dots \\ \dots &= S_{w\text{res}} + (1 - S_{w\text{res}}) [1 + (ap_c)^n]^{\frac{1-n}{n}} \end{aligned} \quad (1.4.38)$$

Steps taken for the derivation of  $S_w$  with respect to  $p$  are as follows:

$$\begin{aligned} \frac{dS_w}{dp} &= (S_{\text{sat}} - S_{w\text{res}}) \left( \frac{1-n}{n} \right) [1 + (a(-p))^n]^{(\frac{1-n}{n}-1)} (n)(a(-p))^{n-1}(a)(-1) \dots \\ \dots &= (S_{\text{sat}} - S_{w\text{res}}) \left( \frac{n-1}{n} \right) [1 + (a(-p))^n]^{-\frac{2n-1}{n}} (n)(a(-p))^{n-1}(a) \dots \\ \dots &= \frac{(a)(n-1)(S_{\text{sat}} - S_{w\text{res}})(a(-p))^{n-1}}{[1 + (a(-p))^n]^{\frac{2n-1}{n}}} \end{aligned} \quad (1.4.39)$$

where  $p = -p_c$ . The user-programmed subroutine UNSAT, located within SUTRA, requires (A) water saturation as a function of pressure, (B) the derivative of saturation with respect to pressure, and (C) the relative permeability as a function of pressure. The three required conditions are given below:

$$S_w(p) = S_{w\text{res}} + (S_{\text{sat}} - S_{w\text{res}}) [1 + (a|p|)^n]^{-m} \quad (1.4.40)$$

$$\frac{dS_w}{dp} = \frac{(a)(n-1)(S_{\text{sat}} - S_{w\text{res}})(a|p|)^{n-1}}{[1 + (a|p|)^n]^{\frac{2n-1}{n}}} \quad (1.4.41)$$

$$k_r(p) = \frac{[1 - (a|p|)^{n-1}(1 + (a|p|)^n)^{-m}]^2}{(1 + (a|p|)^n)^{\frac{m}{2}}} \quad (1.4.42)$$

where  $m = 1 - 1/n$  and  $p < 0$ . Functions (A) and (C) are presented graphically in Figures A.5 and A.6, respectively. Unsaturated parameter values are based upon physical properties identified for Webster clay loam: a fine-loamy, mixed, superactive, mesic, Typic Endoaquoll, 32% sand, 39% silt, and 28% clay (Shao and Horton, 1998).

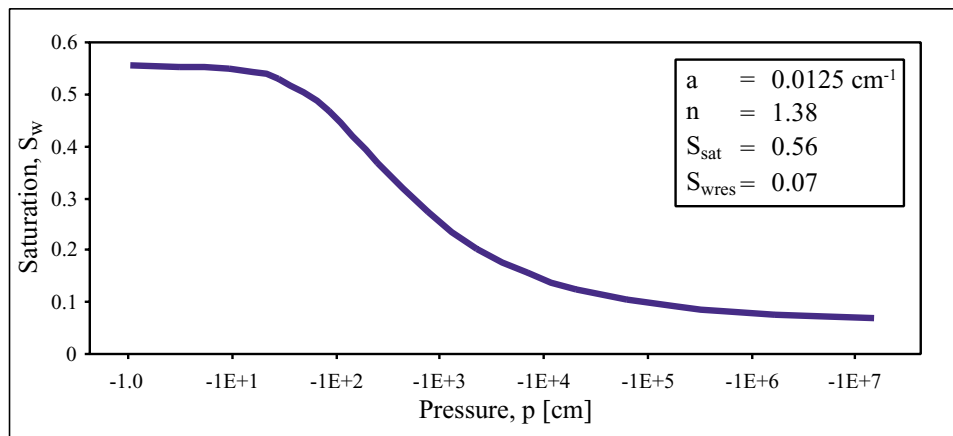


**Figure A.5:** Water saturation versus pressure.

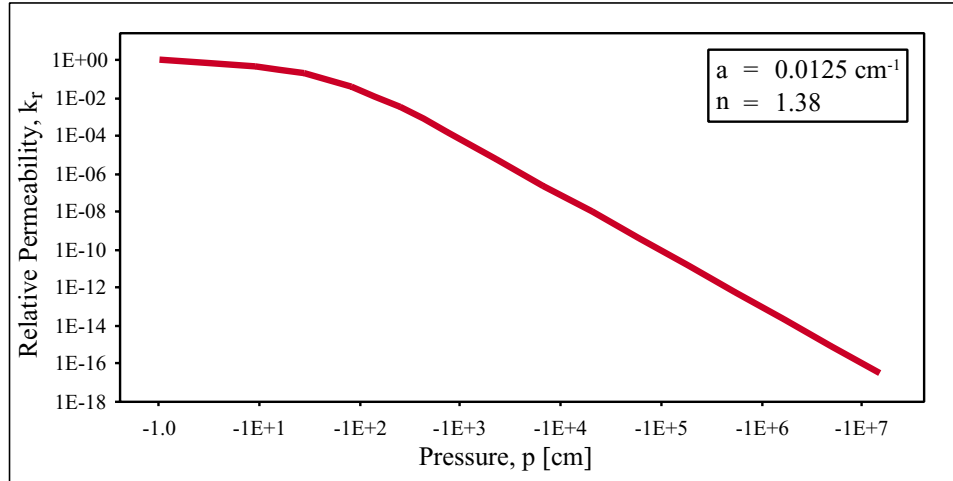


**Figure A.6:** Relative permeability versus pressure.

### 1.5 Fluid Mass Balance:

Simulation of flow within SUTRA is nothing more than a calculation of how the amount of fluid mass contained within the void spaces of the solid matrix changes with time. A fluid mass balance is used to keep track of the fluid mass held at every point in the simulated groundwater system as it changes with time due to flows and saturation changes. The continuity equation for the groundwater system is developed by considering a nondeforming elemental volume located within the aquifer (Figure A.7). The principle of mass conservation requires,

$$\left| \begin{array}{c} \text{Mass} \\ \text{inflow rate} \end{array} \right| - \left| \begin{array}{c} \text{Mass} \\ \text{outflow rate} \end{array} \right| = \left| \begin{array}{c} \text{Time rate of change} \\ \text{in mass storage} \end{array} \right| \quad (1.5.1)$$

or

$$\mathbf{I} - \mathbf{O} = \frac{\partial \mathbf{M}}{\partial t} \quad (1.5.2)$$

The mass flow rate through an elemental area is  $\rho q_n A$  where  $q_n$  is the component of the mean seepage fluid velocity normal to the surface of an element of area A. Assuming that the volume is completely saturated with a single-phase, homogeneous fluid of density  $\rho$ , and the mean seepage velocity of the fluid and density are given at point P, the centroid of the control volume, then a Taylor series expansion about point P is used to obtain the net mass inflow to the elemental volume (Willis and Yeh, 1987). For example, the mass inflow in the  $x$  direction,  $I_x$ , is

$$I_x = \rho q_x \Delta y \Delta z - \frac{\partial}{\partial x}(\rho q_x) \frac{\Delta x}{2} \Delta y \Delta z \doteq \left[ \frac{M}{T} \right] \quad (1.5.3)$$

Similarly, the mass outflow in the  $x$  direction,  $O_x$ , is

$$O_x = \rho q_x \Delta y \Delta z + \frac{\partial}{\partial x}(\rho q_x) \frac{\Delta x}{2} \Delta y \Delta z \doteq \left[ \frac{M}{T} \right] \quad (1.5.4)$$

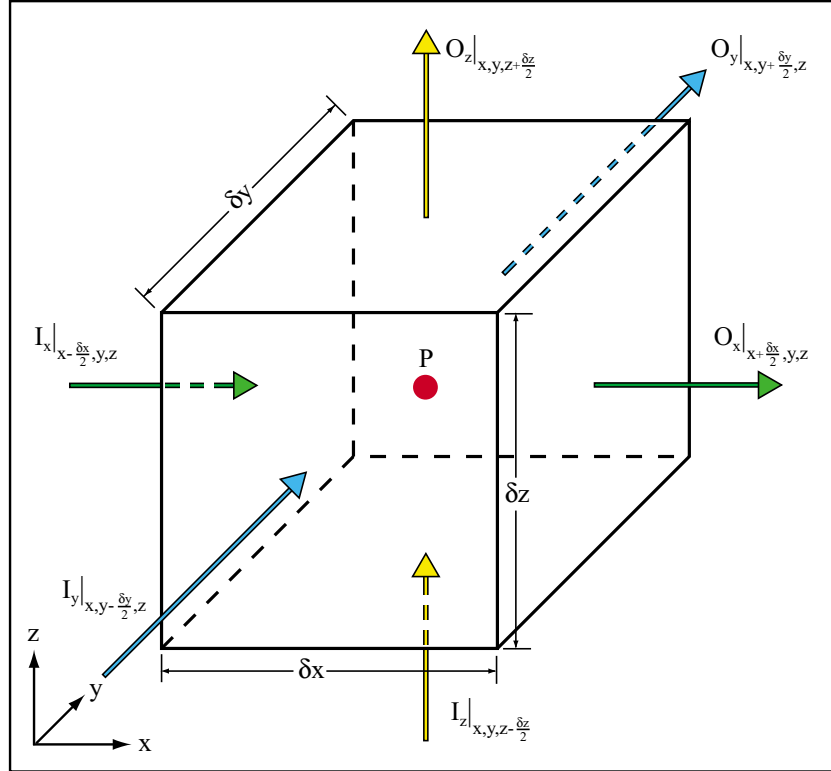


**Figure A.7:** Mass conservation for a control volume.

Summing the contributions to the inflow and outflow in the  $x$  direction gives,

$$\begin{aligned} I_x - O_x &= \rho q_x \Delta y \Delta z - \frac{\partial}{\partial x}(\rho q_x) \frac{\Delta x}{2} \Delta y \Delta z - \rho q_x \Delta y \Delta z - \frac{\partial}{\partial x}(\rho q_x) \frac{\Delta x}{2} \Delta y \Delta z \dots \\ \dots &= -\frac{\partial}{\partial x}(\rho q_x) \Delta x \Delta y \Delta z \end{aligned} \quad (1.5.5)$$

Summing the contributions to the inflow and outflow in the  $x,y,z$  directions, the net mass inflow is

$$\begin{aligned} \mathbf{I} - \mathbf{O} &= -\frac{\partial}{\partial x}(\rho q_x) \Delta x \Delta y \Delta z - \frac{\partial}{\partial y}(\rho q_y) \Delta x \Delta y \Delta z - \frac{\partial}{\partial z}(\rho q_z) \Delta x \Delta y \Delta z \\ \mathbf{I} - \mathbf{O} &= -\left[ \frac{\partial}{\partial x}(\rho q_x) + \frac{\partial}{\partial y}(\rho q_y) + \frac{\partial}{\partial z}(\rho q_z) \right] \Delta x \Delta y \Delta z \end{aligned} \quad (1.5.6)$$

or in vector notation,

$$\mathbf{I} - \mathbf{O} = (-\nabla \cdot \rho \mathbf{q}) \Delta x \Delta y \Delta z \quad (1.5.7)$$

where  $\nabla$  is the divergence operator,

$$\nabla = \frac{\partial}{\partial x} \hat{\mathbf{i}} + \frac{\partial}{\partial y} \hat{\mathbf{j}} + \frac{\partial}{\partial z} \hat{\mathbf{k}}$$

The net increase in the mass flow rate is equal to the rate of change of the mass stored within the elemental volume. The mass  $M$  of the fluid contained in the volume is

$$M = \epsilon S_w \rho \Delta x \Delta y \Delta z \equiv \left( \frac{V_{\text{void}}}{V_{\text{total}}} \frac{V_{\text{water}}}{V_{\text{void}}} \frac{\text{Mass}}{V_{\text{water}}} \right) \cdot V_{\text{total}} \equiv \text{Mass} \quad (1.5.8)$$

The time rate of change in mass storage is given as

$$\frac{\partial M}{\partial t} = \frac{\partial}{\partial t} (\epsilon S_w \rho) \Delta x \Delta y \Delta z \doteq \left[ \frac{M}{T} \right] \quad (1.5.9)$$

The continuity Equation (1.5.2) for the groundwater system is then expressed as,

$$(-\nabla \cdot \rho \mathbf{q}) \Delta x \Delta y \Delta z = \frac{\partial}{\partial t} (\epsilon S_w \rho) \Delta x \Delta y \Delta z \quad (1.5.10)$$

$$-\nabla \cdot \rho \mathbf{q} = \frac{\partial}{\partial t} (\epsilon S_w \rho) \quad (1.5.11)$$

Substituting  $\mathbf{q} = \epsilon S_w \mathbf{v}$  from Equation (1.3.13) gives

$$-\nabla \cdot (\epsilon S_w \rho \mathbf{v}) = \frac{\partial (\epsilon S_w \rho)}{\partial t} \quad (1.5.12)$$

A fluid mass source term,  $Q_p$ , is added to Equation (1.5.12) to account for external additions of fluid mass (e.g. a precipitation input).

$$\frac{\partial (\epsilon S_w \rho)}{\partial t} = -\nabla \cdot (\epsilon S_w \rho \mathbf{v}) + Q_p \quad (1.5.13)$$

where

$$Q_p \doteq \left[ \frac{M}{L^3 T} \right]$$

From Equation (1.2.8) the time rate of change in mass storage is defined as

$$\frac{\partial(\epsilon S_w \rho)}{\partial t} = \left( S_w \frac{\partial(\epsilon \rho)}{\partial p} + \epsilon \rho \frac{\partial(S_w)}{\partial p} \right) \frac{\partial p}{\partial t} = \left( S_w \rho S_{op} + \epsilon \rho \frac{\partial(S_w)}{\partial p} \right) \frac{\partial p}{\partial t} \quad (1.5.14)$$

which allows Equation (1.5.13) to be written as

$$\left( S_w \rho S_{op} + \epsilon \rho \frac{\partial(S_w)}{\partial p} \right) \frac{\partial p}{\partial t} = -\nabla \cdot (\epsilon S_w \rho \underline{v}) + Q_p \quad (1.5.15)$$

Substituting in the definition for average velocity,  $\underline{v}$ , Equation (1.5.15) becomes

$$\left( S_w \rho S_{op} + \epsilon \rho \frac{\partial(S_w)}{\partial p} \right) \frac{\partial p}{\partial t} = -\nabla \cdot \left( (\epsilon S_w \rho) \left[ \left( \frac{-\mathbf{k} k_r}{\epsilon S_w \mu} \right) \cdot (\nabla \mathbf{p} - \rho \underline{\mathbf{g}}) \right] \right) + Q_p \quad (1.5.16)$$

or

$$\left( S_w \rho S_{op} + \epsilon \rho \frac{\partial S_w}{\partial p} \right) \frac{\partial p}{\partial t} - \nabla \cdot \left[ \left( \frac{\mathbf{k} k_r \rho}{\mu} \right) \cdot (\nabla \mathbf{p} - \rho \underline{\mathbf{g}}) \right] = Q_p \quad (1.5.17)$$

## **APPENDIX B: Numerical Methods**

The model employs a two-dimensional hybrid finite-element and integrated-finite-difference method to approximate the governing equation that describes fluid density dependent saturated or unsaturated groundwater flow. The following sections review the numerical methods used by SUTRA. The numerical tools required for the approximation of the fluid mass balance are basis functions, coordinate transformations, and Gaussian integration.

### **2.1 Basis Functions:**

In a finite-element analysis, the dependent variables (e.g. pressure) are approximated by polynomial functions that are defined in terms of the unknown nodal values of the state or dependent variables. These approximating or interpolating functions vary over each element of the system, although continuity of the function is maintained along the element boundaries (Willis and Yeh, 1987). Linear basis functions are used by SUTRA to described the unknown nodal values over the system of two-dimensional quadrilateral elements.

Integration of linear basis functions is required within the model formulation. Basis functions are developed within a local coordinate system to facilitate the integration. Figure B.1 illustrates an element in both the global and local coordinate systems. The irregularly shaped element within the global coordinate system,  $(x, z)$ , is reduced to a square in the local coordinate system,  $(\eta, \xi)$ . Furthermore, the square in  $(\eta, \xi)$  has its corners (nodes) located at  $\eta = \pm 1, \xi = \pm 1$ . The relation between

the local and global coordinates is expressed as

$$x = \Omega_1^e x_1^e + \Omega_2^e x_2^e + \Omega_3^e x_3^e + \Omega_4^e x_4^e = \sum_{j=1}^4 \Omega_j^e x_j^e \quad (2.1.1)$$

$$z = \Omega_1^e z_1^e + \Omega_2^e z_2^e + \Omega_3^e z_3^e + \Omega_4^e z_4^e = \sum_{j=1}^4 \Omega_j^e z_j^e \quad (2.1.2)$$

where  $\Omega_j^e$  are some, as yet determined, functions of  $\eta$  and  $\xi$ . Both  $x_j^e$  and  $z_j^e$  are nodal coordinates within  $x$  and  $z$ . Adjacent elements must fit together so their sides must be uniquely determined by their common points. The quadrilateral element will have straight sides defined by a linear function.

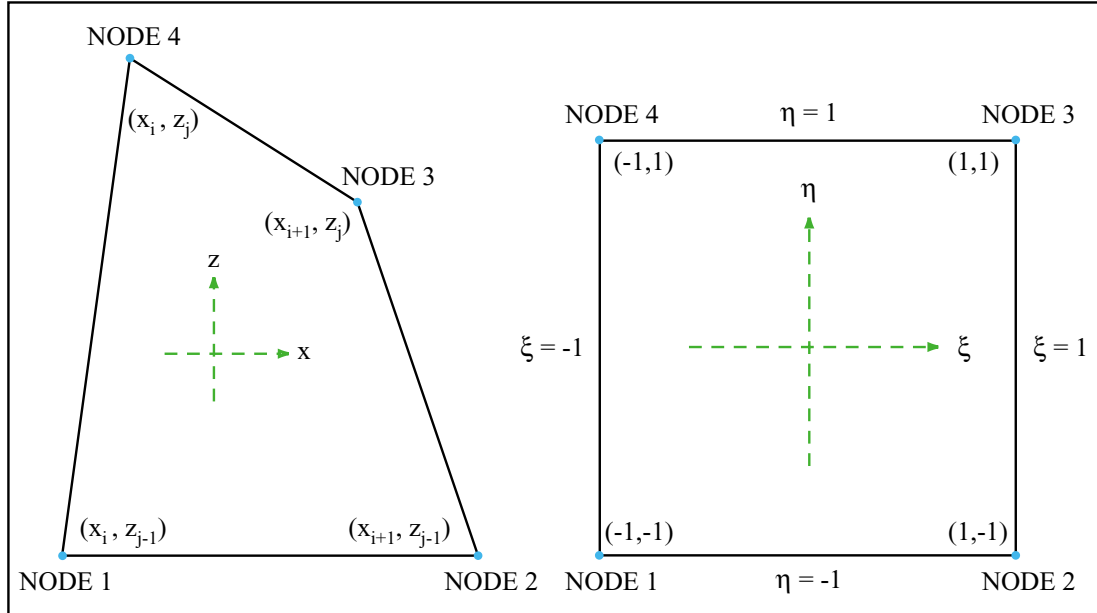


**Figure B.1:** A quadrilateral element in both global and local coordinate systems.

Values for  $\Omega_j^e$  that will provide the linear variation along element sides requires a polynomial of the form

$$x = a + b\xi + c\eta + d\xi\eta \quad (2.1.3)$$

which is linear in  $\xi$  when  $\eta = \pm 1$  and linear in  $\eta$  when  $\xi = \pm 1$ . We also have, from Figure B.1, the following conditions,

$$x = x_1 \quad \text{when } \xi = \eta = -1 \quad (2.1.4)$$

$$x = x_2 \quad \text{when } \xi = 1, \eta = -1$$

$$x = x_3 \quad \text{when } \xi = \eta = 1$$

$$x = x_4 \quad \text{when } \xi = -1, \eta = 1$$

Substituting these constraints into Equation (2.1.3) gives

$$\begin{Bmatrix} x_1 \\ x_2 \\ x_3 \\ x_4 \end{Bmatrix} = \begin{bmatrix} 1 & \xi_1 & \eta_1 & \xi_1\eta_1 \\ 1 & \xi_2 & \eta_2 & \xi_2\eta_2 \\ 1 & \xi_3 & \eta_3 & \xi_3\eta_1 \\ 1 & \xi_4 & \eta_4 & \xi_4\eta_4 \end{bmatrix} \begin{Bmatrix} a \\ b \\ c \\ d \end{Bmatrix} = \begin{bmatrix} 1 & -1 & -1 & 1 \\ 1 & 1 & -1 & -1 \\ 1 & 1 & 1 & 1 \\ 1 & -1 & 1 & -1 \end{bmatrix} \begin{Bmatrix} a \\ b \\ c \\ d \end{Bmatrix} \quad (2.1.5)$$

or, in vector-matrix notation

$$\mathbf{x} = [\mathbf{A}] \{\mathbf{P}\} \quad (2.1.6)$$

$$\mathbf{P} = [\mathbf{A}]^{-1} \{\mathbf{x}\} \quad (2.1.7)$$

where

$$[\mathbf{A}]^{-1} = \frac{1}{4} \begin{bmatrix} 1 & 1 & 1 & 1 \\ -1 & 1 & 1 & -1 \\ -1 & -1 & 1 & 1 \\ 1 & -1 & 1 & -1 \end{bmatrix} \quad (2.1.8)$$

Substituting  $\mathbf{P}$  into the matrix form of Equation (2.1.5) yields,

$$x = [1 \ \xi \ \eta \ \xi\eta] \begin{Bmatrix} a \\ b \\ c \\ d \end{Bmatrix} = [1 \ \xi \ \eta \ \xi\eta] \mathbf{P} = [1 \ \xi \ \eta \ \xi\eta] [\mathbf{A}]^{-1} \{\mathbf{x}\} \quad (2.1.9)$$

A comparison of Equation (2.1.1) and (2.1.9) reveals,

$$x = \{\Omega^e\}^T \{\mathbf{x}^e\} = [1 \ \xi \ \eta \ \xi\eta] [\mathbf{A}]^{-1} \{\mathbf{x}\} \quad (2.1.10)$$

or

$$\begin{aligned} \{\Omega^e\}^T &= [1 \ \xi \ \eta \ \xi\eta] [\mathbf{A}]^{-1} \\ \begin{bmatrix} \Omega_1 \\ \Omega_2 \\ \Omega_3 \\ \Omega_4 \end{bmatrix} &= [1 \ \xi \ \eta \ \xi\eta] \cdot \frac{1}{4} \begin{bmatrix} 1 & -1 & -1 & 1 \\ 1 & 1 & -1 & -1 \\ 1 & 1 & 1 & 1 \\ 1 & -1 & 1 & -1 \end{bmatrix} \end{aligned} \quad (2.1.11)$$

where

$$\Omega_1 = \frac{1}{4}(1 - \xi - \eta + \xi\eta) = \frac{1}{4}(1 - \xi)(1 - \eta) \quad (2.1.12)$$

$$\Omega_2 = \frac{1}{4}(1 + \xi - \eta - \xi\eta) = \frac{1}{4}(1 + \xi)(1 - \eta) \quad (2.1.13)$$

$$\Omega_3 = \frac{1}{4}(1 + \xi + \eta + \xi\eta) = \frac{1}{4}(1 + \xi)(1 + \eta) \quad (2.1.14)$$

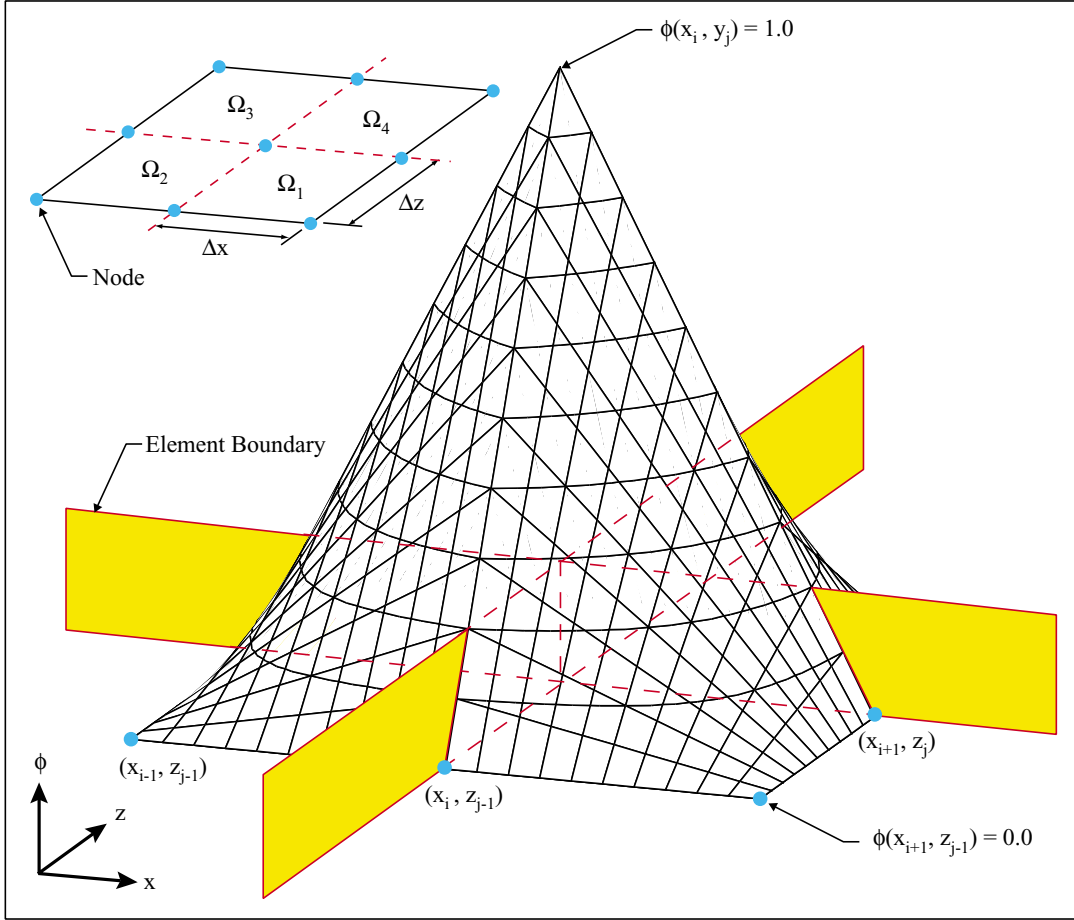
$$\Omega_4 = \frac{1}{4}(1 - \xi + \eta - \xi\eta) = \frac{1}{4}(1 - \xi)(1 + \eta) \quad (2.1.15)$$

Figure B.2 illustrates the basis function defined over a four element local space. Nodes are described with global coordinates to help facilitate the connection between local and global coordinate systems. The basis function within the local coordinate system is given as  $\Omega^e(\xi_i, \eta_j)$ , while  $\phi(x_i, y_j)$  is given for the basis function within the global coordinate system. One basis function is defined for each node.

Figure B.3 illustrates multiple perspectives of the basis function,  $\Omega_j$ , defined for node  $j$ . The basis function has a value of one at node  $j$  and a value of zero at all other nodes. The surface representing  $\Omega_j$  over an element is curved due to the product of  $\xi$  and  $\eta$  in Equation (2.1.11).

The derivatives of the bi-linear basis functions which depend on only one space coordinate are given as:

$$\frac{\partial \Omega_1}{\partial \xi} = \frac{\partial}{\partial \xi} \left[ \frac{1}{4} - \frac{\xi}{4} - \frac{\eta}{4} + \frac{\xi\eta}{4} \right] = -\frac{1}{4} + \frac{\eta}{4} = -\frac{1}{4}(1 - \eta) \quad (2.1.16)$$



**Figure B.2:** Basis function defined for quadrilateral elements. Note above function for central node spans four elements.

$$\frac{\partial \Omega_2}{\partial \xi} = \frac{\partial}{\partial \xi} \left[ \frac{1}{4} + \frac{\xi}{4} - \frac{\eta}{4} - \frac{\xi\eta}{4} \right] = \frac{1}{4} - \frac{\eta}{4} = \frac{1}{4}(1 - \eta) \quad (2.1.17)$$

$$\frac{\partial \Omega_3}{\partial \xi} = \frac{\partial}{\partial \xi} \left[ \frac{1}{4} + \frac{\xi}{4} + \frac{\eta}{4} + \frac{\xi\eta}{4} \right] = \frac{1}{4} + \frac{\eta}{4} = \frac{1}{4}(1 + \eta) \quad (2.1.18)$$

$$\frac{\partial \Omega_4}{\partial \xi} = \frac{\partial}{\partial \xi} \left[ \frac{1}{4} - \frac{\xi}{4} + \frac{\eta}{4} - \frac{\xi\eta}{4} \right] = -\frac{1}{4} - \frac{\eta}{4} = -\frac{1}{4}(1 + \eta) \quad (2.1.19)$$

and

$$\frac{\partial \Omega_1}{\partial \eta} = \frac{\partial}{\partial \eta} \left[ \frac{1}{4} - \frac{\xi}{4} - \frac{\eta}{4} + \frac{\xi\eta}{4} \right] = -\frac{1}{4} + \frac{\xi}{4} = -\frac{1}{4}(1 - \xi) \quad (2.1.20)$$

$$\frac{\partial \Omega_2}{\partial \eta} = \frac{\partial}{\partial \eta} \left[ \frac{1}{4} + \frac{\xi}{4} - \frac{\eta}{4} - \frac{\xi\eta}{4} \right] = -\frac{1}{4} - \frac{\xi}{4} = -\frac{1}{4}(1 + \xi) \quad (2.1.21)$$

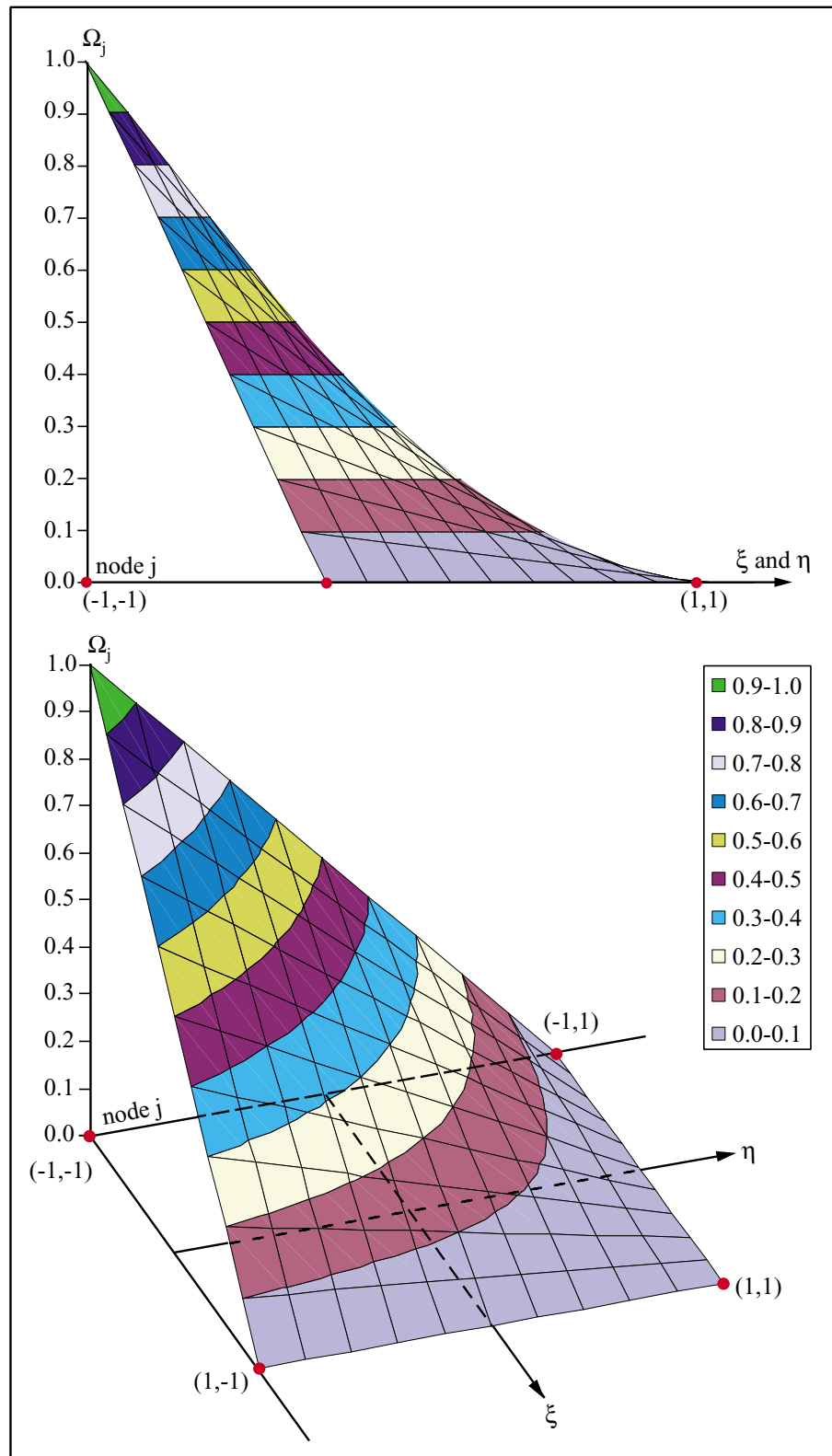


**Figure B.3:** Perspectives of basis function  $\Omega_j(\xi, \eta)$  at node  $j$ .

$$\frac{\partial \Omega_3}{\partial \eta} = \frac{\partial}{\partial \eta} \left[ \frac{1}{4} + \frac{\xi}{4} + \frac{\eta}{4} + \frac{\xi \eta}{4} \right] = \frac{1}{4} + \frac{\xi}{4} = \frac{1}{4}(1 + \xi) \quad (2.1.22)$$

$$\frac{\partial \Omega_4}{\partial \eta} = \frac{\partial}{\partial \eta} \left[ \frac{1}{4} - \frac{\xi}{4} + \frac{\eta}{4} - \frac{\xi \eta}{4} \right] = \frac{1}{4} - \frac{\xi}{4} = \frac{1}{4}(1 - \xi) \quad (2.1.23)$$

## 2.2 Coordinate Transformations:

Coordinate transformation between local,  $(\xi, \eta)$ , and global,  $(x, z)$ , coordinate systems is required for the finite-element mesh calculations and integral evaluations. The transformation involves a linear remapping in each coordinate direction and employs the basis functions,  $\Omega_j$ , to provide mapping. The ability to map from one coordinate system to another is based on the chain rule of differentiation. For functions of two variables, we have,

$$\frac{\partial \Omega_j}{\partial \xi} = \frac{\partial \Omega_j}{\partial x} \frac{\partial x}{\partial \xi} + \frac{\partial \Omega_j}{\partial z} \frac{\partial z}{\partial \xi} \quad (2.2.1)$$

$$\frac{\partial \Omega_j}{\partial \eta} = \frac{\partial \Omega_j}{\partial x} \frac{\partial x}{\partial \eta} + \frac{\partial \Omega_j}{\partial z} \frac{\partial z}{\partial \eta} \quad (2.2.2)$$

In matrix notation, equations (2.2.1) and (2.2.2) are combined to give transformations for both directions local to global and global to local.

$$\begin{Bmatrix} \frac{\partial \Omega_j}{\partial \xi} \\ \frac{\partial \Omega_j}{\partial \eta} \end{Bmatrix} = \begin{bmatrix} \frac{\partial x}{\partial \xi} & \frac{\partial z}{\partial \xi} \\ \frac{\partial x}{\partial \eta} & \frac{\partial z}{\partial \eta} \end{bmatrix} \begin{Bmatrix} \frac{\partial \Omega_j}{\partial x} \\ \frac{\partial \Omega_j}{\partial z} \end{Bmatrix} = \mathbf{J} \begin{Bmatrix} \frac{\partial \Omega_j}{\partial x} \\ \frac{\partial \Omega_j}{\partial z} \end{Bmatrix} \quad (2.2.3)$$

and

$$\begin{Bmatrix} \frac{\partial \Omega_j}{\partial x} \\ \frac{\partial \Omega_j}{\partial z} \end{Bmatrix} = \begin{bmatrix} \frac{\partial x}{\partial \xi} & \frac{\partial z}{\partial \xi} \\ \frac{\partial x}{\partial \eta} & \frac{\partial z}{\partial \eta} \end{bmatrix}^{-1} \begin{Bmatrix} \frac{\partial \Omega_j}{\partial \xi} \\ \frac{\partial \Omega_j}{\partial \eta} \end{Bmatrix} = \mathbf{J}^{-1} \begin{Bmatrix} \frac{\partial \Omega_j}{\partial \xi} \\ \frac{\partial \Omega_j}{\partial \eta} \end{Bmatrix} \quad (2.2.4)$$

where

$$\mathbf{J} = \begin{bmatrix} J_{11} & J_{12} \\ J_{21} & J_{22} \end{bmatrix} = \begin{bmatrix} \frac{\partial x}{\partial \xi} & \frac{\partial z}{\partial \xi} \\ \frac{\partial x}{\partial \eta} & \frac{\partial z}{\partial \eta} \end{bmatrix} \quad (2.2.5)$$

$$\begin{aligned} \mathbf{J}^{-1} &= \left( \frac{1}{\det \mathbf{J}} \right) \begin{bmatrix} J_{22} & -J_{12} \\ -J_{21} & J_{11} \end{bmatrix} = \left( \frac{1}{J_{11}J_{22} - J_{12}J_{21}} \right) \begin{bmatrix} J_{22} & -J_{12} \\ -J_{21} & J_{11} \end{bmatrix} \dots \\ \dots &= \left( \frac{1}{\frac{\partial x}{\partial \xi} \frac{\partial z}{\partial \eta} - \frac{\partial z}{\partial \xi} \frac{\partial x}{\partial \eta}} \right) \begin{bmatrix} \frac{\partial z}{\partial \eta} & -\frac{\partial z}{\partial \xi} \\ -\frac{\partial x}{\partial \eta} & \frac{\partial x}{\partial \xi} \end{bmatrix} \end{aligned} \quad (2.2.6)$$

The partial derivative terms within the Jacobian Matrix, J, are obtained from the differentiation of  $x$ , Equation (2.1.1), and  $z$ , Equation (2.1.2), with respect to the local coordinates  $(\xi, \eta)$ .

$$\frac{\partial x}{\partial \xi} = \frac{\partial(\Omega_1^e x_1^e)}{\partial \xi} + \frac{\partial(\Omega_2^e x_2^e)}{\partial \xi} + \frac{\partial(\Omega_3^e x_3^e)}{\partial \xi} + \frac{\partial(\Omega_4^e x_4^e)}{\partial \xi} \quad (2.2.7)$$

$$\frac{\partial x}{\partial \eta} = \frac{\partial(\Omega_1^e x_1^e)}{\partial \eta} + \frac{\partial(\Omega_2^e x_2^e)}{\partial \eta} + \frac{\partial(\Omega_3^e x_3^e)}{\partial \eta} + \frac{\partial(\Omega_4^e x_4^e)}{\partial \eta} \quad (2.2.8)$$

$$\frac{\partial z}{\partial \xi} = \frac{\partial(\Omega_1^e z_1^e)}{\partial \xi} + \frac{\partial(\Omega_2^e z_2^e)}{\partial \xi} + \frac{\partial(\Omega_3^e z_3^e)}{\partial \xi} + \frac{\partial(\Omega_4^e z_4^e)}{\partial \xi} \quad (2.2.9)$$

$$\frac{\partial z}{\partial \eta} = \frac{\partial(\Omega_1^e z_1^e)}{\partial \eta} + \frac{\partial(\Omega_2^e z_2^e)}{\partial \eta} + \frac{\partial(\Omega_3^e z_3^e)}{\partial \eta} + \frac{\partial(\Omega_4^e z_4^e)}{\partial \eta} \quad (2.2.10)$$

or in matrix notation,

$$J = \begin{bmatrix} \frac{\partial x}{\partial \xi} & \frac{\partial z}{\partial \xi} \\ \frac{\partial x}{\partial \eta} & \frac{\partial z}{\partial \eta} \end{bmatrix} = \begin{bmatrix} \frac{\partial \Omega_1}{\partial \xi} & \frac{\partial \Omega_2}{\partial \xi} & \frac{\partial \Omega_3}{\partial \xi} & \frac{\partial \Omega_4}{\partial \xi} \\ \frac{\partial \Omega_1}{\partial \eta} & \frac{\partial \Omega_2}{\partial \eta} & \frac{\partial \Omega_3}{\partial \eta} & \frac{\partial \Omega_4}{\partial \eta} \end{bmatrix} \begin{bmatrix} x_1 & z_1 \\ x_2 & z_2 \\ x_3 & z_3 \\ x_4 & z_4 \end{bmatrix} \quad (2.2.11)$$

Further development of the Jacobian terms gives

$$\begin{aligned} \frac{\partial x}{\partial \xi} &= -\frac{1}{4}(1-\eta)x_1 + \frac{1}{4}(1-\eta)x_2 + \frac{1}{4}(1+\eta)x_3 - \frac{1}{4}(1+\eta)x_4 \quad \dots \\ \dots &= \frac{1}{4}[(x_2 - x_1)(1-\eta) + (x_3 - x_4)(1+\eta)] \end{aligned} \quad (2.2.12)$$

$$\begin{aligned} \frac{\partial x}{\partial \eta} &= -\frac{1}{4}(1-\xi)x_1 - \frac{1}{4}(1+\xi)x_2 + \frac{1}{4}(1+\xi)x_3 + \frac{1}{4}(1-\xi)x_4 \quad \dots \\ \dots &= \frac{1}{4}[(x_4 - x_1)(1-\xi) + (x_3 - x_2)(1+\xi)] \end{aligned} \quad (2.2.13)$$

$$\begin{aligned} \frac{\partial z}{\partial \xi} &= -\frac{1}{4}(1-\eta)z_1 + \frac{1}{4}(1-\eta)z_2 + \frac{1}{4}(1+\eta)z_3 - \frac{1}{4}(1+\eta)z_4 \quad \dots \\ \dots &= \frac{1}{4}[(z_2 - z_1)(1-\eta) + (z_3 - z_4)(1+\eta)] \end{aligned} \quad (2.2.14)$$

$$\begin{aligned} \frac{\partial z}{\partial \eta} &= -\frac{1}{4}(1-\xi)z_1 - \frac{1}{4}(1+\xi)z_2 + \frac{1}{4}(1+\xi)z_3 + \frac{1}{4}(1-\xi)z_4 \quad \dots \\ \dots &= \frac{1}{4}[(z_4 - z_1)(1-\xi) + (z_3 - z_2)(1+\xi)] \end{aligned} \quad (2.2.15)$$

In addition to transforming the derivatives from  $(x, z)$  to  $(\xi, \eta)$ , the area of the element is changed using

$$d\mathbf{A} = dx dz = (\det J) d\xi d\eta \quad (2.2.16)$$

Integrating over each element within the local coordinate system gives

$$\mathbf{A} = \int d\mathbf{A} = \int_z \int_x dx dz = \int_{-1}^1 \int_{-1}^1 (\det J) d\xi d\eta \quad (2.2.17)$$

### 2.3 Gaussian Integration:

Gaussian quadrature is a technique for solving the exact integration of polynomials through the summation of the integrands' point values. Integration is performed by replacing a definite integral with a finite series. The symbolic form of Gaussian integration is,

$$\int_{\Psi=-1}^{\Psi=1} f(\Psi) d\Psi = \sum_{gp=1}^{np} H_{gp} f(\Psi_{gp}) \quad (2.3.1)$$

where  $f(\Psi)$  is the function to be integrated between  $\Psi = -1$  to  $\Psi = +1$ ,  $gp$  is the Gauss point number,  $np$  is the total number of Gauss points, and  $H_{gp}$  are the weighting coefficients.

In order to integrate a term of the differential governing equation,  $f(x, z)$ , over an arbitrary quadrilateral element, the limits of the integral must first be transformed to local coordinate values of  $-1$  to  $+1$ .

$$\int_z \int_x f(x, z) dx dz = \int_\eta \int_\xi f(\xi, \eta) (\det J) d\xi d\eta = \int_{-1}^1 \int_{-1}^1 \tilde{f}(\xi, \eta) d\xi d\eta \quad (2.3.2)$$

Gaussian integration is applied independently to each integral with two Gauss points required for each coordinate direction. The Gauss point values for numbers one and two are  $-3^{\frac{1}{2}}$  and  $+3^{\frac{1}{2}}$  respectively.

$$\int_z \int_x f(x, z) dx dz = \int_{-1}^1 \left[ \sum_{i=1}^2 \tilde{f}(\xi_i, \eta) \right] d\eta = \sum_{j=1}^2 \sum_{i=1}^2 \tilde{f}(\xi_i, \eta_j) \quad (2.3.3)$$

Identical limits of integration for the two integrals allows for a single summation of Equation (2.3.3).

$$\int_z \int_x f(x, z) dx dz = \sum_{gp=1}^4 \tilde{f}(\xi_{gp}, \eta_{gp}) \quad (2.3.4)$$

where each of the four Gauss point values are shown in Figure B.4.

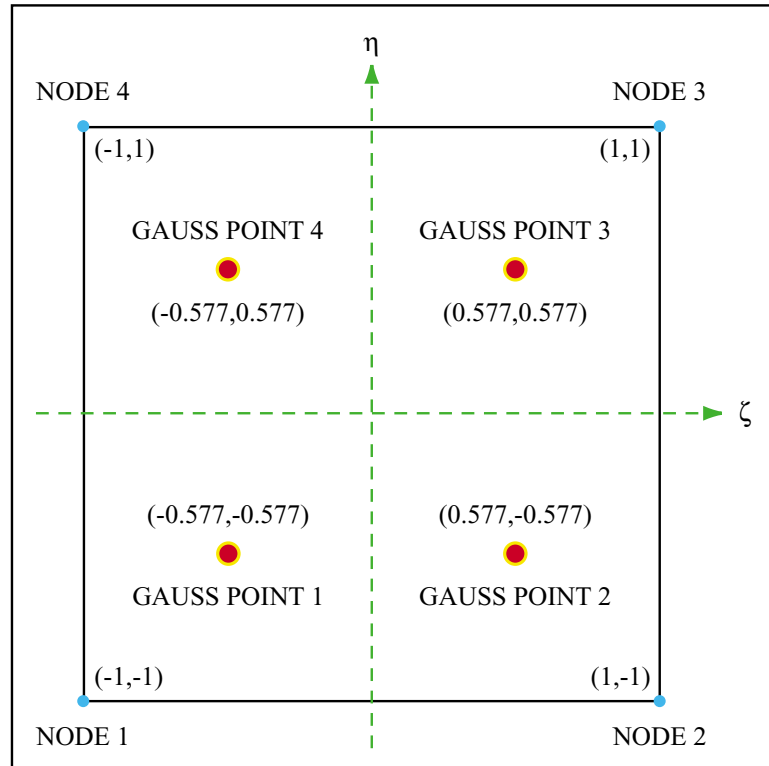


**Figure B.4:** Finite element in local coordinate system with Gauss points.

Example:

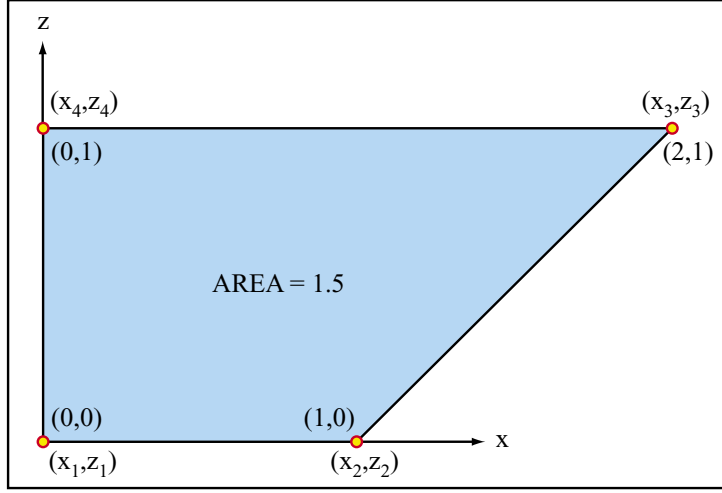


**Figure B.5:** Geometry of example cell  $i$ .

Consider a cell  $i$  whose corner nodes are described in Figure B.5. Show that over the given element, the volumetric integral of a single basis function is equal to the element's area,  $A = 1.5$ :

It can be shown that the volume of a cell  $i$  is expressed as,

$$\forall_i = \int_z \int_y \int_x \phi_i(x, z) dx dy dz = \int_z \int_x \phi_i B(x, z) dx dz \quad (2.3.5)$$

A uniform unit thickness,  $B = 1$ , reduces the elemental volume to an area,  $A$ .

$$A = \int_z \int_x \phi_i dx dz \quad (2.3.6)$$

Transformation of the double integral from global to local coordinate systems gives,

$$\begin{aligned} A &= \int_{\eta} \int_{\xi} \boldsymbol{\Omega}_i(\xi, \eta) (\det J) d\xi d\eta = \int_{-1}^1 \int_{-1}^1 \boldsymbol{\Omega}_i(\det J) d\xi d\eta \quad \dots \\ \dots &= \sum_{gp=1}^4 \boldsymbol{\Omega}_{i, gp} (\det J_{gp}) = \sum_{gp=1}^4 [\Omega_{1, gp} + \Omega_{2, gp} + \Omega_{3, gp} + \Omega_{4, gp}] (\det J_{gp}) \quad \dots \end{aligned}$$

$$\begin{aligned}
& \cdots = (\Omega_{1,1} + \Omega_{1,2} + \Omega_{1,3} + \Omega_{1,4})(\det J_1) \cdots \\
& \cdots + (\Omega_{2,1} + \Omega_{2,2} + \Omega_{2,3} + \Omega_{2,4})(\det J_2) \cdots \\
& \cdots + (\Omega_{3,1} + \Omega_{3,2} + \Omega_{3,3} + \Omega_{3,4})(\det J_3) \cdots \\
& \cdots + (\Omega_{4,1} + \Omega_{4,2} + \Omega_{4,3} + \Omega_{4,4})(\det J_4)
\end{aligned} \tag{2.3.7}$$

Using equations (2.1.12 – 2.1.16), the basis functions for the given element are given as

$$\Omega_{1,1} = \Omega_1(-0.577, -0.577) = 0.622 \quad \Omega_{3,1} = \Omega_3(-0.577, -0.577) = 0.045$$

$$\Omega_{1,2} = \Omega_1(-0.577, -0.577) = 0.167 \quad \Omega_{3,2} = \Omega_3(-0.577, -0.577) = 0.167$$

$$\Omega_{1,3} = \Omega_1(-0.577, 0.577) = 0.045 \quad \Omega_{3,3} = \Omega_3(-0.577, 0.577) = 0.622$$

$$\Omega_{1,4} = \Omega_1(-0.577, 0.577) = 0.167 \quad \Omega_{3,4} = \Omega_3(-0.577, 0.577) = 0.167$$

$$\Omega_{2,1} = \Omega_2(-0.577, -0.577) = 0.167 \quad \Omega_{4,1} = \Omega_4(-0.577, -0.577) = 0.167$$

$$\Omega_{2,2} = \Omega_2(-0.577, -0.577) = 0.622 \quad \Omega_{4,2} = \Omega_4(-0.577, -0.577) = 0.045$$

$$\Omega_{2,3} = \Omega_2(-0.577, 0.577) = 0.167 \quad \Omega_{4,3} = \Omega_4(-0.577, 0.577) = 0.167$$

$$\Omega_{2,4} = \Omega_2(-0.577, 0.577) = 0.045 \quad \Omega_{4,4} = \Omega_4(-0.577, 0.577) = 0.622$$

The determinate of the Jacobian matrix (Equation 2.2.5) is given for each Gauss point.

$$\det J_1 = (0.606)(0.05) - (0)(0.105) = 0.303$$

$$\det J_2 = (0.606)(0.05) - (0)(0.394) = 0.303$$

$$\det J_3 = (0.894)(0.05) - (0)(0.394) = 0.447$$

$$\det J_4 = (0.894)(0.05) - (0)(0.394) = 0.447$$

Evaluation of Equation (2.3.7), produces the element's exact area.

$$\begin{aligned} A &= (0.622 + 0.167 + 0.045 + 0.167)0.303 \quad \dots \\ &\quad \dots + (0.167 + 0.622 + 0.167 + 0.045)0.303 \quad \dots \\ &\quad \dots + (0.045 + 0.167 + 0.622 + 0.167)0.447 \quad \dots \\ &\quad \dots + (0.167 + 0.045 + 0.167 + 0.622)0.447 \\ A &= (1)0.303 + (1)0.303 + (1)0.447 + (1)0.447 = 1.5 \end{aligned}$$

or  $\forall_i = 1.5$ , considering a unit depth of thickness. There are four basis functions within an element, one  $\Omega_i$  for each of the element nodes. At any location within an element, the sum of four basis functions will always equal one. For example:

$$\Omega_{1,1} + \Omega_{2,1} + \Omega_{3,1} + \Omega_{4,1} = 0.622 + 0.167 + 0.045 + 0.167 = 1$$

## 2.4 Numerical Approximation of Fluid Mass Balance:

Groundwater flow is simulated through the numerical solution of the fluid mass balance Equation (1.5.17). The governing equation representing the SUTRA fluid mass balance,  $O_p(p) = 0$ , is

$$O_p(p) = \left( S_w \rho S_{op} + \epsilon \rho \frac{\partial S_w}{\partial p} \right) \frac{\partial p}{\partial t} - \nabla \cdot \left[ \left( \frac{\mathbf{k} k_r \rho}{\mu} \right) \cdot (\nabla p - \rho \mathbf{g}) \right] - Q_p = 0 \quad (2.4.1)$$

where  $S_w$  is the water saturation;  $\rho$  is the fluid density;  $S_{op}$  is the specific pressure storativity;  $\epsilon$  is the porosity;  $p$  is the fluid pressure;  $t$  is time;  $\mathbf{k}$  is the solid matrix

permeability;  $k_r$  is the relative permeability to fluid flow;  $\mu$  is the fluid viscosity;  $\mathbf{g}$  is the gravitational acceleration; and  $Q_p$  is the fluid mass source.

An additional source term is added to the mass balance Equation (2.4.1) to account for externally specified pressure boundary conditions,  $p_{BC}$ .

$$\begin{aligned} O_p(p) = & \left( S_w \rho S_{op} + \epsilon \rho \frac{\partial S_w}{\partial p} \right) \frac{\partial p}{\partial t} - \nabla \cdot \left[ \left( \frac{\mathbf{k} k_r \rho}{\mu} \right) \cdot (\nabla p - \rho \mathbf{g}) \right] \dots \\ & \dots - Q_p - \nu_p (p_{BC} - p) = 0 \end{aligned} \quad (2.4.2)$$

where  $\nu_p$  is the average medium conductance. Conductance is related to the cross-sections of the elementary channels through which the flow takes place. When conductance is set sufficiently large, the weight of the pressure boundary term becomes larger than the other terms within Equation (2.4.2).  $O_p(p) = 0$  is maintained with an excessive source term which requires  $p_{BC} \cong p$ . By forcing  $p_{BC} = p$ , the desired boundary condition is satisfied.

### Spatial Integration

The fluid mass balance equation,  $O_p(p)$ , is approximated through nodewise, elementwise, and cellwise discretizations, Figure B.6. Spatial discretization of the domain results in the inexact representation of variables and their derivatives. The approximate equation,  $\widehat{O_p(p)}$ , equals a spatially varying residual value,  $R_p(x, z, t)$ , which is no longer equal to zero.

$$\widehat{O_p(p)} = R_p(x, z, t) \neq 0 \quad (2.4.3)$$

By minimizing the residual over space and time, Equation (2.4.3) is reformulated as an optimization problem. The objective of the optimization is to determine the

nodal values of  $\hat{p}_i$ , in such a way as to minimize the residual,  $R_p(x, z, t)$ . The residual is minimized by requiring the orthogonality of the weighting functions and the differential. The weighted residual formulation is written as:

$$\int_{\mathbb{V}} R_p(x, z, t) W_i(x, z) d\mathbb{V} = \int_{\mathbb{V}} \widehat{O_p(p)} W_i(x, z) d\mathbb{V} = 0 \quad i = \overline{1, \text{NN}} \quad (2.4.4)$$

where  $W_i(x, z)$  is the weighting function in global coordinates;  $\mathbb{V}$  is the total spatial volume of the groundwater system; and NN is the total number of nodes within the finite element mesh.

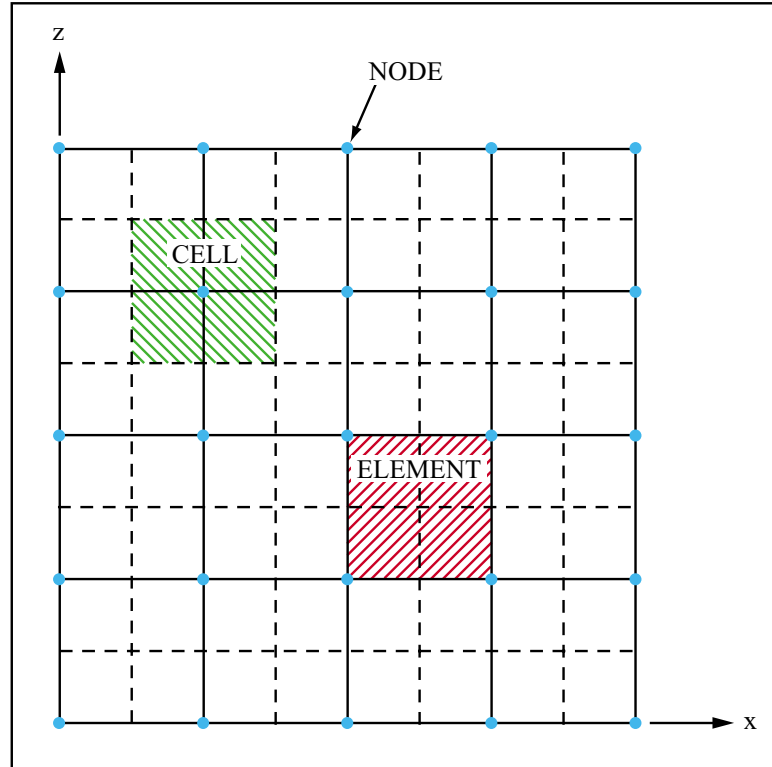


**Figure B.6:** Cells, elements and nodes for a two-dimensional finite-element mesh composed of quadrilateral elements.

The Galerkin method of weighted residuals is applied, since the basis function,  $\phi_i(x, z)$ , is equal to the weighting function,  $W_i(x, z)$ . Substituting  $\phi_i(x, z)$  into

Equation (2.4.4) yields

$$\int_{\forall} \widehat{\widehat{O_p(p)}} \phi_i(x, z) d\forall = 0 \quad (2.4.5)$$

Substitution for  $\widehat{\widehat{O_p(p)}}$  from Equation (2.4.2) gives,

$$\begin{aligned} & \int_{\forall} \left\{ \left( S_w \rho S_{op} + \epsilon \rho \frac{\partial S_w}{\partial p} \right) \frac{\partial p}{\partial t} - \nabla \cdot \left[ \left( \frac{\mathbf{k} k_r \rho}{\mu} \right) \cdot (\nabla p - \rho \mathbf{g}) \right] \right. \dots \\ & \left. \dots - Q_p - \nu_p \left( p_{BC} - p \right) \right\} \phi_i(x, z) d\forall = 0 \end{aligned} \quad (2.4.6)$$

or

$$\begin{aligned} & \int_{\forall} \left[ \left( S_w \rho S_{op} + \epsilon \rho \frac{\partial S_w}{\partial p} \right) \frac{\partial p}{\partial t} \right] \phi_i(x, z) d\forall \dots \\ & \dots - \int_{\forall} \left[ \nabla \cdot \left\{ \left( \frac{\mathbf{k} k_r \rho}{\mu} \right) \cdot (\nabla p - \rho \mathbf{g}) \right\} \right] \phi_i(x, z) d\forall \dots \\ & \dots - \int_{\forall} [Q_p] \phi_i(x, z) d\forall - \int_{\forall} \left[ \nu_p \left( p_{BC} - p \right) \right] \phi_i(x, z) d\forall = 0 \end{aligned} \quad (2.4.7)$$

The first term in Equation (2.4.7) is an integral of the pressure derivative,

$$\begin{aligned} & \int_{\forall} \left[ \left( S_w \rho S_{op} + \epsilon \rho \frac{\partial S_w}{\partial p} \right) \frac{\partial p}{\partial t} \right] \phi_i(x, z) d\forall \dots \\ & \dots = \left[ \left( S_w \rho S_{op} + \epsilon \rho \frac{\partial S_w}{\partial p} \right) \frac{\partial p}{\partial t} \right] \int_{\forall} \phi_i(x, z) d\forall \end{aligned} \quad (2.4.8)$$

where the term in brackets is discretized cellwise. From the Gaussian Integration example, Equation (2.3.5), the integral of the basis function equals the volume of the cell at node  $i$ . Integrating term (2.4.8) gives,

$$\left( S_w \rho S_{op} + \epsilon \rho \frac{\partial S_w}{\partial p} \right)_i \frac{\partial p_i}{\partial t} \forall_i \quad (2.4.9)$$

Green's Theorem is applied to the second term in Equation (2.4.7). The symbolic form of Green's Theorem is given as,

$$\int_{\forall} (\nabla \cdot \Psi) \Upsilon d\forall = \int_{\Gamma} (\Psi \cdot \mathbf{n}) \Upsilon d\Gamma - \int_{\forall} (\Psi \nabla \Upsilon) d\forall \quad (2.4.10)$$

Application of Green's Theorem to the second term yields,

$$\begin{aligned}
 & - \int_{\mathbb{V}} \left( \nabla \cdot \left[ \left( \frac{\mathbf{k} k_r \rho}{\mu} \right) \widehat{\cdot} (\nabla p - \rho \mathbf{g}) \right] \right) \phi_i(x, z) d\mathbb{V} = \dots \\
 & \dots - \int_{\Gamma} \left[ \left( \frac{\mathbf{k} k_r \rho}{\mu} \right) \widehat{\cdot} (\nabla p - \rho \mathbf{g}) \right] \cdot \mathbf{n} \phi_i(x, z) d_{\Gamma} \dots \\
 & \dots + \int_{\mathbb{V}} \left[ \left( \frac{\mathbf{k} k_r \rho}{\mu} \right) \widehat{\cdot} (\nabla p - \rho \mathbf{g}) \right] \cdot \nabla \phi_i d\mathbb{V} \tag{2.4.11}
 \end{aligned}$$

where  $\mathbf{n}$  is the unit vector normal to the three-dimensional surface bounding the region to be simulated, and  $\Gamma$  is the surface of the region. The basis function in global coordinates is denoted,  $\phi_i(x, z)$ . The first term on the right of Equation (2.4.11) is exactly the fluid mass outflow,  $\mathbf{O}_i(t)$ , across the region's boundary at node  $i$ .

$$\begin{aligned}
 \mathbf{O}_i(t) &= -\mathbf{q} \rho A = -\epsilon S_w \mathbf{v} \rho A \dots \\
 \dots &= -\epsilon S_w \left[ \left( \frac{\mathbf{k} k_r}{\epsilon S_w \mu} \right) \cdot (\nabla p - \rho \mathbf{g}) \right] \rho A = -\left( \frac{\mathbf{k} k_r \rho}{\mu} \right) \cdot (\nabla p - \rho \mathbf{g}) A \\
 \mathbf{O}_i(t) &= - \int_{\Gamma} \left[ \left( \frac{\mathbf{k} k_r \rho}{\mu} \right) \widehat{\cdot} (\nabla p - \rho \mathbf{g}) \right] \cdot \mathbf{n} \phi_i(x, z) d_{\Gamma} \tag{2.4.12}
 \end{aligned}$$

This term is used to specify fluid flows across system boundaries.

The second term on the right of Equation (2.4.11) is approximated using a combination of elementwise and nodewise discretizations. The permeability tensor,  $\mathbf{k}$ , is expressed in matrix notation as,

$$\hat{\mathbf{k}}^L = \begin{bmatrix} k_{xx}^L & k_{xy}^L & k_{xz}^L \\ k_{yx}^L & k_{yy}^L & k_{yz}^L \\ k_{zx}^L & k_{zy}^L & k_{zz}^L \end{bmatrix} \tag{2.4.13}$$

where the discretization of  $\mathbf{k}$  is elementwise and is indicated by  $\hat{\mathbf{k}}^L$ . A simplification of the permeability tensor is made with the assumption of a two-dimensional model.

Within the third dimension, or  $y$  coordinate direction, the  $k_{xy}$ ,  $k_{yx}$ ,  $k_{yy}$ ,  $k_{yz}$ , and  $k_{zy}$  components of the permeability tensor are eliminated.

$$\hat{\mathbf{k}}^L = \begin{bmatrix} k_{xx}^L & k_{xz}^L \\ k_{zx}^L & k_{zz}^L \end{bmatrix} \quad (2.4.4)$$

The finite approximation of fluid pressure is discretized nodewise:

$$p(x, z, t) \cong \sum_{i=1}^{NN} p_i(t) \phi_i(x, z) \quad (2.4.15)$$

where NN is the total number of nodes in the mesh. Integration of the pressure derivative over the total spatial volume gives,

$$\int_V \nabla p dV = \sum_{i=1}^{NN} \int_V \nabla [p_i(t) \cdot \phi_i(x, z)] dV = \sum_{i=1}^{NN} p_i(t) \int_V \nabla \phi_i(x, z) dV \quad (2.4.16)$$

Relative permeability,  $k_r$ , depends on saturation which, in turn, depends on pressure. Relative permeabilities depend on saturation and are evaluated at each Gauss point during numerical integration. Viscosity,  $\mu$ , is constant throughout space and time.

The second term on the right of Equation (2.4.11) is further developed as follows:

$$\int_V \left( \frac{\hat{\mathbf{k}}^L k_r \rho}{\mu} \right) \nabla p_i \cdot \nabla \phi_i dV - \int_V \left( \frac{\hat{\mathbf{k}}^L k_r \rho}{\mu} \right) \rho \mathbf{g} \cdot \nabla \phi_i dV \quad (2.4.17)$$

Substituting for  $\int \nabla p dV$  in Equation (2.4.16) gives,

$$\begin{aligned} & \sum_{i=1}^{NN} p_i(t) \int_V \left( \frac{\hat{\mathbf{k}}^L k_r \rho}{\mu} \right) \nabla \phi_j \cdot \nabla \phi_i dV - \int_V \left( \frac{\hat{\mathbf{k}}^L k_r \rho}{\mu} \right) \rho \mathbf{g} \cdot \nabla \phi_i dV \dots \\ \dots & = \sum_{i=1}^{NN} p_i(t) \int_V \left( \left[ (\hat{\mathbf{k}}^L) \left( \frac{k_r \rho}{\mu} \right) \cdot \nabla \phi_j \right] \nabla \phi_i dV \dots \right. \end{aligned}$$

$$\dots - \int_{\forall} \left( \left[ (\hat{\mathbf{k}}^L) \left( \frac{k_r \rho}{\mu} \right) \cdot (\rho \mathbf{g}) \right] \right) \cdot \nabla \phi_i d\forall \quad (2.4.18)$$

The element volume is expressed as,

$$d\forall = dy dz dx = B(x, z) dz dx \quad (2.4.19)$$

where  $B(x, z)$  is the thickness of the mesh within the  $y$ -coordinate direction. The thickness is assumed equal to one throughout space and time. Substitution for  $d\forall$ , in Equation (2.4.18), gives

$$\begin{aligned} & \sum_{i=1}^{NN} p_j(t) \int_{\forall} \left( \left[ (\hat{\mathbf{k}}^L) \left( \frac{k_r \rho}{\mu} \right) \cdot \nabla \phi_j \right] \nabla \phi_i B(x, z) dz dx \dots \right. \\ & \left. \dots - \int_{\forall} \left( \left[ (\hat{\mathbf{k}}^L) \left( \frac{k_r \rho}{\mu} \right) \cdot (\rho \mathbf{g}) \right] \right) \cdot \nabla \phi_i B(x, z) dz dx \right) \quad (2.4.20) \end{aligned}$$

where  $(\frac{k_r \rho}{\mu})$  is a term based on nodewise discretized values of pressure,  $p$ .

The last two terms of Equation (2.4.6) are approximated cellwise. Both the fluid mass source term,  $\hat{Q}_p$ , and conductance,  $\nu_p$ , are averaged over the volume of a cell  $i$ .

$$\hat{Q}_p = \sum_{i=1}^{NN} \left( \frac{Q_i}{\forall_i} \right) \quad (2.4.21)$$

$$\nu_p = \sum_{i=1}^{NN} \left( \frac{\nu_i}{\forall_i} \right) \quad (2.4.22)$$

A single cell representation, with substitutions made for  $\hat{Q}_p$  and  $\nu_p$ , gives the last two terms of Equation (2.4.7) as,

$$\begin{aligned} & - \int_{\forall} \left( \frac{Q_i}{\forall_i} \right) \phi_i(x, z) d\forall - \int_{\forall} \left[ \left( \frac{\nu_i}{\forall_i} \right) (\hat{p}_{BC_i} - p_i) \right] \phi_i(x, z) d\forall \dots \\ & \dots = - \left( \frac{Q_i}{\forall_i} \right) \int_{\forall} \phi_i(x, z) d\forall - \left[ \left( \frac{\nu_i}{\forall_i} \right) (\hat{p}_{BC_i} - p_i) \right] \int_{\forall} \phi_i(x, z) d\forall \dots \end{aligned}$$

$$\begin{aligned} \dots &= -\left(\frac{Q_i}{\forall_i}\right) \forall_i - \left[\left(\frac{\nu_i}{\forall_i}\right)(\hat{p}_{BC_i} - p_i)\right] \forall_i \quad \dots \\ \dots &= Q_i - \nu_i(\hat{p}_{BC_i} - p_i) \end{aligned} \quad (2.4.23)$$

By combining and rearranging the evaluations of approximate terms of Equation (2.4.7), the following weighted residual relation is obtained:

$$AF_i \frac{dp_i}{dt} - BF_i + \sum_{j=1}^{NN} p_j(t) CF_{ij} - DF_i - Q_i - [\nu_i(\hat{p}_{BC_i} - p_i)] = 0$$

$$i = \overline{1, NN} \quad (2.4.24)$$

or

$$AF_i \frac{dp}{dt} i + \sum_{j=1}^{NN} p_j(t) CF_{ij} + \nu_i p_i = Q_i + \nu_i p_{BC_i} + BF_i + DF_i$$

$$i = \overline{1, NN} \quad (2.4.25)$$

where:

$$\begin{aligned} AF_i &= \left( S_w \rho S_{op} + \epsilon \rho \frac{\partial S_w}{\partial p} \right)_i \forall_i \\ BF_i &= \int_{\Gamma} \left[ \left( \frac{\mathbf{k} k_r \rho}{\mu} \right) \cdot (\nabla p - \rho \mathbf{g}) \right] \cdot \mathbf{n} \phi_i d_{\Gamma} \\ CF_{ij} &= \int_x \int_z \left( \left[ \left( \hat{\mathbf{k}}^L \right) \left( \frac{k_r \rho}{\mu} \right) \right] \cdot \nabla \phi_j \right) \cdot \nabla \phi_i Bdzdx \\ DF_i &= \int_x \int_z \left( \left[ \left( \hat{\mathbf{k}}^L \right) \left( \frac{k_r \rho}{\mu} \right) \right] \cdot [\rho \mathbf{g}] \right) \cdot \nabla \phi_j Bdzdx \end{aligned}$$

The integrals requiring Gaussian integration are  $BF_i$ ,  $CF_{ij}$ , and  $DF_i$ . The other terms, except for those involving  $\nu_i$ , are evaluated cellwise.

### Temporal Discretization

The time derivatives in the spatially discretized and integrated equation are approximated by finite differences. The pressure term is approximated as,

$$\frac{dp_i}{dt} \cong \frac{p_i^{n+1} - p_i^n}{\Delta t_{n+1}} \quad (2.4.26)$$

where

$$p_i^n = p_i(t^n)$$

$$p_i^{n+1} = p_i(t^n + \Delta t_{n+1}) = p_i(t^{n+1})$$

$$\Delta t_{n+1} = t^{n+1} - t^n$$

The current time step,  $\Delta t_{n+1}$ , begins at time  $t^n$  and ends at time  $t^{n+1}$ . The previous time step for which a solution has already been obtained at time  $t^n$  is denoted  $\Delta t_n$ . Temporal definitions are given in Figure B.7, where  $p^0$  is the initial pressure distribution at  $t^0 = 0$  seconds.

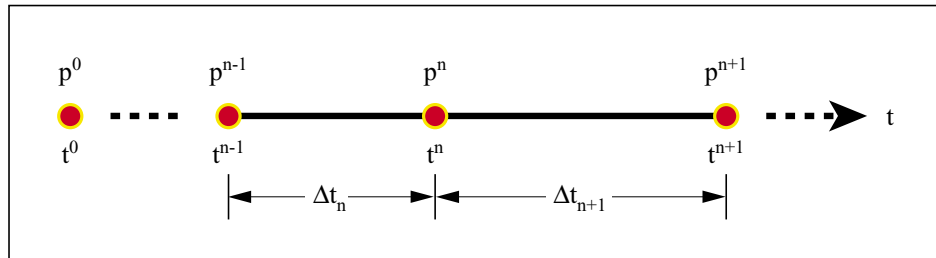


**Figure B.7:** Temporal definitions.

All other terms in Equation (2.4.25) are evaluated at the new time  $t^{n+1}$  for the solution of the present time step,  $\Delta t^{n+1}$ . For each time step, coefficients are

based on a projected value of fluid pressure,  $p$ . The projected pressure,  $p_i^{\text{proj}}$ , is an estimation of  $p$  at the end of the present time step,  $\Delta t_{n+1}$ , based on the linear extrapolation of the two previous values of  $p$ . The projected pressure is determined with a linear extrapolation between  $(t^{n-1}, p^{n-1})$  and  $(t^n, p^n)$ .

$$\begin{aligned} p_i - p_i^n &= \left( \frac{p_i^n - p_i^{n-1}}{t^{n-1} - t^n} \right) [t - t^n] = \left( \frac{p_i^n - p_i^{n-1}}{\Delta t_n} \right) [t - t^n] \\ p_i &= \left( \frac{p_i^n - p_i^{n-1}}{\Delta t_n} \right) [t - t^n] + p_i^n \end{aligned} \quad (2.4.27)$$

At  $t^{n+1}$  the projected pressure,  $p_i^{\text{proj}}$ , is given as

$$\begin{aligned} p_i^{\text{proj}} &= \left( \frac{p_i^n - p_i^{n-1}}{\Delta t_n} \right) [t^{n+1} - t^n] + p_i^n = \left( \frac{p_i^n - p_i^{n-1}}{\Delta t_n} \right) \Delta t_{n+1} + p_i^n \dots \\ \dots &= p_i^n + \left( \frac{\Delta t_{n+1}}{\Delta t_n} \right) (p_i^n - p_i^{n-1}) \end{aligned} \quad (2.4.28)$$

The weighted residual relation, Equation (2.4.25), is then written in a form which allows for the solution of pressures at nodes,  $p_i^{n+1}$ , at the end of the present time step,

$$\begin{aligned} \text{AF}_i^{n+1} \left( \frac{p_i^{n+1} - p_i^n}{\Delta t_{n+1}} \right) + \sum_{j=1}^{\text{NN}} p_j^{n+1}(t) \text{CF}_{ij}^{n+1} + \nu_i p_i^{n+1} \dots \\ \dots = Q_i^{n+1} + \nu_i p_{BC_i}^{n+1} + \text{BF}_i^{n+1} + \text{DF}_i^{(n+1)*} \quad i = \overline{1, \text{NN}} \end{aligned} \quad (2.4.29)$$

or

$$\begin{aligned} \left( \frac{\text{AF}_i^{n+1}}{\Delta t_{n+1}} \right) p_i^{n+1} + \sum_{j=1}^{\text{NN}} p_j^{n+1}(t) \text{CF}_{ij}^{n+1} + \nu_i p_i^{n+1} \dots \\ \dots = Q_i^{n+1} + \nu_i p_{BC_i}^{n+1} + \text{BF}_i^{n+1} + \text{DF}_i^{(n+1)*} + \left( \frac{\text{AF}_i^{n+1}}{\Delta t_{n+1}} \right) p_i^n \quad i = \overline{1, \text{NN}} \end{aligned} \quad (2.4.30)$$

where the superscript involving  $(n)$  or  $(n + 1)$  indicates the time of evaluation.

## **APPENDIX C: Scenario 1 Sensitivity**

Pressure RMSE = Root Mean Squared Error =  $\text{SQRT}\{\text{SUM}[(p_{\text{base}} - p)^2]/NN\}$

COMP TIME = Computational time required to complete a given simulation.

RATE OF CHANGE = Mass budget, rate of change in total stored fluid due to pressure change [kg/m].

Net Inflow (+) / Net outflow (-)

TOTAL OF FLOWS = Mass budget, total of fluid flows at points of specified pressure [kg/m].

Net Inflow (+) / Net outflow (-)

Base = Base case value.

### **INTRINSIC PERMEABILITY**

	PERM	PRESSURE RMSE	SATURATION RMSE	ANGLE RMSE	MAGNITUDE RMSE	COMP TIME (min)	RATE OF CHANGE	TOTAL OF FLOWS
Base	1.E-13	17842	0.509	63.7	7.74E-05	25.7	-0.001	-0.001
	1.E-12	16783	0.489	62.5	6.73E-05	25.6	-0.010	-0.010
	5.E-12	10198	0.353	56.6	3.95E-05	25.8	-0.048	-0.049
	1.E-11	0	0.000	0.0	0.00E+00	26.1	-0.058	-0.062
	5.E-11	7057	0.352	46.9	7.86E-05	26.9	0.000	0.000
	1.E-10	7053	0.355	52.5	7.86E-05	27.0	0.000	0.000

### **POROSITY**

	POR	PRESSURE RMSE	SATURATION RMSE	ANGLE RMSE	MAGNITUDE RMSE	COMP TIME (min)	RATE OF CHANGE	TOTAL OF FLOWS
Base	0.01	4249	0.25	52.0	4.1E-04	26.18	-0.029	-0.029
	0.05	2224	0.18	47.0	6.0E-05	26.14	-0.077	-0.047
	0.10	0	0.00	0.0	0.00E+00	26.07	-0.058	-0.062
	0.15	2275	0.18	46.8	2.7E-05	26.02	-0.086	-0.076
	0.20	4266	0.24	50.4	3.8E-05	26.08	-0.106	-0.084
	0.25	5465	0.26	49.6	4.4E-05	26.15	-0.081	-0.087
	0.30	7627	0.31	54.2	4.8E-05	25.90	-0.091	-0.091

### **TEMPORAL STEP SIZE**

	DT	PRESSURE RMSE	SATURATION RMSE	ANGLE RMSE	MAGNITUDE RMSE	COMP TIME (min)	RATE OF CHANGE	TOTAL OF FLOWS
Base	2	3228	0.206	51.9	3.7E-05	129.8	-0.078	-0.079
	5	1318	0.126	48.1	2.0E-05	52.1	-0.031	-0.070
	10	0	0.000	0.0	0.00E+00	26.1	-0.058	-0.062
	20	854	0.110	41.7	1.5E-05	13.1	-0.085	-0.057
	40	1041	0.121	42.1	1.7E-05	6.7	-0.061	-0.054
	100	877	0.118	42.8	1.3E-05	2.7	-0.052	-0.057
	200	879	0.107	38.6	8.5E-06	1.4	-0.101	-0.059
	500	2086	0.147	47.5	1.9E-04	0.6	-0.093	-0.065

### **PARTIALLY SATURATED PARAMETERS**

	Soil Type	PRESSURE RMSE	SATURATION RMSE	ANGLE RMSE	MAGNITUDE RMSE	COMP TIME (min)	RATE OF CHANGE	TOTAL OF FLOWS
Base	Sandy loam	3547	0.272	58.0	4.2E-05	26.47	-0.033	-0.036
	Silt loam	586	0.077	39.4	1.3E-05	26.18	-0.052	-0.067
	Loam	483	0.070	38.8	9.2E-06	26.25	-0.250	-0.066
	Sandy clay loam	0	0.000	0.0	0.00E+00	26.07	-0.058	-0.062
	Silty clay loam	2199	0.175	47.9	2.9E-05	26.23	-0.072	-0.074
	Clay loam	3048	0.218	50.9	3.9E-05	26.17	-0.046	-0.039
	Beit Netofa Clay	3847	0.233	46.9	4.2E-05	25.96	-0.080	-0.081

	a [1/m]	n	S <sub>sat</sub>	S <sub>wres</sub>	
Sandy loam	2.77	2.89	0.44	0.00	(Shao and Horton, 1998)
Silt loam	10.92	1.18	0.50	0.00	(Shao and Horton, 1998)
Loam	17.81	1.16	0.50	0.00	(Shao and Horton, 1998)
Sandy clay loam	0.58	1.59	0.54	0.09	(Shao and Horton, 1998)
Silty clay loam	1.36	1.24	0.56	0.00	(Shao and Horton, 1998)
Clay loam	1.25	2.38	0.56	0.07	(Shao and Horton, 1998)
Beit Netofa Clay	0.152	1.17	0.446	0.00	(van Genuchten, 1980)

**Total Number of Elements**

	<b>Num. of Elements</b>	<b>PRESSURE RMSE</b>	<b>SATURATION RMSE</b>	<b>COMP TIME (min)</b>	<b>RATE OF CHANGE</b>	<b>TOTAL OF FLOWS</b>
Base	7157	1475	0.043	186.7	-0.066	-0.066
	4186	966	0.010	63.6	-0.099	-0.063
	2696	0	0.000	33.7	-0.079	-0.065
	1877	1127	0.040	34.3	-0.061	-0.064
	1404	1552	0.012	9.1	-0.058	-0.063

Note: The RMSE analysis was conducted with the following nodal positions (X, Z).

<b>Position X</b>	<b>Position Z</b>
2.5126	96.6291
11.102	98.8522
16.6289	101.839
25.4377	101.728
34.0224	105.791
46.9804	111.61
51.6938	115.052
57.176	112.97
64.0599	113.45
68.2611	116978
79.0315	112.309

## **APPENDIX D: Sample SUTRA.d55 Input File**

```

SUTRA SOLUTE TRANSPORT
SUTRA Model created using ArgusONE
E-Road System Scenario 3
 4183 3949   93    0   242    0   234    0    6   308
    1     0     0   -1 1317
      0.          0.01       1.
 99999     200.      5270400.    9999     1.
 1317     1     0     0     0     1     1
    1     0.          0.
 2.718e-06     1.      1.e-09    1000.     0.
 1.27e-06     0.          0.      1025.
NONE     0.          0.
      0.          0.          0.
      0.        -9.81
NODE      1         1         1         1
  1     0   87.333 127.28566   1.     0.1
  2     0   87.054163 127.19016   1.     0.1
  3     0   87.333 126.80432   1.     0.1
  4     0   86.936639 126.86404   1.     0.1
  5     0   87.333 127.52633   1.     0.1
  6     0   87.109383 127.43238   1.     0.1
  7     0   86.843822 127.25948   1.     0.1
  8     0   86.954185 127.62555   1.     0.1
  9     0   86.58868 127.02331   1.     0.1
 10     0   87.06702 126.54291   1.     0.1
*****
 * **** * **** * **** * **** *
 * **** * **** * **** * **** *
 * **** * **** * **** * **** *
4175     0   0.867   96.633   1.     0.1
4176     0   1.1565557 95.164978   1.     0.1
4177     0   0.867   95.333   1.     0.1
4178     0   1.2168073 95.020472   1.     0.1
4179     0   1.2566953 94.853684   1.     0.1
4180     0   1.110322 94.902296   1.     0.1
4181     0   0.867   95.033   1.     0.1
4182     0   0.867   94.883   1.     0.1
4183     0   0.867   94.733   1.     0.1
ELEMENT     1         1         1         1         1         1         1
  1     0   1.e-11 1.e-11   0.     0.5     0.5     0.1     0.1
  2     0   1.e-11 1.e-11   0.     0.5     0.5     0.1     0.1
  3     0   6.e-13 6.e-13   0.     0.5     0.5     0.1     0.1
  4     0   1.e-11 1.e-11   0.     0.5     0.5     0.1     0.1
  5     0   7.e-14 7.e-14   0.     0.5     0.5     0.1     0.1
  6     0   7.e-14 7.e-14   0.     0.5     0.5     0.1     0.1
  7     0   7.e-14 7.e-14   0.     0.5     0.5     0.1     0.1
  8     0   7.e-14 7.e-14   0.     0.5     0.5     0.1     0.1
  9     0   7.e-14 7.e-14   0.     0.5     0.5     0.1     0.1
 10     0   7.e-14 7.e-14   0.     0.5     0.5     0.1     0.1
*****
 * **** * **** * **** * **** *
 * **** * **** * **** * **** *
 * **** * **** * **** * **** *
3940     0   6.e-13 6.e-13   0.     0.5     0.5     0.1     0.1
3941     0   6.e-13 6.e-13   0.     0.5     0.5     0.1     0.1
3942     0   6.e-13 6.e-13   0.     0.5     0.5     0.1     0.1
3943     0   6.e-13 6.e-13   0.     0.5     0.5     0.1     0.1
3944     0   6.e-13 6.e-13   0.     0.5     0.5     0.1     0.1
3945     0   6.e-13 6.e-13   0.     0.5     0.5     0.1     0.1
3946     0   1.e-11 1.e-11   0.     0.5     0.5     0.1     0.1
3947     0   7.e-14 7.e-14   0.     0.5     0.5     0.1     0.1
3948     0   3.e-13 3.e-13   0.     0.5     0.5     0.1     0.1
3949     0   3.e-13 3.e-13   0.     0.5     0.5     0.1     0.1
      -8     0.          0.
      -15    0.          0.
      -16    0.          0.
      -18    0.          0.

```

